MARYAM MORAVEJ

DÉVELOPPEMENT ET VALIDATION DES MATÉRIAUX MÉTALLIQUES POUR STENTS CARDIOVASCULAIRES BIODÉGRADABLES PAR DÉPÔT ÉLECTROLYTIQUE

Thèse présentée
à la Faculté des études supérieures de l'Université Laval
dans le cadre du programme de doctorat en génie de la métallurgie
pour l'obtention du grade de Philosophiae doctor (Ph.D.)

DÉPARTEMENT DE GÉNIE DES MINES, MÉTALLURGIE ET MATÉRIAUX
FACULTÉ DES SCIENCES ET DE GÉNIE
UNIVERSITÉ LAVAL
QUÉBEC

2011

Résumé

Les stents coronariens métalliques dégradables émergent comme une alternative possible aux stents permanents fabriqués à partir de métaux résistants à la corrosion comme l'acier inoxydable 316L. Le fer pur est un candidat intéressant pour les stents dégradables en termes de propriétés mécaniques, de dégradation et de biocompatibilité. Ce projet est le premier à étudier la faisabilité d'utiliser l'électroformage pour produire le fer comme matériau structural dans les stents dégradables. Dans ce projet, un processus de dépôt électrolytique a d'abord été développé. Les couches de fer produites ont une microstructure fine, une limite élastique élevée ainsi qu'une résistance à la traction ayant des valeurs comparables à celles de l'acier inoxydable 316L. Un traitement thermique de recuit à 550 ˚C pendant 1 h a produit une recristallisation dans le fer et a amélioré sa ductilité de 8 à 18 %. Des tests de corrosion par polarisation potentiodynamique et par immersion statique et dynamique ont permis l'étude de la dégradation du fer électroformé en solution de Hank. Il a été montré que le fer électrodéposé se corrode plus rapidement que le fer Armco ® déjà implanté comme stents biodégradables. L'effet de la densité de courant en tant que paramètre de l'électroformage sur la microstructure et la dégradation de fer a aussi été étudié. L'étude de diffraction d′électrons rétrodiffusés (EBSD) a montré que différentes microstructures, y compris la taille des grains et la texture, peuvent être produites à différentes densités de courant de 1 à 10 A dm^{-2}. Le plus haut taux de dégradation a été obtenu pour le fer fabriqué à 5 A dm^{-2}, car celui-ci possède la plus petite taille de grains et ceux-ci sont équiaxes avec des orientations aléatoires qui présentent un plus grand volume de joints de grains entraînant un taux de dégradation plus rapide. Enfin, le procédé d'électroformage a été appliqué avec succès pour la fabrication de mini-tubes de fer. Les mini-tubes de fer ont été électroformés sur les échantillons cylindriques d'étain qui ont été décollés par fusion du substrat après le processus. Les mini-tubes ont ensuite été utilisés pour la fabrication de stents de fer par découpe au laser. Les stents de fer ont montré une taille moyenne des grains de 5 µm après recuit et décapage à l'acide. Cette taille du grain est plus fine que celle généralement obtenue pour des stents SS 316L et pourrait fournir des propriétés mécaniques élevées et une dégradation ciblée pour les stents de fer électroformés.

Abstract

Degradable metallic coronary stents have emerged as possible alternatives for permanent stents fabricated from corrosion-resistant metals such as 316L stainless steel (316L SS). Pure iron has shown to be an interesting candidate for degradable stents in terms of mechanical properties, degradation and biocompatibility. This project is the first to investigate the feasibility of using electroforming process for production of iron for degradable stents where the material is used for a load-bearing application. In this project, firstly, an electroforming process was developed. The produced iron foils showed a fine microstructure and high yield and tensile strength were also obtained comparable to those of 316L SS. Annealing at 550˚C for 1h induced recrystallization in iron and improved its ductility from 8 to 18%. The investigation of the degradation of electroformed iron in Hank's solution using potentiodynamic polarization, static immersion and dynamic degradation tests showed that it corrodes faster than Armco® iron previously investigated for degradable stents. The effect of current density as an electroforming parameter on the microstructure and thereby the degradation of iron was also studied. Electron backscatter diffraction (EBSD) showed that different microstructures including grain size and texture were produced at different current densities from 1-10 A dm^{-2}. The highest degradation rate was obtained for iron fabricated at 5 A dm^{-2} since it possesses small grain size and equiaxed grains with random orientations providing more grain boundary volume can be held responsible for its faster degradation rate compared to the other iron samples. Finally, the electroforming process was successfully applied for the fabrication of iron tubes. Iron tubes were electroformed on Sn cylinders which were separated from them by melting after the process. The tubes were then used for the fabrication of iron stents by laser-cutting. Iron stents fabricated from electroformed tubes demonstrated an average grain size of 5 μm after annealing and acid-pickling. This grain size is finer than what usually obtained for 316L SS stents and could potentially provide high mechanical properties and targeted degradation for electroformed iron stents.

Preface

During the last decade, degradable metallic stents have been developed and investigated as alternatives for the currently-used permanent cardiovascular stents. Degradable metallic materials could potentially replace corrosion-resistant metals currently used for stent application as it has been shown that the effect of stent is temporary and the permanent presence of stents after the arterial remodeling could not provide any beneficial role. Although corrosion is generally considered as a failure in metallurgy, the corrodibility of certain metals can be an advantage for their application as degradable implants. These materials do their job to provide the required scaffolding effect of stent and degrade thereafter. The candidate materials for such application should have mechanical properties ideally close to 316L stainless steel which is the gold standard material for stent application in order to provide mechanical support to the diseased arteries. Non-toxicity of the metal itself and its degradation products is another requirement as the material is absorbed by blood and cells. Based on the mentioned requirements, iron and magnesium alloys have been the investigated candidates for degradable stents.

This doctoral project is included in a general program for design, development and evaluation of new candidate materials for degradable stents. The primary studies on degradable metallic stents included the implantation of the candidate metals in animals and the evaluation of their biocompatibility and degradation. However, our approach is to study the effect of metallurgical conditions of the candidate metals on their mechanical properties and degradation behavior based on the requirements for stent applications before proceeding to *in vivo* implantation. This approach could provide us with the insight on the effect of processing method, microstructure and composition of the investigated metals on their mechanical properties and degradation mechanism in order to tailor the desired properties. In this context, we also propose for the first time, the application of electroforming for the production of degradable iron-based stents. Electrodeposition is an electrolysis technique mainly used for production of coatings on metals to improve their performance. It is an ideal process for fabrication of small thin-walled metallic objects with different shapes, sizes and properties since it produces the metallic film layer by layer.

Therefore, this project focuses on the development and evaluation of iron-based metallic materials by electroforming for degradable stents.

This doctoral project was carried out under the direction of Professor Diego Mantovani and co-direction of Professor Michel Fiset. It consisted of 1) design and development of the electroforming technique, 2) fabrication of flat iron samples by electroforming, 3) adjustment of the electroforming parameters to produce metallic foils with low surface roughness and porosity, 4) the evaluation of microstructure and mechanical properties of the foils, 5) the study of the effect of electroforming current density on microstructure and degradation of the foils and finally 6) the fabrication of iron stents from electroformed iron tube and their microstructural evaluation.

This thesis has been prepared as an article insertion thesis and includes three journal articles in which I have acted as the principle researcher and the first author. The first article entitled: Electroformed iron as new biomaterial for degradable stents: Development process and structure–properties relationship, co-authored by Dr. Frederic Prima, Prof. Michel Fiset and Prof. Diego Mantovani, was published in the journal: Acta Biomaterialia, 2010, Vol. 6, Issue 5, P. 1726-1735. My contribution to this article was firstly the design of the experimental set-up and then performing of the experiments including: electroforming, mechanical-tensile testing, sample metallographic preparations for microstructural studies and corrosion testing. EBSD studies were carried out by Dr. Frédéric Prima. I subsequently prepared the first draft of the article which was revised by the other co-authors before submission.

The second article entitled: Electroformed pure iron as a new biomaterial for degradable stents: In vitro degradation and preliminary cell viability studies, co-authored by Agung Purnama, Prof. Michel Fiset, Prof. Jaques Couet and Prof. Diego Mantovani, was published in the journal: Acta Biomaterialia, 2010, Vol. 6, Issue 5, P. 1843-1851. My contribution to this article was firstly the design of the experimental set-up and then performing of the experiments including: material production by electroforming, sample preparation for microstructural studies, degradation testing and cell viability assays, degradation testing including static and dynamic tests and the study of the degradation mechanism and products after the tests. The cell viability assays were performed by my colleague, Agung

Purnama, PhD candidate, at Laval Hospital Research Center. I subsequently prepared the first draft of the article which was revised by the other co-authors before submission

The third article entitled: Effect of electrodeposition current density on the microstructure and the degradation of electroformed iron for degradable stents, co-authored by Dr. Sofiene Amira, Dr. Frederic Prima, Dr. Ahmed Rahem, Prof. Michel Fiset and Prof. Diego Mantovani, was submitted to the journal: Materials Science and Engineering: B on September 2, 2010. My contribution to this article was firstly the design of the experimental set-up and then performing of the experiments including: material production by electroforming at different current densities, heat treatment of the fabricated foils, degradation and corrosion testing, and sample preparation for microstructural studies. EBSD sample preparations and studies were carried out by Dr. Sofiene Amira at Aluminum Technology Centre; National Research Council Canada in Chicoutimi under the supervision of Dr. Ahmed Rahem. I subsequently prepared the first draft of the article which was revised by the other co-authors before submission.

I wish to express my deepest appreciation to my thesis advisor, Prof. Diego Mantovani, for giving me this opportunity to be part of his team and to work on this exciting project. I also appreciate his insight, guidance and continuous encouragement throughout this research.

I would also extend my gratitude to my co-advisor Prof. Michel Fiset for his insight and knowledge and his valuable comments and discussions through my Ph.D. studies. I am also thankful to my thesis evaluation committee, Dr. Matthias Peuster, Dr. Frédéric Prima, Dr. Dominique Dubé and Dr. Gaétan Laroche.

I am grateful to Daniel Macrotte, Michel Savard, Vicky Dodier and Marie-Josée Bouchard, the technicians of the Department of Mining, Metallurgy and Materials Engineering at Université Laval for their kind collaboration in technical support of the project. I am also really thankful to Maude Larouche for her help, training and collaboration in Metallography Lab and for Optical Microscopy studies, to André Ferland for Scanning Electron Microscopy studies and to Jean Frenette for X-ray diffraction analysis.

Specials thank goes to Prof. Edward Ghali for kindly allowing me to perform the corrosion tests in his laboratory and thanks to his group members for sharing the facilities.

Many thanks to all my colleagues in the Laboratory for Biomaterial and Bioengineering in Saint-Francois d'Assise hospital for their invaluable support and help particularity to Dr. Hendra Hermawan, Dr. Stéphane Turgeon, Dr. Pascale Chevalier, Dr. Jean Lagueux, Dr. Paula Horny, Dr. Sevaas Holvoet, Dr. Penelope Hale, Frédéric Couet and Agung Purnama.

I am thankful to Dr. Frédéric Prima from Laboratory for Physical Metallurgy, École Nationale Supérieure de Chimie de Paris for sharing his valuable insight and knowledge about Electron Backscatter Diffraction studies and for performing some of the experiments in his Laboratory. I also appreciate his valuable new ideas and discussions about the project.

Many thanks to Dr. Sofiene Amira from Aluminum Technology Centre, Industrial Materials Institute, National Research Council Canada for his interest, dedication and kind collaboration in sample preparation and EBSD analysis. Without his valuable help, EBSD studies would be far from completion. I am also grateful to Dr. Ahmed Rahem for his kind collaboration and thanks to Helene Gregoire and Genevieve Simard, the technicians of Aluminum Technology Centre for their help in sample preparation of EBSD studies.

I would like to thank Dr. Émile Knystautas from Physics Department of Université Laval who helped me perform thermal and electron-beam evaporation experiments in his lab and for his interest and the time he dedicated to this part of the project.

A special thanks goes to my dear friend, Pegah Seddighian, whose help and encouragement motivated me to start this journey and her care and support prevented me from feeling homesick and lonely during my first days in Canada.

Lastly, I would like to thank my family for their love and encouragement. I am grateful to my parents for their support, patience, and sacrifice in all and every stage of my life. They have always encouraged me to advance my education. And most of all, many thanks to my loving, supportive, encouraging, and talented husband, Hamed, whose scientific collaboration and technical help had a great influence in the progress of my Ph.D. Many thanks to my dear brother, Amir, and my friends for their encouragement and supports.

Table of Contents

List of Tables

List of Figures

Chapter 1. Introduction

A biomaterial can be defined as any material used to make devices or to replace a part of a function of the body in a safe, reliable, economic, and physiologically accepted manner [1]. In order to achieve that purpose, a biomaterial must be in contact with living tissue and/or body fluids resulting in an interface between living and nonliving substances. Biomaterials used for implants can be metals, ceramics, polymers and composites. The early use of metals as biomaterials has been reported since late 18th century when Fe, Au, Ag and Pt were used as wires and pins to fix bone fractures [2]. Metals have high impact strength, high wear resistance, high ductility and the capacity to absorb high strain energy (toughness) compared to other materials. These properties make metals suitable candidates for orthopaedic load-bearing application and fixation devices such as joint replacement, bone plates and screws, as well as dental implants, pacer and suture wires, and cardiovascular stents [1,2]. The implantation of cardiovascular stents is among the available treatment options for coronary artery disease the primary cause of which is *atherosclerosis* or occlusion of coronary artery by deposition of plaque along the artery wall [3]. The blockage of the arteries reduces or cuts off the oxygenated blood supply of the heart muscle leading to a heart attack. Stent are metal mesh structures that expand in the artery and hold it open after *percutaneous transluminal coronary angioplasty*. *Stenting* is indeed performed to improve the success of balloon angioplasty. In the process of stenting, a stent is mounted on the balloon and is expanded and positioned by inflating the balloon. The expansion of stent pushes it up against the artery wall and when the balloon is deflated the stent remains in place and hold the artery open. The other treatment options for coronary artery disease include medical treatment (in non-severe cases), minimally invasive surgical treatments such as *atherectomy* and invasive surgical method which is coronary artery by-pass graft surgery. By doing a stent insertion along with balloon angioplasty, the risk of the artery re-narrowing (*restenosis*) is reduced, and the risk of abrupt vessel closures during or within 24 hours of the procedure is nearly eliminated [4]. Although the ideal stent does not exist, the following properties are necessary to make the stent implantation more efficient [1]:

- Ease of visualization with X-rays
- High strength to resist arterial recoil
- Longitudinal flexibility to pass tortuous vessels
- Radial elasticity under external compression
- Fatigue resistance
- Minimal induction of *hyperplasia* of *intima*
- Thromboresistance
- *Biocompatibility*

Based on the mentioned requirements, metals including 316L stainless steel, Ni-Ti alloy and Co-Cr alloys have been the most suitable candidate materials for fabrication of stents [1,2].

1.1 Objectives of the project

This doctoral project was included in a large research program focusing on the development of candidate metals for degradable stents which show uniform degradation mechanism, are non-toxic and possess the necessary mechanical properties for their application as stent materials. Pure iron was selected as the candidate material for this study. Although Armco® iron had been previously studied by Peuster et al [5,6] for degradable stents, their investigations mostly focused on the implantation of iron stents in animal models. Therefore, the evaluation of microstructure, mechanical properties and degradation mechanism of iron from the materials science point of view was necessary. The objective of this project was to investigate the effect of microstructure on mechanical properties and degradation of iron and to explore the microstructural modifications which could increase its degradation rate. The method we decided to pursue in this project for production of iron was electroforming. Electrodeposition method have been previously used to apply coatings on the surface of metallic stents to alter their surface morphology, release drugs, enhance radio-opacity, and prevent corrosion [7]. However, it had never been explored for fabrication of a structure for load-bearing applications such as degradable

stents. Currently, the majority of stent materials are fabricated by casting and thermomechanical process. However, it has some limitations especially in production of pure metals which is of high importance in case of stent materials. In casting process, the nature and purity of the elemental material components mixed prior to melting, together with melt practice itself, have an influence on homogeneity, porosity and microcleanliness of stent materials. Standard casting processes for metallic implants such as ASTM F138 permit inclusions as thick as 15 μm on a 75 μm length. Such defects are massive compared with stent *struts* that can be thinner than 100 μm and could represent a serious problem of rupture upon expansion, thus, in selection of material source and in the melting process attention should be paid to purity and chemical composition [8]. Powder metallurgy is another metal fabrication method which was investigated by Hermawan et al. [9,10] to develop Fe-Mn alloys for degradable stent. In this process the size, morphology and purity of metal powders, mixing time and conditions, pressing load and sintering conditions including sintering temperature, time and atmosphere can strongly influence the products properties. The risk of this method is porosity which can be included in the final products and is very sensitive to the mentioned processing parameters.

Using electroforming to fabricate stent materials appears to be logical because this method which produces a metallic part by building up the structure of the material layer by layer could be an excellent method for manufacturing thin-walled products. In conventional metal working processes the metal is normally cast as a massive billet or ingot, which needs to be progressively reduced in size to yield a thin-section final product. This involves multiple working processes and can, therefore, be very costly as well as inefficient in terms of energy consumption. However, the production of thin layers and mesh products is by far the biggest industrial use of electroforming. A variety of metals can be electroformed, offering a wide selection of metallic properties for the product of this process. More common metals which are fabricated by electroforming are iron, nickel and copper. In recent years some of their alloys such as Fe-Co, Ni-Co and gold alloys are also produced by this process [11].

Different stent strut thicknesses have been reported in literatures from 75 to 200 μm [12]. The electroforming process has the potential of producing layers with different thicknesses

ranging from 10 μm to 5 mm, therefore, our primary objective was to produce iron foils, about 100-200 μm in thickness, by a developed electroforming apparatus and to study the effect of deposition parameters on microstructure, mechanical properties and *in vitro* degradation behaviour of the fabricated foils. This could permit us to obtain a better understanding of the feasibility of using electrochemically produced iron as a degradable stent material and also to develop a new class of electroformed degradable stents.

The next step of the project was the fabrication of iron stent tubes by electroforming. One of the advantages of electroforming is its specific capability to produce thin walled cylinders, without a joint line [13]. This property cannot be obtained by other fabrication methods including casting and powder metallurgy. With those methods, the primary ingot should be rolled to achieve the desired thickness. Tube drilling or drawing will be then necessary to obtain the stent tube. By electroforming, a stent tube could be directly electrodeposited on the surface of a cylindrical substrate in a one step process.

1.2 Strategies of the project

Figure 1.1 illustrates the flowchart of the project activities. The research and experimental work of this project was conducted in five stages. Firstly, the literature review on the current status of degradable stents and electroforming process was done while a series of preliminary experiments were carried out on the microstructural analysis and degradation of Armco® iron using three different degradation tests: potentiodynamic polarization, static immersion and dynamic degradation. These experiments were performed in order to know better the degradation properties of Armco® iron previously implanted as degradable stent.

The second stage of the project was to design and prepare a set-up for electroforming of iron based on the literature review. Iron foils were electroformed using the developed set-up and the electrodeposition parameters were optimized. The specimens were fabricated in the form of flat foils since this form was more practical for characterizations. Annealing was also performed on electroformed iron foils to investigate its effect on microstructure and mechanical properties. The study of the microstructure and mechanical properties of the electroformed iron before and after annealing was subsequently performed to investigate if the material had the potential to be applied for degradable stents. A rapid

corrosion testing using potentiodynamic polarization technique was also performed to evaluate the corrosion rate of electroformed iron compared to other materials previously studied for degradable stents. The result of this stage of the project including the electroforming of iron, microstructure and mechanical studies, and corrosion testing are included in the first article.

Although electroformed iron showed interesting mechanical properties and corrosion rate in the previous stage of the project, a more profound study on its degradation mechanism and its biocompatibility was necessary for its application as degradable stent. Therefore, the third stage of the project included detailed *in vitro* degradation evaluation of electroformed iron using static immersion and dynamic degradation test which simulated the conditions of an implanted stent in the artery in a more realistic way. Also, a series of cell viability assays using primary rat smooth muscle cells were performed on electroformed iron to assess the basic cells response in contact with this material. The results from this part of the project were published in the second article.

As the applications of electron backscatter diffraction in the second stage of the project revealed the presence of a strong texture in the electroformed iron deposited at certain parameters, the fourth part the project was performed to understand how the electroforming process can affect the microstructure and texture of electroformed iron and thereby influence its degradation. This was especially important since different textures and microstructures could potentially change the degradation rate and form of the stent material. This stage of the project included the production of iron foils deposited at different current densities, annealing of the electroformed foils, microstructural and texture investigation of electroformed iron foils before and after annealing and finally degradation testing of iron foils deposited at different current densities in as-electroformed and annealed states. The results of this stage were reported in the third article.

Because the objective of the project was to produce electroformed iron for degradable stents, the final stage was to investigate the feasibility of fabricating stents from electroformed iron tubes. During this stage, the electroforming set-up was modified for production of cylindrical specimens instead of flat foils. After investigating a number of materials as substrate, a cylindrical tin substrate was used to produce iron tubes. The

substrate was separated from the tubes by melting after the electroforming. The iron tubes were subsequently ground and laser cut to obtain iron stents. Suitable annealing and acid pickling techniques were developed during this stage to induce recrystallization and to remove the undesired parts of the stents, respectively. Finally the microstructural investigation was performed on the fabricated stents.

1.3 Structure of thesis

This thesis is presented in eight chapters. The first chapter is a general introduction of the thesis and presents the problem identification and the objectives and strategies of the project.

In the second chapter, a literature review of the current status of degradable stents is presented. It starts with a brief review on cardiovascular disease and its treatment method with stents. A detailed review on material selection, properties and fabrication of degradable stents is then presented.

The third chapter focuses on the electroforming of iron. The first part is allocated to an introduction on electrodeposition and electroforming and in the second part a literature review on the electroforming of iron including the deposition process, parameters and the properties and characterization methods of electroformed iron is presented.

Chapters 4-7 are considered as the result sections of the thesis. They present the experimental approach as well as the results of this thesis.

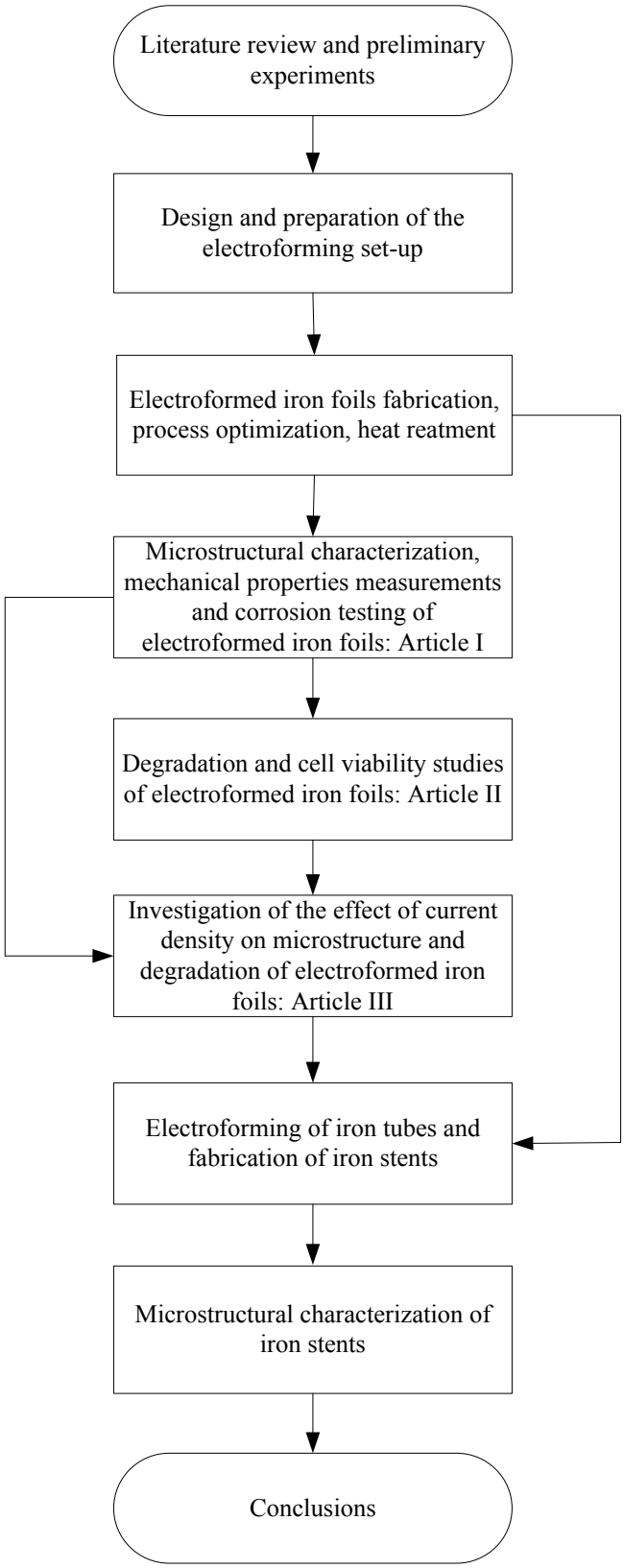

Figure 1.1- Flowchart diagram of the experimental strategy of the project

Chapter 4 reports firstly the experimental methods for iron electroforming process development, selection of deposition parameters, composition, phase and microstructural characterization of the fabricated iron films, evaluation of the mechanical properties and finally corrosion testing of iron foils. The second part of the chapter presents the obtained results and discussion. The results showed that the electroforming process was successful for production of iron foils with a thickness of 80-100 μm. A strong (1 1 1) texture was observed for electroformed iron with the average grain size of 4 μm which is significantly smaller than the grain size observed for iron produced by casting and thermomechanical treatment. Electroformed iron showed high yield and tensile strength comparable to those of 316L stainless steel which is considered as the gold standard for stent materials. However, the ductility of iron was only 8% and an additional annealing at 550˚C for 1 h was required to improve the ductility. Annealing was found to produce recrystallization in electroformed iron and changed its strong texture to a more randomly oriented microstructure. The corrosion rate of electroformed iron was higher than that of Armco® iron previously investigated as a degradable stent material. This chapter was published as an article in the journal: Acta Biomaterialia on May 2010.

The experimental methods and results of the investigation of the degradation mechanism and preliminary biocompatibility of electroformed iron are presented in Chapter 5. Two *in vitro* degradation tests including static immersion and dynamic degradation were performed on electroformed iron before and after annealing and the results were compared to those of Armco® iron. The degradation rate was calculated and a degradation mechanism was proposed based on the analysis of the degradation layer formed on the surface of the specimens. The form of degradation was identified using microscopic images. Electroformed iron showed uniform degradation with higher rate than that of Armco® iron. The degradation rate decreased after annealing because of the recrystallization and the slight grain growth observed after heat treatment. Cell viability and cell counting essays were performed on electroformed iron to assess its biocompatibility using rat smooth muscle cells (SMC). The results showed that iron had no effect on cell metabolic activity of SMCs compared to the control and 316L stainless steel but reduced the cell number slightly which can be considered as an advantage for application of the material as stent. This chapter was also published in the journal: Acta Biomaterialia, May 2010.

Chapter 6 focuses on the effect of current density on microstructure and degradation of electroformed iron. Because current density is one of the main parameters affecting the microstructure and properties of electrodeposited metal, current density was varied in the range of 1-10 $A.dm^{-2}$ and its effect on electroformed iron was studied. The microstructure of iron foils was characterized using electron backscattered diffraction to identify the orientation of grains as well as the average grain size. Potentiodynamic polarization and static immersion test were subsequently performed on electroformed iron specimens deposited at different current densities to assess their degradation behaviour. A discussion on the effect of microstructure on degradation of different iron samples is finally presented. This work was submitted as an article to the journal: Materials Science and Engineering: B on September 2010.

In Chapter 7, the fabrication process of iron stents from electroformed iron tubes and the microstructural evaluation of the resulting stents are presented. As the objective of the project was to investigate the feasibility of applying electroforming process for fabrication of stents, the last part of the project was iron tube electroforming. Iron tubes were electroformed on Sn cylinders and the substrates were removed by melting after the process. Tube grinding, laser cutting, annealing and acid pickling were then performed to achieve iron stents. The results showed that the fabrication of stents from electroformed iron tubes was feasible with some modifications to annealing and acid pickling process. Iron stents had an average grain size of 5µm which is smaller than those generally observed in 316L stainless steel stents. This fine grain size is anticipated to provide high strength and ductility to iron stents. However, the mechanical properties of iron stents should be investigated before reaching to any conclusion.

In Chapter 8, concluding remarks of the project are presented and some perspectives to continue this work are suggested.

Chapter 2. Degradable Stents- State of the art

2.1 Cardiovascular disease (CVD)

2.1.1 Facts and statistics about cardiovascular disease

CVD has been the number one killer and the major cause of illness and disability in Canada. It is the most costly disease, putting the greatest burden on Canada's national health care system. In year 2005, over one third (33%) of all deaths in Canada were due to heart disease and stroke and according to World Health Organization statistics, it affected both sexes and all age groups [14]. Figure 2.1 shows the classification of different cause of deaths in Canada in 2005.

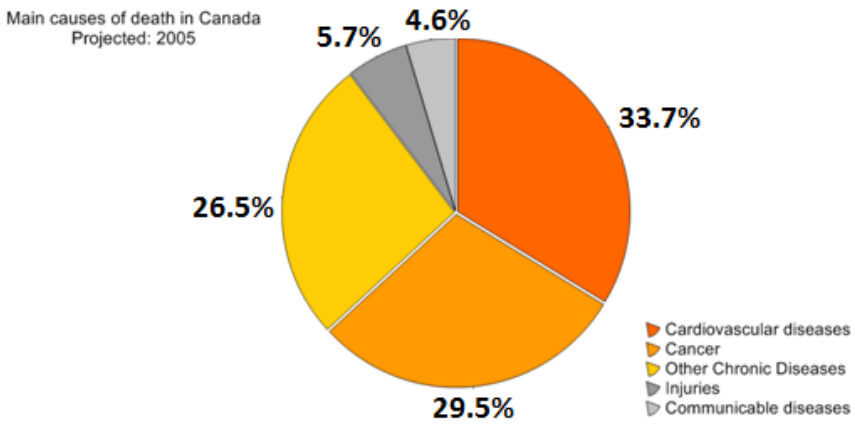

Figure 2.1- Percentage of different causes of deaths in Canada in 2005, adapted from Ref.[14]

2.1.2 Coronary artery disease (CAD)

Cardiovascular diseases are diseases affecting the heart and circulatory system. The most widespread form of cardiovascular disease starts with damage and occlusion of the coronary arteries and reduction of coronary blood supply to the heart. The most frequent cause of obstruction in a main coronary artery is *atherosclerosis* [3]. Atherosclerosis leads to the formation of plaques of *atheroma* that can build up within the arterial walls. The

plaque is made up of LDL-Cholesterol, lipids and cellular debris and narrows the diameter of the large and medium-sized arteries. This narrowing of the arteries can lead to a loss of tissue elasticity and loss of oxygen to the arterial tissues, heart muscles and brain tissues and as the damage increases there is increased reduction of blood flow to vital organs, such as the heart or brain, even kidneys and lower extremities. Plaques are also prone to rupture or to ulcerate and then act as a site for blood clot formation (Figure 2.2).

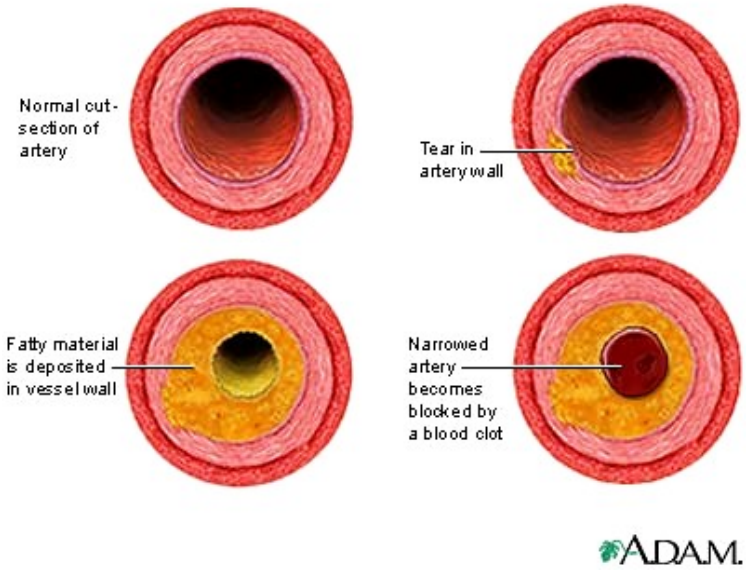

Figure 2.2- Developmental process of atherosclerosis, adapted from Ref. [15]

The resulting blood clots (*thrombosis*), which can block the affected vessel completely, are usually responsible for the more severe clinical manifestations of cardiovascular disease such as *ischemia* which is the reduction of demanded oxygen of the heart leading to a heart attack and stroke [16].

2.2 Treatment of CAD by stenting

Stent is a small mesh-like tubular scaffold which is placed and then is expanded inside the coronary artery to keep the *lumen* open. Stenting is a catheter-based procedure in which a stent is inserted into the artery to hold it open following a balloon angioplasty. At present, stenting is performed during about 60 percent of balloon angioplasty cases. In this process, the stent is mounted on the balloon and is expanded and positioned by inflating the balloon.

The expansion of stent pushes it up against the artery wall and when the balloon is deflated the stent remains in place and hold the artery open. In addition to balloon expandable stents, self expanding stents are produced with the desirable diameter and are loaded on a smaller catheter. Once the stent is deployed on the diseased location in the artery, the catheter is withdrawn and the stent expands into the artery [4]. Stenting can considerably reduce the risk of restenosis after the angioplasty, however, in about 25% of cases of stenting, the problem of restenosis can still remain which is called *in-stent restenosis* (ISR). ISR is caused within 3-6 months after stenting by *neointimal proliferation* which is an excessive healing process after the tissue injury [17]. In recent years, different methods are being investigated for the treatment of ISR most of which are focused on its prevention [18]. Figure 2.3 shows the stenting process following balloon angioplasty.

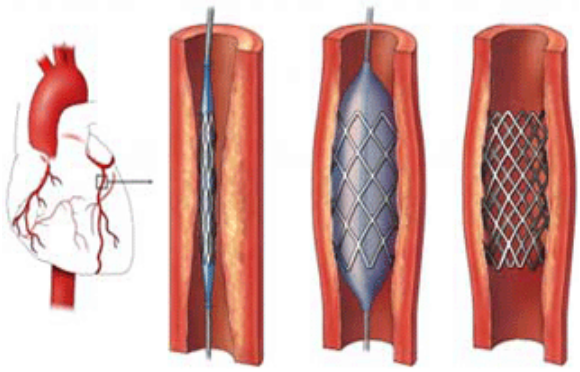

Figure 2.3- Stenting procedure: the stent is inserted into the artery using a catheter; it is expanded and positioned by inflating the balloon; the stent remains in place and hold the artery open. adapted from Ref. [19]

2.3 Stent development history

The idea of using stents was firstly introduced by Dotter in 1969 in order to improve the application of balloon angioplasty in the treatment of vascular occlusion by keeping the lumen open and by reducing the risk of restenosis associated to this process. In 1983, he could successfully deploy stainless steel and Nitinol coil stents in animal trial studies. The first human use of stent occurred in 1986 by Sigwart et al [4], but it was not sooner than 1994

when the Cordis Palmz-Schats stent was approved by FDA of the US. Since then stents have been increasingly used as new alternatives in treatment of coronary artery disease. In the first decade after the approval of Palmaz-Schatz stent, several generations of bare metal stents were developed, with each succeeding one being more flexible and easier to deliver to the narrowing site. However, while stents virtually eliminated many of the complications of abrupt artery closure, restenosis persisted. Although the rates were somewhat lower, bare metal stents still experienced reblocking (typically at six-months) which necessitates a repeat procedure [18].

The idea of drug-eluting stent was put forward as a solution for in-stent restenosis to move stent from purely mechanical devices toward pharmacologic advances. Physicians and companies began testing a variety of drugs that were known to interrupt the biological processes that caused restenosis [20]. Stents were coated with these drugs, sometimes imbedded in a thin polymer for time-release, and clinical trials were begun. The first drug eluting stent (DES), which was a Cypher *Sirolimus*-Eluting Coronary Stent made by Cordis Corporation, was approved by FDA in April 2003. The stent was made of stainless steel and coated with Sirolimus as an anti-restenosis drug which inhibits the vascular smooth muscle cell proliferation [21]. Since then, some other drug eluting stents have been developed in US and Europe and proved to be successful in reducing the restenosis rate. Although it is proven that DES can reduce the problem of restenosis, it has become obvious that permanent stents generate problems other than just IRS. Also it has been shown that the requirement for stent implantation is temporary and is limited to a short period after stenting during which the arterial remodelling and healing is done. In this context, the development of degradable stents which fulfill the short-term need for a stent and prevent the potential long-term complications of permanent stents can be a logical approach [22]. The first degradable stent was developed in 1980's from a polymeric material (poly-L lactic acid) and there have been several experimental and clinical studies on implantation of polymeric stents [23]. Recently metallic degradable stents have been developed and in 2001, the first degradable metallic stent made from pure iron was implanted in rabbits by Peuster et al [5]. In December 2004, the first human implantation of a degradable metal stent (Biotronik magnesium stent) was performed [22]. Since then, the development of degradable metallic stents has been increasing rapidly and more human clinical implantation studies of

magnesium stents have been reported. Degradable stents have also the potential to be coated with drugs and to serve as platforms for local drug delivery [24]

2.4 Degradable stents

Bare metal stent implantation mainly fabricated from 316L stainless steel, Nitinol and cobalt-chromium alloy has shown tremendous superior effects in various kinds of clinical situations, especially in the field of percutaneous coronary intervention, compared to simple balloon angioplasty. From the studies using intracoronary ultrasound after balloon coronary angioplasty, the two underlying components were identified as the mechanisms for restenosis after balloon coronary angioplasty: tissue accumulation and arterial remodelling. Pathologic remodelling, which occurs late between 3 and 6 months after balloon angioplasty, can contribute as the dominant mechanism of restenosis. Stent implantation can reduce the subsequent restenosis by utilizing its scaffolding effect and preventing the lumen shrinkage as a result of pathologic remodelling. However, it cannot prevent the tissue accumulation within stents, and this is the shortcoming of bare metal stent implantation leading to ISR which occurs in 25% of stent deployments [25].

Also, permanent metallic implants have specific drawbacks which limit their more widespread use. These limitations include long-term endothelial dysfunction, delayed re-endothelialization, *thrombogenicity*, permanent physical irritation, chronic inflammatory local reactions, mismatches in mechanical behavior between stented and non-stented vessel areas, inability to adapt to growth, and importantly non-permissive or disadvantageous characteristics for later surgical *revascularization* [22].

Since the major effect of stent implantation is provided by its scaffolding effect, its radial force and endurance have been considered very important. From the ultrasound observations on coronary restenosis, the scaffolding effect of stent is required to last for 6 months. After this period, the presence of stent within the body cannot provide any beneficial effects. Thus, the development of degradable stents, which can fulfill the mission and step away, is the logical approach [23,25]. The material for degradable stents is requested to have at least the following characteristics: it must be biocompatible; degradation products of the material must also be biocompatible, the material must stay in the place for

several months before its complete bioabsorption and the radial force of the resultant stent must be enough for scaffolding effect during the requested period [25]

2.4.1 Polymeric degradable stents

The first degradable stent was developed by Stack and Clark of Duke University in the early 1980s. They investigated a number of degradable polymers and selected Poly-L Lactic Acid (PLLA) as the stent material. This material has a high tensile strength, permitting robust mechanical design, but requiring long degradation times [26]. Currently, most of degradable polymeric stents are fabricated of PLLA and numerous experimental and clinical investigations have been performed about the performance and efficiency of this material as a degradable stent. Tamai et al [27] reported their preliminary results of PLLA degradable stent implantation in human coronary arteries. They performed coronary *angiography* and intravascular ultrasound during 6 months after the stenting procedure. The results showed that all stents were delivered successfully. There were no deaths, *myocardial infarctions*, coronary artery bypass graft, or stent thrombosis. However, Eberhart et al observed inflammatory response to sterilized PLLA stents implanted in the porcine femoral artery and suggested that this tissue responses might be due to the parent polymer compound, additives to the polymer, intermediate biodegradation products, the implant geometry, or combinations thereof [26].

Degradable polymeric stents can be used as platforms for local drug delivery in the diseased coronary arteries. Tsuji et al [28] used the Igaki-Tamai PLLA stent for a new DES system acting as a vehicle for local Tranilast administration which is an atni-allergic drug inhibiting the migration and proliferation of vascular smooth muscle cells. The Tranilast-eluting Igaki–Tamai stents were supposed to reduce neointimal hyperplasia and restenosis after stent implantation; however, there are not yet sufficient experimental or clinical data on these stents to present.

Although a variety of polymer-based degradable stents are currently being commercially developed, there are important drawbacks of polymer stents relate to their intrinsic mechanical properties. Polymers are not able to guarantee the same radial force and limited recoil compared with metal platforms, and their relative bulkiness could limit application in small vessels [22]. Also, there are some complications associated with the implantation of

PLLA polymeric stents such as required heating process during balloon inflation and uncontrolled expansion of stent [5]. Furthermore, severe tissue responses were identified with some biodegradable polymers in porcine models. Therefore, more trials and development of materials and techniques are necessary to bring these stents to clinical study and confirm their efficiency and safety [29]. For polyglycolide (PGA) degradable implant material, it is confirmed that the rapid degradation process and its acidic products are responsible for causing inflammation in surrounding tissues [30].

2.4.2 Metallic degradable stents

2.4.2.1 Fe-based degradable stent

The first degradable metallic stent was fabricated from Armco® iron (Fe >99.8%) and implanted in descending aorta of 16 New Zealand white rabbits [5] . Iron can interconvert between ferric (Fe^{2+}) and ferrous (Fe^{3+}) forms by accepting and donating electrons quite readily, which makes it a useful component for cytochromes, oxygen–binding molecules (hemoglobin and myoglobin), and many *enzymes*. Iron ions are bound to transferrin (the Fe–transporting protein) during circulation and bound to ferritin (the Fe–storaging protein) when accumulated within cells. Even though iron is essential to life, its excess or deficiency can be deleterious [31]. However the results from the implantation of the first iron stent showed no significant evidence of either an inflammatory response or neointimal proliferation, and organ examination did not reveal any systemic toxicity. There was also a maintained stent *patency*, no thromboembolic complications, and no adverse events during a 6-18 month follow-up period [5]. In 2006, another study was performed to evaluate the safety of corrodible iron stent in a peripheral stent design (6-12 mm diameter) in a slotted tube design. Iron stents were implanted into the descending aorta of 29 minipigs which were followed for 1-360 days and 316L SS stents were implanted as reference. The results showed no difference with regard to the amount of neointimal proliferation between 316L SS and iron stents. Also no signs of iron overload or iron-related organ toxicity were observed. Adjacent to the iron stent struts, there was no evidence for local toxicity due to corrosion products. It was concluded that iron is a suitable metal for the production of a large-size degradable stent with no local or systemic toxicity. However, the implantation of Armco® iron stent showed that the stents did not corrode completely during the follow up

period and therefore, faster degradation rate is desirable for iron and further studies have to focus on the modification of the composition and design of the stent to expedite the degradation process [6]. In a more recent study, iron stents were deployed in the coronary arteries of juvenile domestic pigs. Cobalt chromium stents were also implanted for comparison. Short-term effects of the implanted stent were investigated after 28 days. Results showed that iron stents started to show signs of degradation without evidence of stent particle embolization or thrombosis without traces of excess inflammation, or *fibrin* deposition. At 28 days, the surface of the iron stent struts was black to brown and the vascular wall adjacent to the iron stent had a brownish tinge. There were no statistically significant differences in any of the measured parameters between segments implanted with iron and cobalt chromium stents. There were also no adverse effects in the persistent areas [32]. Because the study was limited to a short period after implantation, no conclusion could be drawn about the degradation rate of iron stent. However, the results of long-term implantation of iron stent showed that future efforts have to focus on the acceleration of the degradation rate. The suggested mechanisms are either using iron-based alloys with a more pronounced corrosion rate or increasing the surface of the stent along with reduction of the strut thickness and modification of the stent design[5,6].

2.4.2.2 Mg-based degradable stent

Magnesium is another attractive material for biodegradable implants because of its low thrombogenicity and well-known biocompatibility. It is an essential trace element and has a high systemic toxic level which is about 7 to 10 millimols per litre of serum [33]. The use of magnesium as a biodegradable stent material was also based on the fact that it is a structural constituent of the tissue and essential element in the living organism. Magnesium is a substantial intercellular cation which is involved in more than 300 biological reactions of cell. Magnesium is also regarded as a *non-carcinogenic* element. However, magnesium has a rapid degradation in aggressive chloride environments like body fluid. Rapid degradation of magnesium implant results in tissue overload with degradation products and this can lead to neointimal formation. Accelerated degradation of magnesium can also cause the loss of mechanical integrity in a short period which can limit its application as an implant material. Therefore, magnesium is alloyed with other elements such as aluminum,

manganese and rare earth elements in order to decrease the degradation rate [34]. The first application of magnesium in cardiovascular applications dates back to year 1878 when Huse used a Mg wire ligature successfully to stop bleeding vessels three times: once in a radial artery and twice in the operation for varicocele. Later in the 20th century, magnesium was used in several investigations as biodegradable material for connectors for vessel anastomosis and wires for aneurysm treatment [35]. However, Heublein et al [36] were the first to investigate the idea of using magnesium alloys for cardiovascular stents. They selected AE21 alloy which has lower degradation rate compared to other magnesium alloys for an initial coronary animal study. It was expected to have up to 50% mass loss during the first half-year of the implantation. The experiments were performed by implantation of stents into the coronary artery of eleven domestic pigs and the follow up procedure was performed at 10, 35 and 56 days after implantation. The histological analysis showed that AE21 magnesium stent induced a neointimal response, but this disadvantage was offset by later positive remodelling. There was not also any *platelet* deposition or *thrombus* at the endothelial sites after any of assessment intervals. Furthermore, a negligible inflammatory response was observed on evaluating each strut. The problem of AE21 stent was that its degradation occurred faster than the expected rate as the loss of mechanical integrity occurred between 35 and 56 days after implantation. Therefore, further improvements are necessary with respect to prolongation of the degradation and mechanical stability over a defined time. In addition, the short and long term local biocompatibility and bioreactivity of such alloys and their components before and during degradation need to be assessed. These investigations and experiments later resulted in the invention of a new generation of biodegradable stents in Biotronic Company [37].

Di Mario et al [38] reported the results of experimental implantation of Lekton Magic coronary stent (Biotronik, Bulach, Switzerland) in the coronary artery of 33 mini-pigs and also the preliminary results of the first clinical study of bioabsorbabe WE43 magnesium alloy stent implantation in human for treatment of critical lower limb ischemia. The animal implantation results showed that it is significantly more efficient than stainless steel stent in increasing of the minimum luminal diameter. By now, the clinical implantation of the magnesium stent into the lower leg arteries of 20 patients showed that there were no symptoms of allergic or toxic reactions to the stent material.

The first successful implantation of a biodegradable metal stent in human was performed by Zartner et al [39] in the left *pulmonary* artery of a preterm baby with a congenital heart disease. The biodegradable stent selected for implantation was a magnesium stent 3 mm in diameter and 10 mm in length fabricated by Biotronik Company. The follow-up procedure showed the complete degradation occurred during 5 months and no in-stent obstruction or neointimal *hypertrophy* could be observed. This first result with a biodegradable magnesium stent implantation rescued a child from an extremely severe clinical problem and this case implicate that such stent technology may be more widely applicable in babies and children with different stent diameters and lengths.

In more recent studies, Waksman et al [40] investigated the safety and efficacy of bioabsorbable WE43 magnesium alloy stents in porcine coronary arteries for a period of 3 months. There was no evidence of stent particle embolization, thrombosis, excess inflammation, or fibrin deposition and neointimal area was significantly less in magnesium alloy stent segments as compared with the stainless steel stent segments. They concluded that magnesium alloy stents are safe and are associated with less neointima formation; however, reduced neointima did not result in larger lumen.

2.4.3 In vitro degradation of metallic materials for degradable stents

Besides the study of *in vivo* behaviour of degradable stents, the *in vitro* degradation is investigated to assess the degradation behaviour of the developed materials. Based on the data found the literature, three different methods are applied which are presented in the following section.

2.4.3.1 Static immersion

The most applied *in vivo* degradation testing method is static immersion generally performed based on ASTM G31-72 [41] test with some modifications. In this test, metallic samples are immersed in a physiologically simulated solution for a certain period. The temperature and pH of the solution are selected to be close to 37ºC and 7.4, respectively, which are similar to those in human body. The weight of samples is measured before and after the test and based of the weight loss; corrosion rate can be calculated. The analysis of the surface morphology and corrosion products after the test can also identify the

mechanism and form of corrosion. Peuster et al. [5] have applied static immersion test to iron for the evaluation of its corrosion rate before stent implantation. They immersed iron probes in Ringer electrolyte solution and incubated under continuous stirring and temperature of 37ºC for two weeks and in different time intervals, sampling from the solution was performed to measure the Fe^{2+} ion release from the specimens. Based on the calculated corrosion rate, the iron stent can keep its mechanical strength within the first 6 months of implantation while degrade slowly during this period. However, the *in vivo* results showed that the corrosion rate was even slower than what was calculated since the stents did not degrade completely after 18 months of implantation. It was concluded that future research has to focus on the kinetics of *in vivo* corrosion and its modification.

Static immersion test has been also applied to the degradable magnesium alloys for orthopaedic implants and cardiovascular stents in several investigations [42-48]. Specific simulated body fluid (SBF), Hank's and Ringer solution have been used as corrosion milieu in the mentioned references.

2.4.3.2 Electrochemical corrosion testing

Potentiodynamic polarization [10,43,44,47,48] and Electrochemical impedance spectroscopy (EIS) [44,47,49] are two electrochemical testing methods applied to assess the corrosion rate and behaviour of degradable metals. In both methods, a three-electrode set-up is used in which the specimen act as working electrode, a platinum sheet is used as counter-electrode, and a reference electrode is used as a half cell to build an electrochemical cell. Reported testing solutions for these methods have been prepared from Hank's solution[10,45], a borax-phosphate buffer[43], artificial seawater[50], and specific simulated body fluid [47,51]. Potentiodynamic polarization is performed based on two standard methods ASTM G9 [52] and ASTM F2129 [53]. In this technique, the potential of the electrode is varied at a selected rate by application of a current through the electrolyte. The potential is measured between the reference electrode and the working electrode and the current is measured between the working electrode and the counter electrode. This data is then plotted as current (I) vs. potential (E). Based on the obtained corrosion current, the corrosion rate can be calculated. EIS technique records impedance as a function of the frequency of an applied AC signal at a fixed potential. EIS data can be used to determine R_p which is the inverse of corrosion

rate [54]. Parameters such as corrosion rate, electrochemical mechanisms and reaction kinetics, and detection of localized corrosion, can all be determined from EIS data.

2.4.3.3 Dynamic degradation

Since most *in vitro* degradation studies of degradable metals was based on static immersion method, Levesque et al [46] came up with the idea of developing a new degradation testing method specially designed for degradable stent metals. They developed a dynamic test bench in which the testing solution circulates and produces a laminar flow on the surface of specimens simulating the conditions of a coronary artery. They used the test bench to evaluate the degradation of AM60B-F magnesium alloy in Hank's solution. They also performed the standard immersion testing to calculate the corrosion rate based on the weight loss of specimens. According to the results, for the specimens immersed in the static conditions the corrosion mechanism was inter-granular and filiform. However, because of the conditions of the dynamic test including a shear stress resulting from the circulation of the solution, the corrosion of specimens was more uniform. The results of both static and dynamic test showed that the degradation of AM60B-F is very rapid and it would not be a suitable material for degradable stents [45]. Dynamic degradation test has also been used to assess the degradation behaviour of pure iron and Fe-Mn alloy for degradable stents. Dynamic degradation rate for both iron and Fe-Mn alloy was higher than static degradation rate. Pure iron showed uniform degradation [45] while localized pitting corrosion was observed for Fe-Mn alloy [55].

2.4.4 Mechanical properties of degradable metals for stent

Currently, there is no standard for the required mechanical properties of degradable stents. Since 316L SS is the gold standard material for stent fabrication, its mechanical properties are considered the ideal properties for stent materials. 316L SS has well-suited mechanical properties including high yield and tensile strength and excellent ductility [56].

Table 2.1 presents the mechanical properties of degradable metals studies for stent application compared to those of 316L SS. According to the U.S. Food and Drug Administration (FDA), radial strength of the stent is defined as change in stent diameter as a function of circumferential pressure, noting the point at which the deformation is no

longer reversible [57]. Therefore, pure iron has superior radial strength because of its higher elastic modulus. This can be helpful in making stents with thinner struts. Iron has also high ductility which can be helpful during the implantation of stent when the stent is plastically deformed. The results from the implantation of iron stent showed that the stents maintained their mechanical properties during the implantation without any failure [5]. Magnesium alloys have limited ductility compared to most Fe alloys. The ductility of WE43 Mg alloy is only 4% [24] . The ductility of Mg alloys can be improved by alloying and employing advanced processing techniques. For example, newly-developed bio-absorbable magnesium alloys ZW21 and WZ21 showed fine and even microstructures with grains smaller than 10 μm, which generated exceptional plasticity of 17 and 20% at ambient temperature [58]. Generally, Mg and its alloys have low density and stiffness close to those of cortical bone (ρ = 1.99 g cm^{-3} and E = 11.7-18.2 GPa). Its low Young's modulus will be of benefit in reducing the stress shielding at the bone-implant interface, which makes Mg alloys very interesting candidates for biodegradable bone implants [24].

Table 2.1- Mechanical properties of different degradable metals compared to 316L SS

Material	Young's modulus (GPa)	Yield Strength (MPa)	Tensile Strength (MPa)	Elongation (%)
SS 316L (ASTM F138, annealed)[56]	190	250	580	55
Pure iron (annealed) [56]	211	150	200	40
Fe-35Mn alloy (annealed) [59]	-	234	428	32
WE43 Mg alloy (tempered) [56]	44	162	250	4

2.4.5 Forming methods for stent materials

2.4.5.1 Casting and thermomechanical treatments

Currently, most of surgical implant metallic materials including stents are fabricated by casting and thermo-mechanical treatment methods. Metallic parts can be cast either directly into the shape of the component or as ingots that can be subsequently shaped into a desired

form using other forming processes. From an economic standpoint, it would be desirable to form most metal components directly from casting, since subsequent operations such as forming, extruding, annealing and joining add additional expense. However, since the growth rate of crystalline phases is much higher in the liquid state than in the solid state, the microstructure of as-cast materials is much coarser than that of heat-treated or annealed metals. Casting is generally only used as the primary fabrication process and consequently, other forming and thermo-mechanical processes are performed to achieve the desired shape and mechanical properties [60]. Melting of most implant metals is performed under vacuum condition. The use of vacuum in melting operations is used not only to prevent reactions such as oxidation, but to prevent, and even remove, dissolved gases in the metals in order to avoid porosity [61].

In the case of stent materials, the selection of a melt source is extremely important. The nature and purity of the elemental material components mixed prior to melting, together with melt practice itself, have an influence on homogeneity, porosity and microcleanliness of the cast alloy [8]. For instance, in case of Nitinol implant material, to achieve a more precise control, an in-situ composition control process can be implemented during melting where samples are taken from the molten metal and the transformation temperatures are quickly analyzed for instant composition adjustments [62].

The mechanical working of implant metals can be accomplished by various processes, including forging, rolling, and extrusion which are usually performed at elevated temperatures. Such hot working processes break down the cast structure and improve mechanical properties by plastic deformation and work hardening mechanisms. Optimal hot working temperatures are selected in the range that the alloy is easily workable and the surface oxidation in air is not too severe. Following hot working, metals are cold worked and heat-treated to obtain final dimensions with desired physical and mechanical properties [61,62].

2.4.5.2 Powder metallurgy

Powder metallurgy in another fabrication technique involves the compaction of powdered metal, followed by a heat treatment to produce a denser piece. The challenge in powder metallurgy, especially in sintering is to obtain a high density product and keep the grain

size in the desired range. Higher sintering temperatures lead to higher densities but also result in grain growth. Therefore, the sintering parameters should be optimized. Also in this process the size, morphology and purity of metal powders, mixing time and conditions, pressing load and sintering atmosphere influence the properties of the products [63].

Powder metallurgy process has been used for the fabrication of Nitinol implant materials in the experimental basis. Resulting density varies from process to process and the highest density (95%) has been achieved by Hot Isostatic Pressing (HIP). Elemental powders of Ni and Ti can be sintered using either combustion or thermal explosion process. Otherwise, Nitinol materials sintered from elemental powders are highly porous and may contain other intermetallic phases of Ti_2Ni and $TiNi_3$. The limitation of Nitinol PM processes appears to be the oxygen content which has been reported to exceed 3000 ppm. Oxygen at this level may negatively impact ductility and fatigue resistance [62].

The development of Fe-35Mn alloy as a biodegradable stent material by powder metallurgy process has been reported by Hermawan et al [10]. The alloy was single austenitic (γ) phase with high yield strength (234 MPa) and ductility (31%). Porosity was observed in the microstructure of the alloy due to powder metallurgy processing. However, it was suggested that the porosity could be helpful to accelerate the degradation of the alloy which was twice higher than that of pure iron [59].

2.4.6 Stent tube fabrication

In the stent fabrication process, after the production of bulk material and application of required thermomechanical treatment, tube drawing is performed; because a majority of stents are cut from tubing. An adequate degree of control in the tube drawing process is required to ensure repeatable properties for the tubing. After the preparation of stent tubes, they can be laser cut to the final stent design. It is of utmost importance in the laser cutting to achieve a consistent strut width. If the constant laser beam energy hits variable walls, it will tend to cut a wider slot where the wall is thinner and may damage the opposite side of the tubing. Wall should be specified with tolerances that imply an adequately accurate wall measurement system [8].

Chapter 3. Electrochemical Deposition- Literature Review

3.1 Electrodeposition

Electrodeposition is the process of depositing a coating having desirable form by means of electrolysis. Its purpose is generally to alter the characteristics of a surface so as to provide improved appearance, ability to withstand corrosive agents, resistance to abrasion or other desired properties. Electrolysis is carried out in a solution (bath) which may consist of fused salts or of solutions of various kinds; in commercial practice it is almost invariably a water solution. The principle of electrodeposition is described in Figure 3.1 in which two electrodes (cathode and anode) are immersed in solution and connected to the output of a DC current source. The cathode, onto which the metal or alloy is deposited, may itself be a metal such as stainless steel or a non-metallic conductor such as graphite. The primary purpose of anode is to complete the electrical circuit, and as the metal ions are removed from the solution and converted to metal, one or more balancing processes must take place at the anode to remove the anions and thereby maintain the electrical neutrality. The anode may fulfill a second function (in the case of soluble anodes), which is to provide a source of fresh metal to replace the metal ions of the solution which are deposited in the cathode [64-67]. The amount of electrochemical reaction that occurs at an electrode is stated in Faraday's law according to the following Equation 3-1 [64]:

$$w = \frac{I t A}{n F}$$ **Equation 3-1**

Where W is the weight of a product of electrolysis (g), I is the applied current (A), t is the deposition time (s), A_{wt} is its atomic weight, n is the number of electron involved in reaction and F is the faraday constant (96.487 C mol^{-1}). The thickness of a deposit may also be evaluated from the Faraday's law if W in Equation 3-1 assumed to be ρ.V where ρ is the density and V is the volume of the deposit.

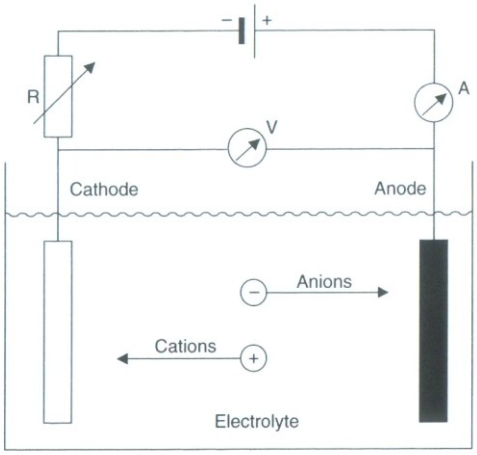

Figure 3.1- Electroplating process: the cations are reduced on the surface of cathode upon the application of an electrical current forming a metal layer. adapted from Ref. [66]

3.2 Electroforming

The process of electroforming is a type of electrodeposition which has emerged as a practical procedure for producing metallic parts with intricate shape and close dimensions. Whereas electrodeposits are used to enhance the surface properties of a substrate metal or nonconductor, electroforms are usually used as independent objects and are separated from the substrate mandrel after electrodeposition. While copper, iron and nickel are usually selected for electroforming, a number of alloys also have been investigated [11,13,68,69]. Figure 3.2 depicts the process of electroforming for production of a metallic part. Today, the electroforming industry sees a number of high-tech uses for nickel, iron, copper and alloy deposits to electrofabricate exceedingly important components such as the main combustion chamber for space shuttle, prosthetic devices, high precision optical scanners, holographical masters, and recording masters. Different microstructural features from few nanometres to tens of micrometers grain size can be achieved by electroforming providing metals with different properties and applications. Electroforming also provides unique production advantages for precision operation in textile, medical, aerospace, communication, electronics, photocopying, automotive and computer industries [68]. Electroforming can enable the user to manufacture complex shapes and surfaces at low unit cost. Seamless objects can be formed as well as complex shapes, which economically defy machining. The virtually perfect surface reproducibility available with electroforming

processes makes them ideal for dimensionally exacting applications which were mentioned above. Some other advantages of electroforming include the wide range on mechanical properties which can be achieved by selecting a suitable plating electrolyte and adjusting operating conditions. In some instances properties can be created in electroformed metals that are difficult to duplicate in wrought counterparts. Also the size and thickness of electroformed parts are not limited. Larger size can be accommodated by increasing the tank volume in which the electrolyte is contained. Thickness may vary from micrometers (as foils) to more centimetres, as is common in rocket thrust chamber shells [68,70].

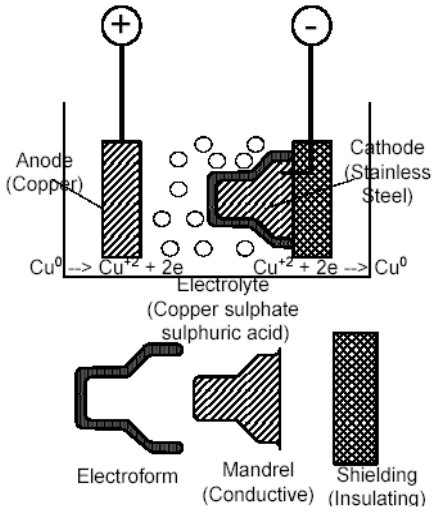

Figure 3.2- Principle of electroforming: the metallic layer formed on the surface of cathode is separated after electrodeposition and used as a separate part. adapted from Ref. [13]

3.3 Structure of electrodeposited metals

Electrodeposition produces a variety of microstructures by varying deposition conditions and electrolyte composition. The influencing parameters on microstructure are additives, current density, substrate microstructure and surface morphology, temperature and pH of electrolyte. These parameters control nucleation and growth of metallic deposits during electrocrystallization and thereby affect the microstructure [71]. For example, generally, higher current densities promote grain refinement as an increase in the current density results in a higher overpotential that increases the nucleation rate [72]. As for growth

mechanism of metallic deposits, two general theories are proposed: layer (two dimensional) growth and three-dimensional (3D) crystallites growth. A schematic illustration of these two mechanisms is presented in Figure 3.3. In layer growth mechanism a crystal enlarges by spreading of discrete layers (steps), one after another across the surface. In this case a step is a structure component of a coherent deposit. In general, there is a tendency for a large number of thin steps to bunch into a system of few thick steps. Monoatomic steps can unite to form a polyatomic step. In the 3D crystallites growth mechanism the structural components are 3D crystallites and a coherent deposit is built up as a results of coalescence of these crystallites. The 3D growth sequence of electrodeposition consists of four stages: (1) formation of isolated nuclei and their growth to 3D crystallites, (2) coalescence of 3D crystallites, (3) formation of linked network, and (4) formation of a continuous deposit. Development of columnar microstructure is very common in electrodeposited metals. A columnar structure perpendicular to the substrate surface is schematically shown in Figure 3.4. This microstructure is composed of relatively fine grains near the substrate but then changes to a columnar microstructure with much coarser grains at greater distances from the substrate. The development of such microstructure may be interpreted as a result of growth competition between adjacent grains. The rapid growth of low-surface-energy grains at the expense of high-surface-energy grains results in an increase in mean grains size with increase thickness of deposit and transition from fine grains to coarse columnar grains [64,67,73].

In electrodeposited metals, there is a crystal direction which grows faster toward the anode than the other ones. Grains possessing this direction can also grow and cover other less favorably oriented grains. In this way the deposit mostly consists of the grains of the favorable growth direction. If the grains are not randomly oriented, the condition is called texture [64]. The energy of formation of layers of various orientations is responsible for texture development. It has been found that the overpotential can determine which crystal plane had the minimum energy of formation and thus could be preferentially nucleated. For example, at low overpotentials, the energy to form a (1 1 1) plane of a face-centered cubic metal is the lowest. Therefore, (1 1 1) monolayers should develop preferentially. At higher overpotentials, other planes would be favored [74]. Texture has a marked influence on the

properties of a given deposit. Properties such as corrosion resistance, hardness, magnetic properties, porosity, contact resistance, and many others, are all texture dependent [67 75].

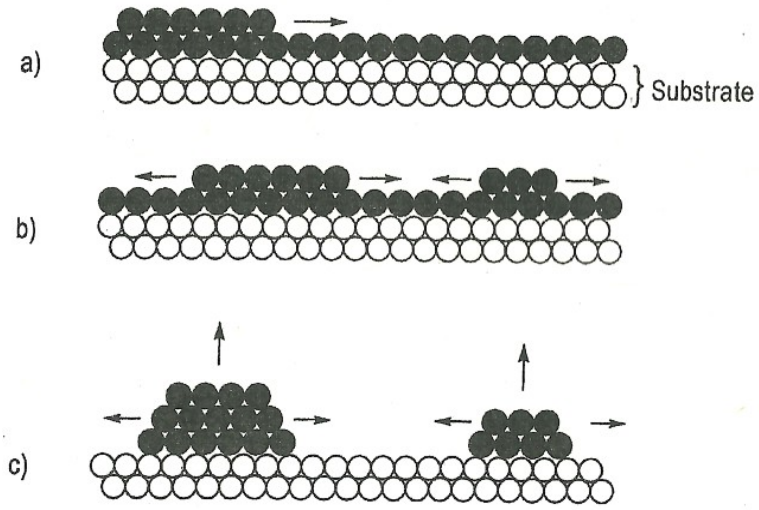

Figure 3.3- Schematic representation of layer growth (a,b) and 3D growth (c), adapted from Ref. [64]

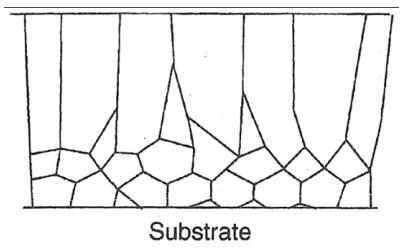

Figure 3.4- Schematic cross section of the columnar deposit, adapted from Ref. [64]

3.4 Mechanical properties of electrodeposited metals

The microstructure of electrodeposits is generally characterized to have a high density of defects including grain boundaries (due to small grain size) primary dislocations, twins, codeposited foreign atoms or molecular groups and point defects such as vacancies. The density of dislocations in electrodeposits can be as high as 10^{12} cm^{-2} which is comparable

that of plastically deformed metals [64,74,76,77]. Therefore, electrodeposits are generally stronger and harder but less ductile than the same metals formed by other means. The higher dislocation density and small grain size is two causes of the higher strength. Fine-grained copper deposits have been shown to obey the Hall-Petch equation which states that the yield strength is inversely proportional to the square root of the grain diameter [78]. Most deposits are inherently brittle because of these structural defects, internal stress, and codeposition of hydrogen which can results in hydrogen embrittlement [74,75]. Some deposits appear to be brittle but are really quite ductile. The reason is that the plastic deformation is confined to a small region in which fracture subsequently occurs. Such small regions have been observed to elongate over 100%. However, when this elongation is averaged over the whole gauge length of a tensile specimen, the value is very low and the deposit appears to be brittle. In this case, the true strength is much greater than the nominal one. For the same reason, deposits are stronger when attached to a substrate so that necking is prevented [78].

Table 3.1 presents tensile properties of electrodeposited metals compared to their wrought counterparts. It can be observed that e.g. for electrodeposited iron, the minimum tensile strength is 327 MPa which is superior to the average value of 282 MPa observed for iron prepared by casting and thermomechanical treatment.

As for hardness, electrodeposited metals are generally harder than those produced by other methods. Defects resulting from electrodeposits growth patterns are mainly responsible for the higher hardness. The higher dislocation density of electrodeposits, which is comparable to that of cold worked metals, is a major contributing factor to the higher hardness. The very small grain size resulting from inhibited growth also results in high hardness [74].

Annealing of electrodeposits at low temperatures is generally performed to remove internal stress and hydrogen which can be source of embrittlement [64]. Fine-grain electrodeposits recrystallize on annealing at relatively low temperatures. The recrystallization temperature of electrodeposits is generally lower than that of wrought metals [64,74]. Thin nickel deposits recrystallized at 260°C and copper electrodeposits recrystallized at temperatures lower than 300°C [74,77]. It was found that the recrystallization of small grains occurred as they rotated to align themselves with their neighbors. Larger-grain deposits recrystallized at higher temperatures by the movement of their boundaries [74].

Table 3.1- Tensile properties of electrodeposited metals compared to their wrought counterparts, adapted from Ref. [79]

		Tensile Strength (electrodeposited)			Tensile Strength (wrought) [a]	
Metal	**Plating Bath**	**Minimum MPa**	**Maximum MPa**	**Elongation %**	**Tensile Strength MPa**	**Elongation %**
Aluminum	Anhydrous chloride–hydride–ether	76	214	2-26	90	35
Cadmium	Cyanide	-	69	-	71	50
Chromium	Chromic acid	97	552	< 0.1	83	0
Cobalt	Sulfate–chloride	517	1186	< 1	255	-
Copper	Cyanide, fluoroborate, or sulfate	172	641	3-35	345	45
Gold	Cyanide and cyanide citrate	124	207	22-45	131	45
Iron	Chloride, sulfate, or sulfamate	327	1067	2-50	283	47
Lead	Fluoroborate	14	16	50-53	18-21	42-50
Nickel	Watts and other types of baths	345	1048	5-35	317	30
Silver	Cyanide	234	331	12-19	159-186	50-55
Zinc	Sulfate	48	110	1-51	90	32

[a] Annealed, worked metal.

3.5 Characterization of the structure of electrodeposited metals

The most frequently used instrument to reveal the microstructure of electrodeposits is scanning electron microscope (SEM). Compared to optical microscope, SEM has greater field of depth allowing rough topography of electrodeposits to be completely in focus[64]. Optical microscopy can provide information on the structure of metallographically prepared cross sections. However, such investigations provided essentially no information about the surface structure [78]. SEM also enables one to analyze the elemental composition of electrodeposits using energy dispersive X-ray spectroscopy (EDS). The main disadvantage of SEM is that it does not determine the crystal structure and the orientation of grains. When secondary electrons are used for imaging, nodules consisting of many crystallites can have the appearance of grains and can be easily mistaken by them. Therefore, it is difficult to identify the grain size using SEM [64].

Recently, electron backscattered diffraction (EBSD) has been developed to examine the crystallographic orientation and texture or preferred orientation of crystalline or polycrystalline material. This technique uses the backscattered electrons in SEM to identify the crystal systems, and is also applied to crystal orientation mapping, defect studies, phase identification, grain boundary and morphology studies, etc. Experimentally, EBSD is conducted using a SEM equipped with a backscatter diffraction camera. This technique has been vastly used during the last decade for determination of grain size and orientation in electrodeposited metals [80,81].

Transmission electron microscope (TEM) has better resolution than SEM and it is possible to obtain atomic resolution by this method. TEM has been used extensively to study the initial stages of deposition in thinner deposits. On a clean substrate, the first layers are generally deposited epitaxially. By transmission electron microscopy, it has also been demonstrated that the early stages of deposition usually consist of the formation of three-dimensional crystallites. The crystallites subsequently coalesce to form layers of the deposit [78]. TEM is applied in both the dark and bright-field modes to estimate grains size and distribution, twins, grains boundaries and dislocations in electrodeposits [82]. With the use of electron diffraction patterns in TEM the orientation as well as direction of grains can be

determined [83]. The main disadvantage of TEM is the extensive preparation required for most electrodeposits.

X-ray diffraction (XRD) has been used primarily to determine the phase composition, grain size and texture of electrodeposits. In nanocrystalline electrodeposited metals, there is a peak broadening effect in XRD pattern caused by small grain size. Therefore, XRD result can be used for grain size estimation based on Debby-Scherrer equation for grain sizes up to few hundreds of nanometres [84]. For texture analysis it is often assumed that the most intensely diffracting crystal plane is preferentially parallel to the surface [85]. In this case, the possibility must be considered that a plane with a zero structure factor, which do not diffract, can be the preferentially oriented one. Another application of XRD is the measurements of internal macrostresses in electrodeposits from the shift of a diffraction peak. However, the results are usually not very accurate because of the line broadening due to small grain sizes. Also, because of preferred orientation, the intensities of the peaks which shift the most are often low [64].

Atomic force microscopy (AFM) is often used for *in situ* observation of electrodeposits. Its most common application is the observation of surface topography and roughness measurements. AFM can be used well in air, vacuum or in an aqueous environment. The latter is of special importance in the study of electrodeposition nucleation and growth processes [66]. The application of AFM to study the effect of electrodeposition parameters in nucleation mechanism, surface topology and grain size of electrodeposits has been reported in numerous investigations [86-91].

3.6 Electrodeposition of iron

The first record of iron electrodeposition dates back to 1846 and the first commercial application of electrodeposited iron occurred in 1868 when iron was electroplated onto engraved copper plates used for printing bank notes. Numerous applications for electrodeposited iron have since been commercially exploited. Two main applications of electroformed iron components with a possible commercial future are reported: foil and moulds. Several foil and mould plants are known to have operated for lengthy periods in the U.S.A. and Germany. The electroformed iron foils have been used in production of magnetic and electronic parts. The moulds produced were used for making car tyres, rubber

artificial limbs and glass headlight lenses [64,68]. Although the electrodeposition of iron has been technically possible, the problem of sensitivity of electrodeposited products to corrosion has limited its industrial success [92]. Iron magnetic alloys are produced by electrodeposition for applications in *Micro-Electro-Mechanical Systems* (*MEMS*). Ni, Co and Pt are generally co-deposited with iron to produce magnetic films with much higher corrosion resistance than that of pure iron [93-98]. The electrodeposition of Zn-Fe alloys is also reported for protective and decorative coatings onto low-carbon steel. These alloys have interesting properties such as excellent corrosion resistance due to the nature of the zinc–iron phase, excellent paintability, good welding properties due to the high hardness and melting point of zinc–iron phase in comparison to the pure zinc [99].

3.6.1 Iron electrodeposition parameters

3.6.1.1 Bath

The bath is the electrolyte or solution containing the ions of the metal which is deposited on the cathode surface. Principally, iron is deposited from acidic solutions of iron (II) (ferrous) salts. The presence of iron (III) (ferric) is undesirable in the bath because it lowers the cathode efficiency for depositing the metal and it may cause the deposits to be brittle, stressed and pitted [64,70]. There are several baths which has been used for iron deposition and could be seen in Table 3.2. The properties of deposited iron depend on the bath type and composition and the bath is selected based on the application and desired properties of the metal to be deposited. For instance, the iron (II) sulphate bath produces deposits that are smooth and light grey in color. By using this bath, there is little tendency toward pitting and thick deposits can be produced. However, this bath yields brittle deposits, the deposition rate is slow and the current density in which burning occurs is about one half of that of a hot chloride bath. Ferrous chloride bath permits higher current densities or fast deposition rates and yields ductile deposits when operated at temperatures higher than about 85ºC. Currently, the most commonly used bath for iron electroforming is a solution of iron (II) chloride and calcium chloride which has been referred to as Fischer-Langbien solution. The composition of this bath has been modified for industrial use consisting of 400 g L^{-1} $FeCl_2$ and 80 g L^{-1} $CaCl_2$ as the main components [64].

3.6.1.2 Additives

Although a highly purified iron bath can yield good deposits, the addition of stress reducing and wetting agents (anti-pitting) can significantly enhance the quality of deposits. The most commonly used additive in electrodeposition is saccharin. It has long been used to reduce the internal stress of deposits and to refine the grain structure. Saccharin molecules are adsorbed in a reversible way on active sites of the electrode surface, thereby blocking active sites and reducing crystal growth. Moreover, surface diffusion of the adatoms is impeded by the adsorbed organic molecules. Therefore, saccharin is especially effective in reducing residual stress and improving film quality [97,100,101]. Sodium saccharin has shown to strongly effect the microstructure and magnetic properties of thin iron films deposited on Si (1 1 1) substrate from of a $Fe(NH_4)_2(SO_4)_2$ bath. The addition of sodium saccharin resulted in increase of the initial growth rate of iron by change in kinetic factors. It reduced the grain size and the roughness of iron films. The increase in saccharin amount improved the preferential (1 1 0) texture of Fe as well as its crystallinity. The addition of sodium saccharin was also accompanied by a significant reduction in the magnetic coercive field with respect to pure iron films [102].

Use of a wetting agent tends to decrease the production of pits in electrodeposited iron. The pits are caused by hydrogen bubbles produced by the reduction of hydrogen ions on substrate surface. Sodium lauryl sulphate has been reported by several authors to be an effective agent and seems to be compatible with all types of iron baths [64]. It is an anionic wetting agent which prevents bubbles of hydrogen from adhering to the cathode and causing pits [103]. The addition of other wetting agents such as sodium naphthalene sulfonate and formaldehyde to the iron (II) chloride bath is also reported to eliminate pitting [64].

Table 3.2- Composition and operating conditions for iron electrodeposition baths

Solutions	Composition	Operating Conditions
Sulphate [64,91,102,104,105]	$FeSO_4.(NH_4)_2SO_4.6H_20$:250-300 g L^{-1}	Low pH 2.8-3.4 or High pH 4.0-5.5, 2 Adm^{-2}, 25˚C
	$FeSO_4.7H_2O$: 250 g L^{-1} $(NH_4)_2SO_4$: 120 g L^{-1}	pH 2.1-3.4, 4-10 Adm^{-2}, 60˚C
(for production of strips)	$FeSO_4.7H_2O$: 600 g L^{-1}	pH 1.4, 6.7 Adm^{-2}, 47˚C
Chloride [64,91,92,106,107] (Fischer-Langbien)	$FeCl_2.4H_2O$: 300 g L^{-1} $CaCl_2$: 335 g L^{-1}	pH 0.8-1.5, 6.5 Adm^{-2}, 90˚C
	$FeCl_2.4H_2O$: 300-450 g L^{-1} $CaCl_2$: 80-190 g L^{-1}	pH 0.2-1.8, 2-9 Adm^{-2}, 88-99˚C
(for electrotype)	$FeCl_2.4H_2O$: 240 g L^{-1} KCl: 180 g L^{-1}	pH 5-5.5, 2-5 Adm^{-2}, 25-40˚C
(for production of strips)	$FeCl_2$: 120-150 g L^{-1}	pH 0.5-4.7, 33-40 Adm^{-2}, 98-106˚C
Sulphate-Chloride [64] (for electrotype)	$FeSO_4.7H_2O$: 250 g L^{-1} $FeCl_2.4H_2O$: 42 g L^{-1} NH_4Cl: 20 g L^{-1}	pH 3.5-5.5 5-10 Adm^{-2}, 40-43˚C
(for production of strips)	$FeSO_4.7H_2O$: 500 g L^{-1} NaCl: 50 g L^{-1}	pH 2.5, 3-27.5 Adm^{-2}, 80˚C
Sulfamate [64]	Fe (II) sulfamate: 250 g L^{-1} Ammonium sulfamate: 30 g L^{-1}	pH 3.2-, 15 Adm^{-2}, 50-70˚C
Fluborate [64]	$Fe(BF_4)_2$: 226 g L^{-1} NaCl: 10 g L^{-1}	pH 2-3, 2-10 Adm^{-2}, 55-60˚C
Alkaline solution [108]	Fe_2O_3 particles in aqueous NaOH solution	1-20 Adm^{-2}, 110˚C

3.6.1.3 pH

Generally, chloride baths are used in more acidic pH compared to sulphate baths. The pH of electrolytes is controlled by adding HCl, H_2SO_4 and sodium hydroxide (NaOH). For Chloride bath, the pH in the range of 0 to 3 is reported to have only a slight effect in mechanical properties of iron electrodeposits. Below pH 0 the foil is highly stressed and brittle while above pH 3 ferric ions, Fe (III), can exist in the solution causing a reduction in cathodic current efficiency and foil quality [92,107]. It has been shown that current efficiency increased with increasing pH value in the range of 0-2 of the chloride solution operated at 20˚C and 5 Adm^{-2}. This finding implied that the hydrogen evolution reaction had been decreased when the pH value of the solution was relatively higher. Vickers Hardness

decreased with an increase of the pH value of the solution. Solution pH has also showed to have an effect on crystallographic orientation and grain size of iron. The orientation index of the (2 0 0) planes as well as grain size of iron increased with increasing pH value of the solution in the range of 0-2 [106].

3.6.1.4 Temperature

Temperature of the bath has been also found to have an influence on electrodeposits grains size, texture and mechanical properties. An increase in temperature tends to produce deposits with larger grain size and reduced hardness, tensile strength and internal stress but with greater elongation [92,107]. Increasing temperature of the chloride solution from 20 to 60˚C increased the orientation index of plane (1 1 0) suggesting that (1 1 0) orientation is promoted at higher temperatures [106]. Myung et al. showed that stress in electrodeposited Fe films from chloride bath decreased dramatically with increase in operating temperature, independent of the applied current density [109].

3.6.1.5 Current density

The increase of current density is generally believed to increase the electrodeposition overpotential and thereby increases the rate of nucleation. Therefore, fine-grain deposits are produced at higher current densities. The commonly applied current density for iron electrodeposition from chloride bath is in the range of 2-100 Adm^{-2} [68]. In a constant deposition time, the weight and thickness of electroformed layer increase with current density according to Faraday's law (Equation 3-1).

Lai et al. [107] have reported that bright smooth electrodeposits of iron can be obtained for current densities in the range 10-100 Adm^{-2} and at solution temperatures from 86 to 108°C using chloride bath. However, Yoshimura et al. [106] showed that for chloride bath an increase in current density more than 2 Adm^{-2} resulted in poor current efficiency since hydrogen evolution reaction increased at higher applied current densities. With increasing applied current density, the crystal orientation index of the (1 1 0) plane decreased, but the crystal orientation index of the (2 0 0) and (2 1 1) planes increased.

Gow et al. [105] found that for a sulphate bath operated at 80˚C with pH 2.5, at current densities up to about 20 A dm^{-2}, an increasing number of defects, primarily dislocations,

were incorporated in the iron crystals and these accounted for the increase of internal stress in the electrodeposited foils. However, at current densities greater than about 20 A dm^{-2} there was an increasing number of grains which grow, probably in a dendritic manner, with relatively few defects, and this accounted for decreasing internal stress in the foils.

Generally, for chloride baths increasing the current density is reported to increase the hardness, yield and tensile strength of electrodeposited iron due to the grain refinement and increase in internal stress. However, less ductile deposits are produced at higher current densities since the internal stress increases [92,105,107,109].

Table 3.3 shows the mechanical properties of electrodeposited iron foils obtained from different baths with different operating conditions.

Table 3.3- Mechanical properties of iron deposits produced form different baths, adapted from Ref. [64].

Bath composition	pH	Temperature (˚C)	Current Density (A dm^{-2})	Tensile Strength (MPa)	Elongation (%)	Hardness
Sulphate bath	3.4	20	0.5			263
$Fe(NH_4)_2(SO_4)_2$	3.4	20	2			354
	4.4	19	0.5			182
	4.4	41	2			240 (Brinell)
Chloride bath	3.5-4.7	100-106	400	490-549	5-15	
$FeCl_2$: 120-150 g L^{-1}						
Chloride bath	0-3	86	20	441	2.1	
$FeCl_2.4H_2O$: 400 g L^{-1}		96	10	412	3.3	
$CaCl_2$: 80 g L^{-1}		96	20	421	4.7	
		96	30	421	5.5	
		108	20	353	2.7	
Chloride bath	0.2-0.4	70	15			450
$FeCl_2.4H_2O$: 465 g L^{-1}			5			300
H_3BO_3: 38 g L^{-1}			2.5			170
		95	15			150 (Vickers)
Sulphate-Chloride bath	2.5	80	8	452	4.3	
$FeSO_4.7H_2O$: 500 g L^{-1}			15	549	5.3	
NaCl: 50 g L^{-1}			27	627	2.7	
Deposits from either sulphate or chloride bath,					40	70-90 (Brinell)

annealed at 900˚C

3.6.1.6 Cathode

The material, microstructure, and surface roughness of the substrate are important parameters influencing the microstructure and properties of electrodeposits. Crichton et al [110] studied the effect of cathode surface roughness on properties of iron electroforms. The roughness of the face of the foil adjacent to the cathode surface was found to be the same as that of the electrode surface. The roughness of the anodic face of the foil, however, increased as the foil became thicker. The hardness of the cathodic face of the foil and Young's modulus were not affected by the roughness of the substrate, although the hardness of the anodic face of the foil increased with increasing cathode surface roughness, because a finer grain structure was produced. Tensile strength was therefore expected to increase with greater surface roughness but the results showed a slight decrease in tensile strength due to greater local stress concentrations suffered by the rougher foils on tensile testing.

Gomes et al. [111] studied the effect of substrate material including Ti and Ebonex® on morphology and crystallinity of iron sulphide electrodeposits. They found that although tetragonal iron sulphide, mackinawite, was electrodeposited on both substrates, film crystallinity and morphology were sensitive to the substrate material. A lattice contraction was observed for the deposit on Ebonex® when compared with the deposit obtained on titanium.

In electroforming process, the deposit is separated from its substrate after deposition and therefore the adhesion between the deposit and the substrate must be avoided. The cathode is selected and processed in such a way to minimize its adhesion to the deposited film. The mandrel surface should be conductive to transfer the electrical current required for electrodeposition. Non-conductor mandrels could be rendered conductive by the process of applying a metallic coating of silver, copper or nickel on their surface. This is generally carried out by spraying a reagent containing metal ions with a specific reducing agent on the mandrel surface by a double-nozzle gun. The chemicals react; the metal is reduced and is deposited on the mandrel surface [112]. There are basically two types of mandrels: those that can be removed intact from electroform, generally referred to as permanent mandrels,

and those that when removed from the electroform are in some way distorted or destroyed, called temporary mandrels [11]. The selection of mandrels depends on the shape and material of electrodeposits. A number of materials, both metallic and non-metallic, are used as permanent mandrels. The material chosen must be capable of being formed into the correct shape and dimensions and, in many cases, needs to be resistant to damage and corrosion. The material must not contaminate the solution in which the electroform is deposited. Suitable metallic materials include stainless steel (preferably an austenitic grade), copper, brass, mild steel, aluminum and its alloys, and electroformed or electrodeposited nickel [68].

3.7 Conclusions

Electroforming is a method for production of thin-walled metals which can be used as separate parts with different microstructures and properties. This method can be particularly interesting for production of stent tubes in a single-step process. The microstructure and properties of electroformed metals depend on the electroforming parameters including bath type, additives, pH, temperature, current density and cathode. Therefore, the desired mechanical and microstructural properties of stent materials can be potentially achieved by adjusting electroforming parameters. Electroformed metals have generally higher strength and hardness compared to wrought metals due to their fine grains, high density of structural defects and presence of internal stress. Although the high strength of electroformed metals can be considered as an advantage for a structural application as stent, their low ductility can be a limiting factor. Further heat treatment of electroforms is usually applied to remove their internal stress and increase their ductility. Iron is one of the metals which can be electroformed using different baths and applying parameters. Since the objective of this project is to produce pure iron with different microstructures in order to obtain higher mechanical properties and faster degradation than that of Armco® iron, electroforming is proposed as an ideal approach. Electroforming process can be optimized to produce iron foils with superior properties to those of Armco® iron in a single-step process.

Chapter 4. Electroformed iron as new biomaterial for degradable stents: Development process and structure–properties relationship

4.1 Résumé

Une technique d'électroformage a été développée pour la fabrication de feuilles de fer ciblées en vue d'une application comme matériau de stents cardiovasculaires biodégradables. La microstructure, les propriétés mécaniques et la corrosion des feuilles de fer électroformé ont été évaluées et comparées à celles du fer pur produit par moulage et traitement thermomécanique (CTT-Fe), à l'acier inoxydable 316L et à d'autres matériaux métalliques utilisés pour les stents biodégradables. L'analyse par diffraction d'électrons rétrodiffusés (EBSD) a révélé une granulométrie moyenne de 4 µm pour le fer électroformé, ce qui a produit une limite élastique de 360 MPa et une résistance à la traction (423 MPa) supérieure à celle des autres matériaux métalliques pour stents biodégradables. Un traitement thermique de recuit à 550°C a amélioré la ductilité du fer électroformé de 8% à 18%. Le taux de corrosion du fer électroformé mesuré par la polarisation potentiodynamique dans une solution de Hank est supérieur à celui du CTT-Fe, qui possède une dégradation in vivo lente. Les résultats ont montré que le fer électroformé possède une microstructure fine, de bonnes propriétés mécaniques et un taux de corrosion modéré en tant que matériau pour stents dégradables.

4.2 Abstract

An electroforming technique was developed for fabricating iron foils targeted for application as biodegradable cardiovascular stent material. The microstructure, mechanical properties and corrosion of electroformed iron (E-Fe) foils were evaluated and compared with those of pure iron made by casting and thermomechanical treatment (CTT-Fe), with 316L stainless steel (316L SS) and with other candidate metallic materials for

biodegradable stents. Electron backscattered diffraction revealed an average grain size of 4 μm for E-Fe, resulting in a high yield (360 MPa) and ultimate tensile strength (423 MPa) being superior to those of other metallic biodegradable stent materials. Annealing at 550ºC was found to improve the ductility of the E-Fe from 8% to 18%. The corrosion rate of E-Fe in Hanks' solution, measured by potentiodynamic polarization, was higher than that of CTT-Fe, which had been found to have a slow *in vivo* degradation. The results showed that E-Fe possesses fine-grain microstructure, suitable mechanical properties and moderate corrosion rate as a degradable stent material.

4.3 Introduction

Cardiovascular stenting is a catheter-based procedure in which a tiny, expandable wire mesh tube (stent) is intravascularly implanted, X-ray placed and deployed in a diseased artery, serving as a scaffold to hold it open. Current stent technology is based on the use of permanent implants made of corrosion-resistant materials such as 316L SS and Nitinol. These permanent implants are intended to remain in the vessel wall for life, mainly because they cannot be removed without causing irreversible damage to the heart. However, it has been shown that the scaffolding effect of stents for prevention of the artery occlusion and arterial remodeling is only required for a set timeframe (6–12 months), and the permanent presence of stents would not provide any further benefit [23]. Therefore, development of biodegradable stents which provide the scaffolding effect and thereafter degrade could be the logical approach to avoid the potential complications observed with permanent stents [23,38]. In the search for biodegradable stent material, several polymers have been evaluated *in vivo*. However, polymers have special drawbacks, including low mechanical properties and inflammatory response, which limit their application as stents [22]. Magnesium alloys, iron–35% manganese alloy (Fe–35Mn) and pure iron are metallic materials which have been investigated for biodegradable stent application [5,6,10,37,39]. Magnesium alloys (AE21 and WE43) have been implanted in porcine models and in clinical studies in humans [37,39]. The implantation results showed that further improvements are required to lower the degradation rate and to increase the mechanical properties of Mg alloys [22,37,39]. Recently, Fe–35Mn alloy developed by powder metallurgy has been evaluated in vitro. It has shown good mechanical properties and slower degradation than Mg alloys and is currently under

further development [10]. Pure iron made by casting and thermomechanical treatment (CTT-Fe) has been implanted in rabbit and porcine models. The results showed that iron had good biocompatibility and superior mechanical and degradation properties compared with Mg alloys. However, *in vivo* degradation of pure iron was slower than the calculated value from in vitro degradation tests. It was suggested that structural or compositional modifications should be made to iron to obtain higher *in vivo* degradation rates [5,6]. In this work, the feasibility of producing electroformed iron (E-Fe) suitable for application as a biodegradable material for stents was investigated. The following are the main reasons for such investigation: (1) Iron ion (Fe^{2+}) is an essential element for the body. It is an essential component of a variety of enzymes. Transport, absorption and storage mechanisms for iron are also well known and make iron and iron-based alloys favorable candidates as biodegradable implant material [5]. (2) Iron has also shown moderate and uniform degradation, which is required for biodegradable stents to avoid the mechanical failure of the device in vessels [5,45]. (3) The mechanical properties of iron are also comparable with those of 316L SS and other stent materials. (4) One of the aims of this work was to modify the microstructure of pure iron to produce a material with a higher degradation rate and mechanical properties superior to those of CTT-Fe. Therefore, the fabrication method selected for production of iron was electroforming. This method uses the electrodeposition principle to produce complex metallic parts and components [11]. While electrodeposition is used to modify the surface of a substrate material by deposition of a metallic coating, in electroforming a metallic part is deposited to be used as a separate entity. As the structure of metallic parts is formed atom layer by atom layer, electroforming is an ideal process for fabrication of complex shapes and surfaces with dimensional precision, thin-walled materials and high-purity metals with different microstructures, thicknesses and properties [11,113]. Also, electroforming produces polycrystalline metals with exceptionally fine-grain structure with grain sizes much smaller than in bulk metals produced by other production methods. The microstructure of electroformed metals could be tailored by adjusting the electrodeposition parameters, including current density, electrolyte composition, pH and temperature [11].

Applications for electroforming include precious tools, mesh and foil products, space mirrors, metal optical parts, bellows, radar and wave guides, and micro-electromechanical

systems using LIGA and SU-8 processes [13,109]. The most common current application of E-Fe is the production of foils used in microelectronic devices and electromagnetic recording devices [92,114].

In this work, E-Fe was investigated as a structural material for biodegradable cardiovascular stent application. Electroformed Fe specimens were fabricated in flat form to facilitate the study of microstructure, mechanical properties and corrosion behaviour. After deposition, the foils were removed from their substrate and evaluated. The properties of E-Fe compared with those of CTT-Fe, Mg alloys, Fe-35Mn alloy, which have previously been studied as biodegradable stent materials, and 316L SS, which is the gold standard material for cardiovascular stent fabrication.

4.4 Materials and methods

4.4.1 Specimen fabrication by electroforming

A ferrous chloride–calcium chloride aqueous solution was used as electrolyte for iron electroforming. The electrolyte was prepared by dissolving $FeCl_2$ (Alfa Aesar, MA, USA) and $CaCl_2$ salts (Alfa Aesar, MA, USA) in deionized water. The composition of the bath was 400 g L^{-1} $FeCl_2$-80 g L^{-1} $CaCl_2$, which is known as Fischer-Langbien solution and is reported to produce more ductile iron foils compared with other electrolytes [64]. One gram per litre of sodium saccharine and 0.25 gram per litre of sodium dodecyl sulfate were added to the electrolyte as stress-reducing and anti-pitting agents, respectively. Ti6Al4V titanium alloy was selected as the substrate because it can be separated easily from deposits after electrodeposition. The substrate had a rectangular surface area of 14 cm^2, which was mechanically polished with 120-3000 grit SiC abrasive paper and then with 0.05 μm alumina paste for a mirror-like finish prior to electrodeposition. Armco-iron sheet was used as a soluble anode to provide Fe^{2+} ions in the electrolyte. The solution pH was adjusted to 1 with the addition of HCl and NaOH, and the temperature was kept at 90˚C. Electrodeposition were carried out for 4.5 h with a direct current density of 2 A dm^{-2}, which was found to produce Fe foils with the lowest surface roughness. The deposition time was calculated based on Faraday's law in order to obtain films 100 μm thick. Figure 4.1 shows a schematic of the electrodeposition cell used in this work. Iron films 100 μm thick were

deposited on the titanium alloy substrate and removed after electrodeposition. To study the effect of heat treatment on properties, Fe foils were annealed at 550 and 650˚C for 1 h in high-purity argon atmosphere. The annealing temperatures were selected to be higher than the recrystallization temperature of pure iron, which is 450˚C [115]. It has also been reported that annealing of E-Fe at 550˚C for 1 h removed the internal stress produced by electrodeposition and improved ductility [105].

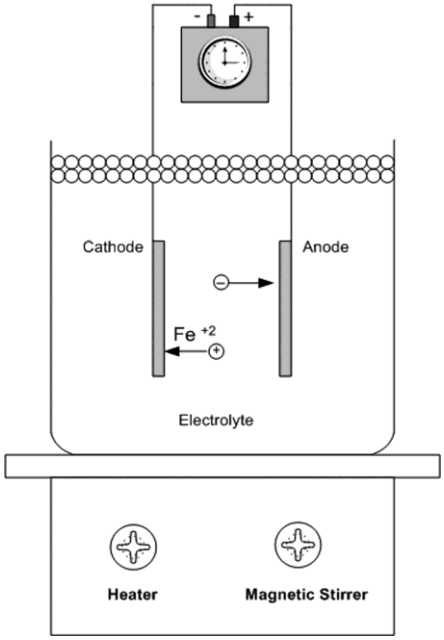

Figure 4.1- Schematic of electroforming apparatus

In order to compare the microstructure, mechanical properties and corrosion behaviour of E-Fe with those of CTT-Fe, pure Fe foils with similar thickness to those of E-Fe (Fe > 99.9, 0.125 mm thick, as-rolled, Goodfellow, USA) were annealed at 550˚C and tested along with the E-Fe foils.

4.4.2 Composition, phase and morphology characterization of E-Fe

The chemical composition of E-Fe was measured using inductively coupled plasma and the fusion gas analysis method, by means of a LECO TCH-600 gas analyzer according to ASTM D1976 [116] and E1019 [117] standards, respectively. The surface morphology and cross section of E-Fe were observed using scanning electron microscopy (SEM; JOEL JSM-840A). For cross-section observation, an E-Fe specimen was mounted in acrylic resin and

polished using 1000-4000 SiC paper and then 0.05 μm alumina paste. Phase analysis of the specimens was carried out by X-ray diffraction (XRD) using a Siemens D5000 diffractometer with Cu Kα radiation at a scanning rate of 1 min^{-1}. The roughness (Ra) of EFe was measured using a Dektack 3 surface profiler. A 1 mm length of the surface was scanned for each measurement, giving 400 data points.

4.4.3 Grain size measurements

4.4.3.1 Methods and sample preparation

The microstructure of as-deposited and annealed Fe foils was studied using SEM and electron backscattered diffraction (EBSD). Before microstructure observation, Fe foils were mounted in acrylic resin and polished with 1000–4000 SiC paper and then with 0.05 μm alumina paste. A 2% nital solution was used to etch the surface prior to SEM observation. For EBDS characterization, the samples were observed as-polished without etching. The average grain size identification of SEM micrographs was performed using image analysing software by Clemex Technology Inc.

4.4.3.2 Study of microstructure changes in E-Fe by SEM and XRD

Since the microstructure of E-Fe could not be revealed using SEM, indirect methods were used for characterization. E-Fe foils were annealed at 250, 350, 450 and 550˚C for 1 h in a high-purity argon atmosphere to reveal the microstructural changes with heat treatment.

4.4.3.3 SEM observation of E-Fe annealed at 550 and 650˚C and CTT-Fe

SEM secondary electron imaging was performed for the samples, and the microstructure was analysed for grain size measurement.

4.4.3.4 XRD orientation study

XRD patterns of samples annealed at each temperature were also obtained for crystalline orientation studies. To identify the preferred orientation of each sample, the orientation

index (M) of each plane was calculated based on the following equations [106] (example for (1 1 0) plane):

$$IFR\ (1\ 1\ 0) = IF\ (1\ 1\ 0)/[IF\ (1\ 1\ 0) + IF\ (2\ 0\ 0) + IF\ (2\ 1\ 1)] \quad \textbf{Equation 4-1}$$

$$IF_{exp}\ (1\ 1\ 0) = I\ (1\ 1\ 0)/[I\ (1\ 1\ 0) + I\ (2\ 0\ 0) + I\ (2\ 1\ 1)] \quad \textbf{Equation 4-2}$$

$$M\ (1\ 1\ 0) = IF_{exp}\ (1\ 1\ 0)/\ IFR\ (1\ 1\ 0) \quad \textbf{Equation 4-3}$$

where *IFR* is the XRD intensity ratio for JCPSD card of BCC iron, IF_{exp} is the intensity ratio for the experimental XRD pattern and M is the calculated orientation index. where *IFR* is the XRD intensity ratio for the JCPSD card of body-centred cubic (bcc) iron, IF_{exp} is the intensity ratio for the experimental XRD pattern, and *M* is the calculated orientation index.

4.4.3.5 Orientation imaging microscopy of E-Fe by EBSD

Orientation imaging microscopy (OIM) was performed using EBSD to establish accurately the specific orientation of individual grains in polycrystalline electrodeposited iron foils. OIM maps were generated using a computer software program by TSL-EDAX from backscattered electron Kikuchi patterns collected by SEM (SUPRA 55 VP-Zeiss scanning electron microscope). The grain size distribution analysis was performed using the orientation images obtained.

4.4.4 Mechanical properties

For mechanical testing, dog-bone-shaped specimens with gauge width 6 mm, thickness 0.1mm, gauge length 30 mm and total length 100 mm were cut from 14 cm^2 iron foils. Uniaxial tensile tests were conducted at room temperature using a computer-controlled Instron MicroTester-5848 with specially designed clamping for thin specimens. The load cell capacity was 1 kN, and the strain was measured based on the elongation of the marked gauge length during the test, using a video camera. Tensile test was performed according to ASTM standard E8 [118] with a strain rate of $5.6 \times 10^{-4}\ s^{-1}$. For each type of material, five specimens were tested, and the mean value and standard deviation were calculated.

4.4.5 Corrosion testing

A potentiodynamic polarization (ASTM G59–97) test [52] was carried out to identify the corrosion rate of E-Fe, using a Princeton Applied Research Model 273 galvanostat/potentiostat. Iron foils were cut to pieces with surface area 1 cm^2 and mounted in acrylic resin. The surface was then polished with 4000 grit SiC paper and 0.05 μm alumina paste prior to electrochemical testing. Corrosion tests were performed in Hanks' modified solution, which simulated the ionic composition of blood plasma. The solution was prepared by dissolving Hanks' modified salt (H1387, Sigma Aldrich, USA) in deionized water. The solution temperature and pH were adjusted to 37 ± 1˚C and 7.4, respectively, during the tests. Corrosion tests were performed at the scanning rate of 0.166 mV s^{-1} and applied potential range -1 to -0.5 V, since the corrosion potential of iron was predicted to be in this range, based on previous studies [45]. A conventional three electrode cell was used with a platinum counter electrode 1 cm^2 in surface area, a saturated calomel reference electrode and the prepared Fe working electrodes. The corrosion rate was calculated according to the corrosion current density (i_{corr}) obtained using Equation 4-4 [52]:

$$CR = - \frac{EW}{\rho}$$ **Equation 4-4**

In this equation, CR is the corrosion rate (mm $year^{-1}$), i_{corr} is the corrosion current density (μA cm^{-2}), EW is the equivalent weight (27.92 g/eq for Fe), and ρ is the material density in grams per cubic centimeter (7.87 for Fe). For each type of material, five specimens were tested using the same conditions, and the mean value and standard deviation were calculated.

4.5 Results and discussions

4.5.1 Specimen fabrication

The electroforming method developed produced iron foils 100 μm thick in a single-step process. The foils were removed mechanically from the Ti alloy cathode.

4.5.2 Composition and microstructure characterization

The compositions of the impurity elements found in E-Fe are presented in

Table 4.1. Atomic concentration of the impurities was calculated from their weight concentration. Although the concentration of metallic impurities is low in weight and atomic percent, non-metallic impurities are relatively higher in atomic concentration. These impurities could incorporate into the iron film during electrodeposition. The presence of a fairly large amount of hydrogen and its role in the reduction of ductility in electrodeposited metals is a well-known fact [67]. Hydrogen co-deposits with iron as a result of cathodic reaction, and its concentration could reach 0.0045-0.013 wt.% [119]. Although the amount of hydrogen detected in this study is below the reported values for electrodeposited iron [119,120], it should be considered a reason for the relatively low ductility of iron.

Table 4.1- Concentration of impurity elements in E-Fe.

Element	O	H	N	C	Mn	Si	Ti	Al
Wt. %	0.095	0.0026	0.083	0.050	0.002	0.010	0.005	0.010
At. %	0.329	0.143	0.329	0.231	0.002	0.020	0.006	0.020

The XRD pattern (Figure 4.2) confirmed the formation of crystalline α-iron with bcc structure as the only detectable phase in the electroformed material compared to JCPDS standard No. 06-0696 for BCC-α-iron.

Figure 4.3 shows the surface morphology and cross-sectional view of E-Fe foil. The cross-sectional image shows the uniform thickness of the foil. The roughness of the cathodic face is lower than that of the anodic face, since it simulates the surface structure of titanium alloy substrate. The roughness of the anodic surface E-Fe deposited at a current density of 2 A dm^{-2} was ~1.5 μm based on the performed measurements. Electrodeposits obtained at higher current densities (4 and 8 A dm^{-2}) appeared much rougher, with a nodular surface structure, and were excluded from further analysis. It has been shown that higher current densities lead to the formation of deposits with higher roughness and heterogeneous surface morphology [121]. Therefore, a current density of 2 A dm^{-2} was selected for this study.

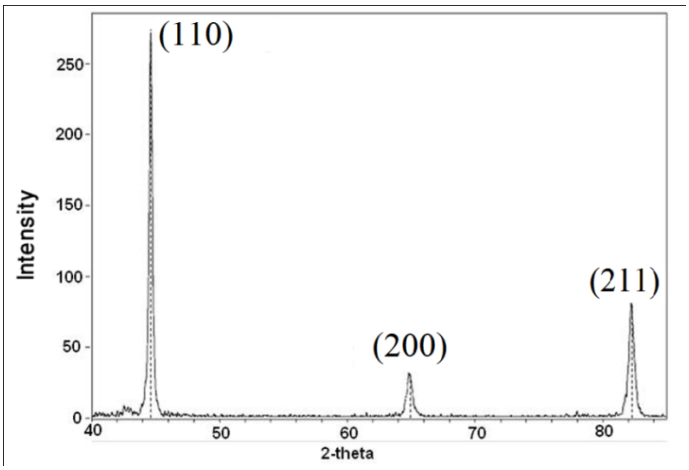

Figure 4.2- XRD pattern of E-Fe: all peaks correspond to α-Fe.

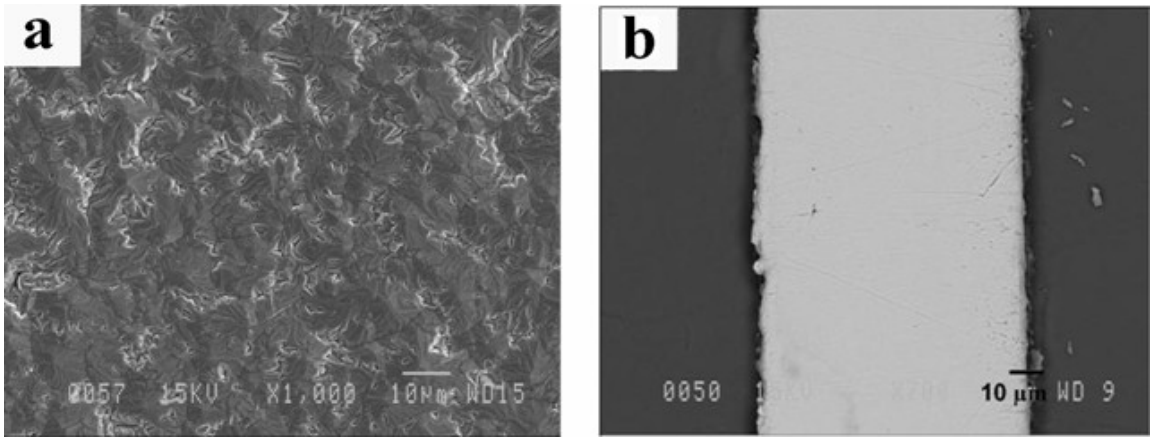

Figure 4.3- Electroformed iron a) surface morphology, b) cross section of E-Fe showing its uniform thickness.

4.5.3 Microstructure and grain size measurement

The grain structure of as-deposited Fe could not be revealed after metallographic preparations including mechanical polishing and etching using different solutions. Fine-grain microstructure and/or preferred orientation of the grains were the two possible reasons for this observation.

4.5.3.1 SEM observation of E-Fe with heat treatment

Figure 4.4 shows the microstructural changes in E-Fe as the annealing temperature increased. As the images show, the grain boundaries could not be identified in as-deposited Fe and E-Fe annealed at 250˚C. However, when the temperature reached 350˚C, grain boundaries started to appear, as shown by arrows in the micrograph. This can be a sign of recovery and recrystallization of E-Fe due to the heat treatment. At 450˚C, small grains could be seen, as indicated in the images. However, the grain size could not be identified, since the grain boundaries were not completely revealed. For the specimen annealed at 550˚C, the grains appeared with an average grain size of 6 μm.

4.5.3.2 XRD analysis of E-Fe with heat treatment

Figure 4.5 presents an orientation index, and Figure 4.6 shows full-width at half maximum (FWHM) intensity data for XRD patterns related to E-Fe samples annealed at 250-550˚C. For E-Fe, the highest orientation index belongs to (110) planes. This is in agreement with previous research on the orientation of electrodeposited Fe. Yoshimura et al. [106] stated that the higher the temperature of the electrolyte solution, the lower the applied current density, which is the case for the present study, producing iron films with large grains with the preferred orientation index plane of (110) promoting crystal growth. As E-Fe foil was annealed at 350˚C, the orientation index of the (110) plane decreased, while those of the (220) and (211) planes increased. The change in the orientation index can be related to the initial recrystallization of as-deposited Fe by annealing.

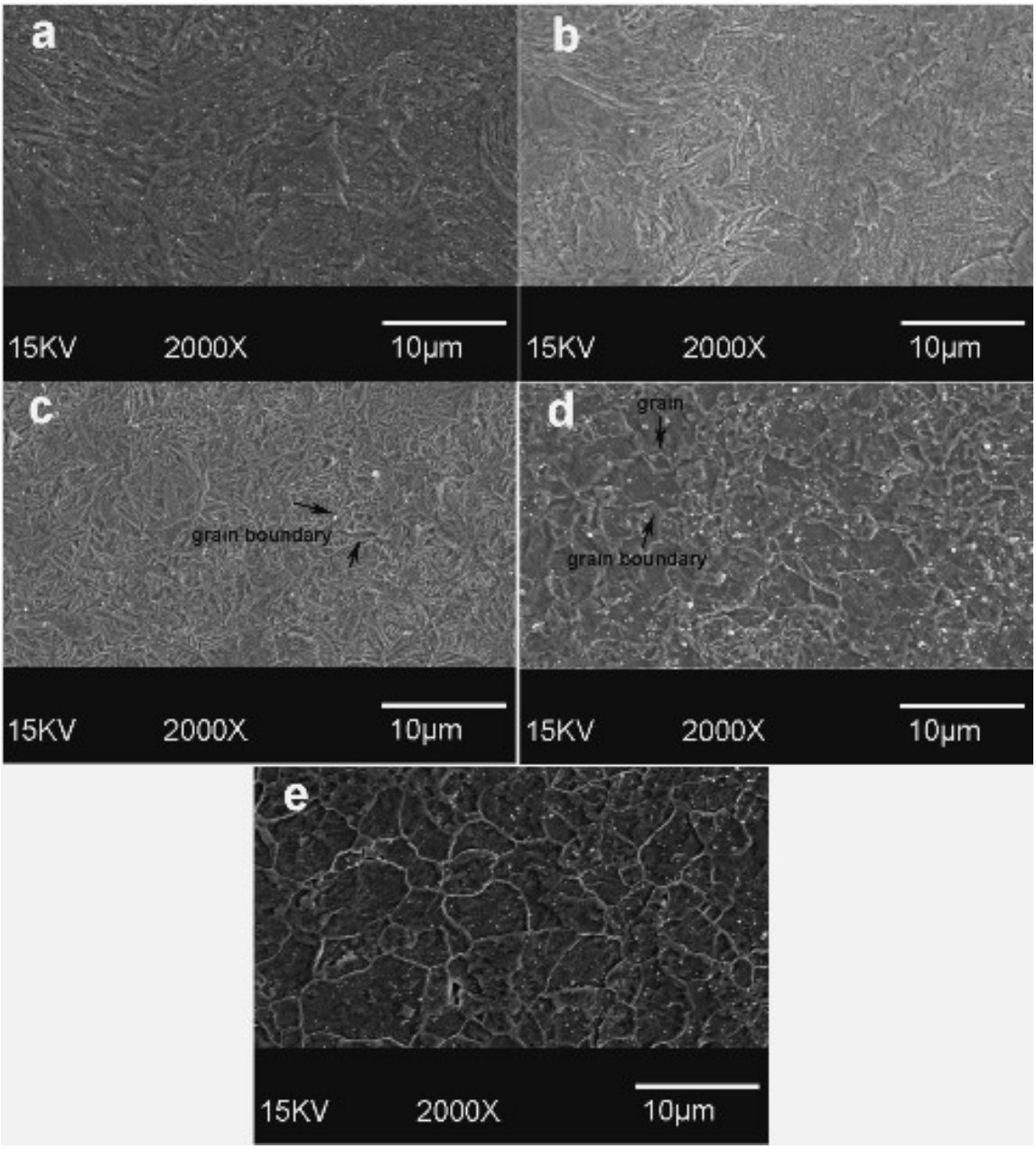

Figure 4.4- SEM micrograph E-Fe: (a) as-deposited; (b) annealed at 250ºC; (c) at 350 ºC; (d) at 450ºC; (e) 550 ºC. The structural reorientation and appearance of grain boundaries is shown.

Electrodeposited metals can undergo recovery at lower temperatures and recrystallization at higher temperatures when annealed, and this can change their texture [77,122-124]. The appearance of grain boundaries in Figure 4.4 (c) could be evidence of these microstructural changes. Increasing the annealing temperature to 450˚C resulted in an important change in the texture of E-Fe, as the highest orientation index was related to the (211) plane and the

index of the (110) notably decreased. The related microstructure in Figure 4.4(d) shows the appearance of small grains and a different texture from that of as-deposited Fe, which can be considered evidence of recrystallization. Although the recrystallization temperature of electrodeposited iron was reported to be ~500˚C [125], the present SEM micrographs and XRD texture changes suggest that it may occur at lower temperatures. It has been shown that recrystallization of 35-μm-thick electrodeposited copper foils starts at 170˚C and is completed at 325˚C. The mechanism of electrodeposited copper recrystallization is speculated to be subgrain rotation and subgrain boundary migration due to the defect-saturated microstructure of electrodeposits, which decrease the activation energy of recrystallization by a factor of two or three compared with that of wrought copper [77]. Ebrahimi et al. [124] also reported that recrystallization of electrodeposited copper started at 150˚C, whereas in cold-rolled copper, recrystallization was not observed at temperatures <450˚C. For electroformed Fe annealed at 550˚C, the orientation index of the (110) plane increased to 1.25, showing that the highest intensity was related to the (110) plane, while the index of the (211) plane is higher than that of as-deposited Fe, showing that annealing at this temperature led to a weaker texture. Since the grains could be seen in the SEM micrograph (Figure 4.4(e)), recrystallization and partial grain growth could be speculated for the sample.

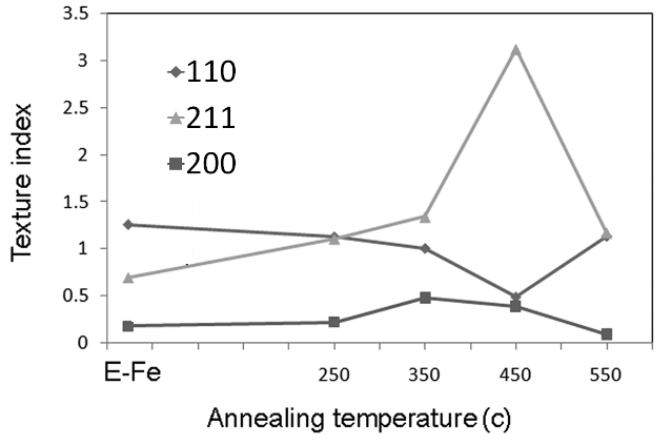

Figure 4.5- XRD texture orientation index of as-deposited and annealed Fe.

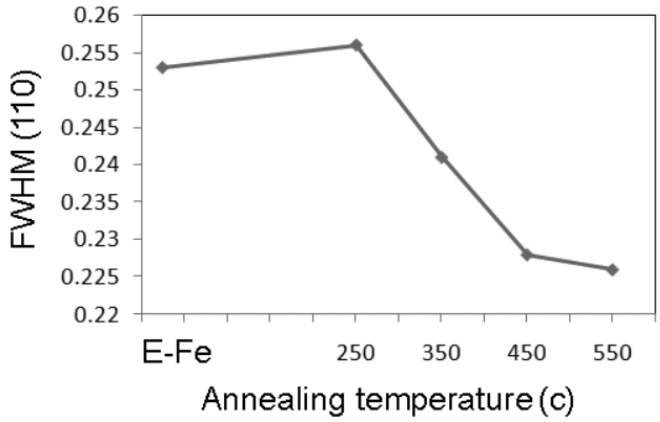

Figure 4.6- FWHM of (1 1 0) peak of E-Fe and E-Fe annealed at different temperatures obtained from XRD patterns.

The FWHM values of the (110) peak of as-deposited Fe and E-Fe annealed at different temperatures are shown in Figure 4.6. Although FWHM increases slightly on annealing at 250˚C, it decreases on annealing at higher temperatures. The nanometric grain size and internal stress of electrodeposits are considered the two main reasons for broadening of XRD peaks. Since the present results show that grain size was in the range of microns, the decrease in FWHM by annealing could be attributed mainly to the release of internal stress and recovery of as-electrodeposited Fe.

4.5.3.3 OIM of E-Fe by EBSD

Figure 4.7 illustrates the grain orientations for E-Fe foil from the normal direction to the surface (left) and cross section (right) as the inverse pole plot map. The colour-coded triangle map below the cross-section image illustrates that different colours belong to different grain orientations, while the grain distribution chart is presented below the surface microstructure. The black zones in the orientation maps belong to the area with no EBSD detection. It is clear from the image that the surface shows a very strong <111> fibre texture, and only a small number of <001> and <010> grain directions are present. This observation of the highly oriented texture in E-Fe explains why the grain structure was not revealed by SEM and OM. EBSD image analysis indicated a Gaussian grain distribution

consisting mainly of 4-μm-diameter grains, which could be suggested as the average grain size. An average grain size of 4 μm of E-Fe could be considered large for an electrodeposited metal. This could be mainly due to the electroforming conditions, including low current density, high deposition temperature and long deposition time (or formation of a thick deposit of 100 μm), which increase grain growth rather than nucleation and favour coarser microstructure [106].

The cross-section orientation map of E-Fe shows the formation of columnar grains and a few equiaxed grains in E-Fe, which is common in electrodeposited metals. The axes of the columnar grains are parallel to the growth direction of the deposit and extend to almost the entire thickness of the foil, with a length of ~60 μm for some grains. It could be concluded that E-Fe foil has a highly oriented columnar growth perpendicular to the cathode surface. Elevated temperatures and low current densities permit the migration of atoms to sites where they can be incorporated into the existing structure [64]. As the columnar formation takes place, island nuclei separated from one another by zones with high impurity content cannot grow together and grow preferably in the direction normal to the film plane [126]. According to geometrical selection theory, the formation of texture in electrodeposits is attributed to the difference in growth rates of different planes and also the coating surface morphology. Based on this theory, there are two different modes for energetically favourable growth: one is an outward growth mode, and the other is a lateral growth mode. In the outward growth mode, grains bounded by slow growing faces, which are perpendicular to the substrate, may grow preferentially. In contrast, in the lateral growth mode, the grains bounded by slow-growing faces, which are parallel to the substrate, may grow preferentially [127]. It has been pointed out that the mode of transport of the depositing ion is an important factor in determining whether the growth mode is outward or lateral. If the metal ion is transported to the cathode by migration under the influence of an electric field, there is a tendency for deposition in a direction normal to the substrate surface and therefore, outward growth. In the bath which was used for the electrodeposition of iron, the current was carried mainly by ferrous ions whose mode of transport is, therefore, essentially by migration. Hence, iron would also grow under the influence of an outward growth tendency [128].

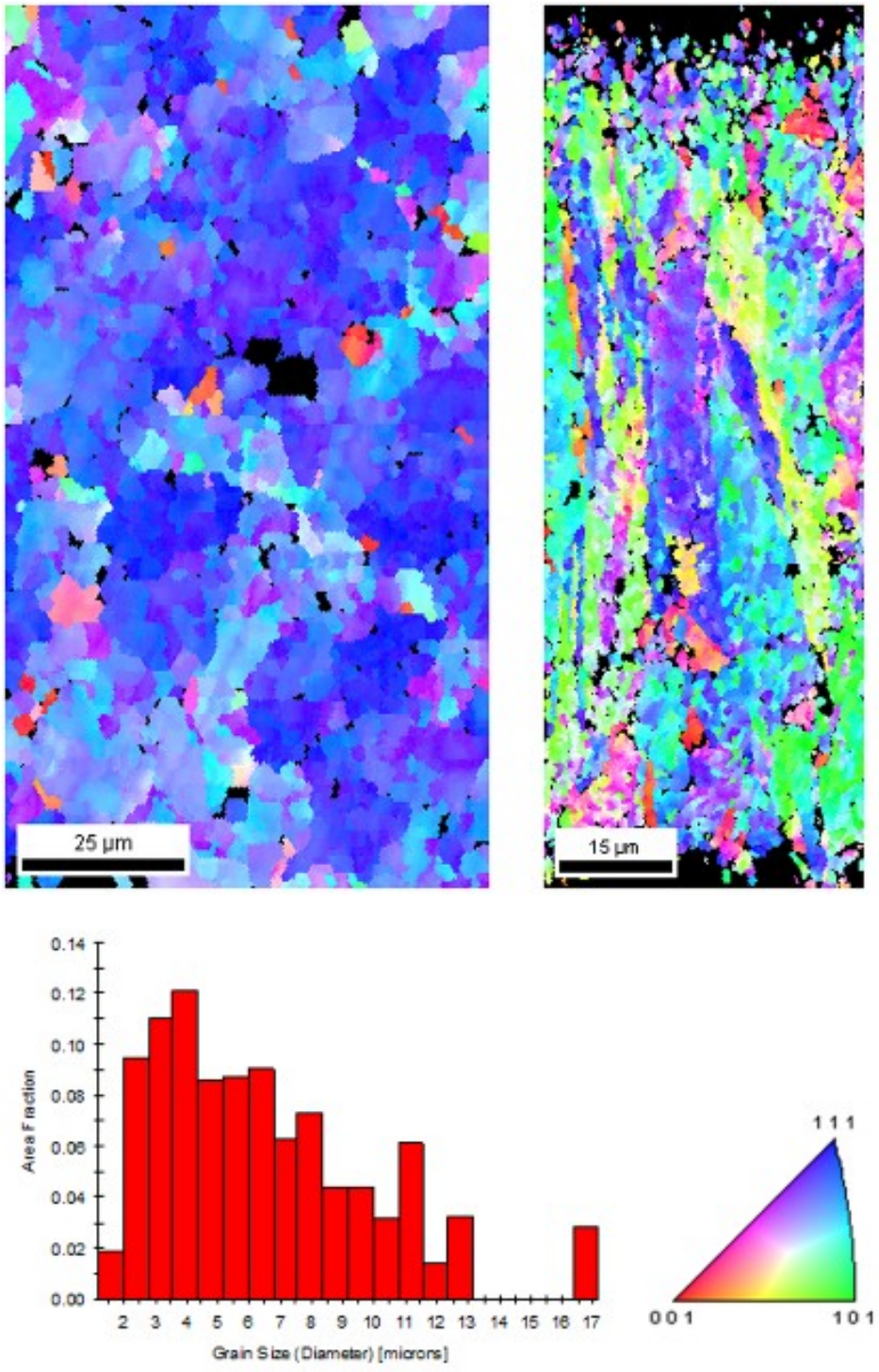

Figure 4.7- EBSD orientation map of E-Fe: surface microstructure (left) and cross section (right). The grain size distribution chart shows that the average grain size is 4 µm. Colour-coded map (triangle) shows different colour codes relating to different orientations.

4.5.3.4 Microstructure and grain size in annealed E-Fe compared with CTT-Fe

SEM micrographs of E-Fe annealed at 550 and 650˚C and CTT-Fe are shown in Figure 4.8. The microstructure of E-Fe annealed at 550˚C shows two types of grains, including a large number of finer grains < 6 μm and a few grains >10 μm (Figure 4.8(a)). Although the presence of large grains could be a sign of partial grain growth in E-Fe after annealing, the average grain size of the annealed sample was not significantly higher than that of as-deposited Fe. This can be a sign of recrystallization, as discussed in Section 3.3.3.2. Electrodeposition generates internal stress and crystal defects which increase the stored energy of fabricated metals. The stored energy could result in recrystallization and the formation of new defect free grains in metals during annealing [77]. When the iron foils were heated to 650˚C, a significant grain growth was observed with an average grain size of 15 μm (Figure 4.8(b)). The microstructure shows a bimodal grain distribution of larger grains and a few smaller grains. The presence of large grains confirms that, when heated at 650˚C for 1 h, the microstructure of E-Fe undergoes both recrystallization and significant grain growth.

In contrast to the fine-grained microstructure of E-Fe annealed at 550˚C (6 μm), Figure 4.8(c) shows a much coarser microstructure for CTT-Fe annealed under the same conditions, with an average grain size of 25 μm. This difference shows the capacity of electrodeposition for the production of iron foils with fine-grain microstructure in a single-step fabrication method.

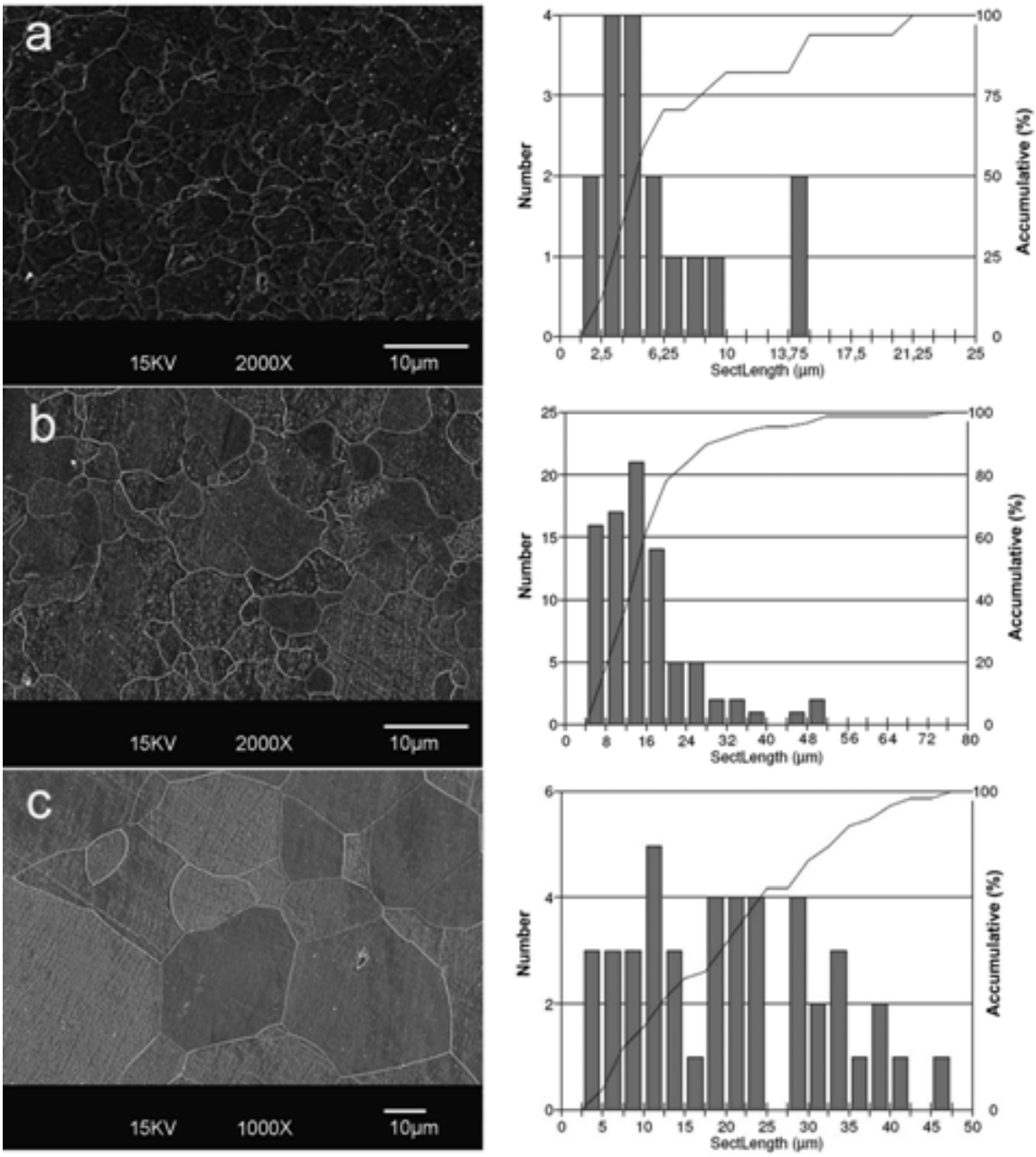

Figure 4.8- Microstructure and grain size distribution of: (a) E-Fe annealed at 550˚C, average grain size 6 µm; (b) E-Fe annealed at 650˚C, average grain size 15 µm; (c) CTT-Fe annealed at 550˚C, average grain size 25 µm.

4.5.4 Mechanical properties

The stress–strain curves of E-Fe, annealed E-Fe (AE-Fe) and annealed CTT-Fe are presented in Figure 4.9, and the related mechanical properties are summarized in Table 4.2. E-Fe shows high 0.2% offset yield strength (σ_y) of 360 MPa, and ultimate tensile strength

(σ_{UTS}) of 423 MPa, compared with the reported values for iron fabricated by CTT [56]. In electroformed metals, defects are primarily dislocations, twins and codeposited foreign atoms or molecular groups. The density of dislocations approaches that of heavily plastically deformed metals and can have an important influence on mechanical properties [77,115,122,123]. Therefore, a high yield and tensile strength of E-Fe can result from obstructions of dislocation movement by other dislocations, codeposited foreign materials, and twin and grain boundaries. Also, the fine grain size of E-Fe provides more grain boundaries, which act as barriers to dislocation motions based on the Hall-Petch law and subsequently increase σ_y. However, the elongation of E-Fe reached a value of only 8%. The low ductility of electrodeposited metals has been generally attributed to the high internal stress and crystal defects produced by electrocrystallization and hydrogen embrittlement caused by the incorporation of hydrogen in the structure as part of the cathodic reactions in electrodeposition [75,105].

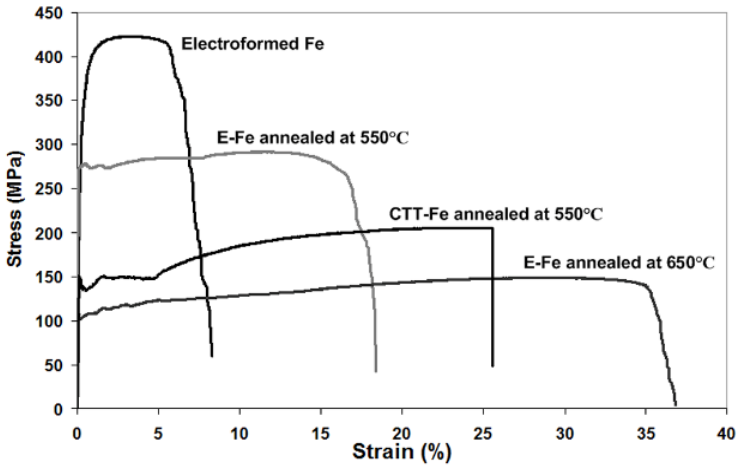

Figure 4.9- Tensile test curves for E-Fe (as-electroformed, annealed at 550˚C and annealed at 600˚C) and CTT-Fe annealed at 550˚C.

When electroformed Fe was annealed at 550˚C, the elongation increased from 8% to 18% which is a result of stress-relief and recrystallization, while yield and tensile strength values decreased to 270 and 292 MPa, owing to the formation of defect-free grains caused by the heat treatment, resulting in easier dislocation movement. As the annealing temperature increased to 650˚C and the average grain size reached 15 µm, the elongation improved to 35%, although σ_y and σ_{UTS} decreased more significantly. The decrease in the strength of

annealed iron is obviously because of its coarser grains. This coarsening of the new strain-free grains results in an improvement in ductility.

For CTT-Fe annealed at 550˚C, σ_y is almost half that of AE-Fe, which could be attributed to its much coarser microstructure (25 vs 6 μm). The ultimate tensile strength of annealed CTT-Fe is also lower than that of AE-Fe, while its elongation is higher (25% vs 18%). The lower ductility of E-Fe could be related to the presence of defects produced by electroforming.

Based on the results of the tensile test on electroformed and pure CTT iron, it could be concluded that electroformed Fe annealed at 550˚C exhibits interesting mechanical properties, with optimum σ_y and σ_{UTS}, and elongation. It provides higher σ_y than pure CTT iron, Mg alloys and Fe-35Mn alloys which have been studied as biodegradable stent material. In spite of its lower ductility compared with pure CTT iron and Fe-35Mn, AE-Fe shows greater elongation than Mg alloys and is acceptable to be used as a cardiovascular stent material.

Table 4.2- Mechanical properties of iron and other candidate materials for cardiovascular stent fabrication.

Material	Yield Strength (MPa)	Tensile Strength (MPa)	Elongation at break (%)
Electroformed Fe	360 ± 9	423 ± 12	8 ± 2
Electroformed Fe-Annealed at 550 ºC	270 ± 6	292 ± 14	18 ± 4
Electroformed Fe-Annealed at 600 ºC	130 ± 7	169 ± 9	32 ± 5
Pure Fe- Annealed at 550 ºC	140 ± 10	205 ± 6	25 ± 3
Fe-35Mn (annealed) alloy [10]	235	550	31
Mg alloy WE43 (tempered) [56]	162	250	2
SS 316L (annealed) [56]	250	580	55

4.5.5 Corrosion testing

Potentiodynamic polarization curves of E-Fe, AE-Fe (at 550˚C) and annealed CTT-Fe (550˚C) are presented Figure 4.10. Polarization curves show that the corrosion potential of

E-Fe is the lowest, and that of CTT-Fe is the highest. This is consistent with the corrosion current density values obtained for the three materials. The corrosion rates of the materials calculated from their corrosion current densities (based on Equation 4-4) are presented in Table 4.3. E-Fe had the highest corrosion rate of 0.85 mm year^{-1}, which was reduced by annealing at 550˚C to a value of 0.51 mm year^{-1}. CTT-Fe showed the lowest corrosion rate of 0.16 mm year^{-1}, which is consistent with previous work on the corrosion of iron fabricated by CTT [45]. These results confirmed that electrodeposition is able to produce iron foils with higher corrosion rates, which can facilitate the biodegradation of stents for 6-12 months after implantation.

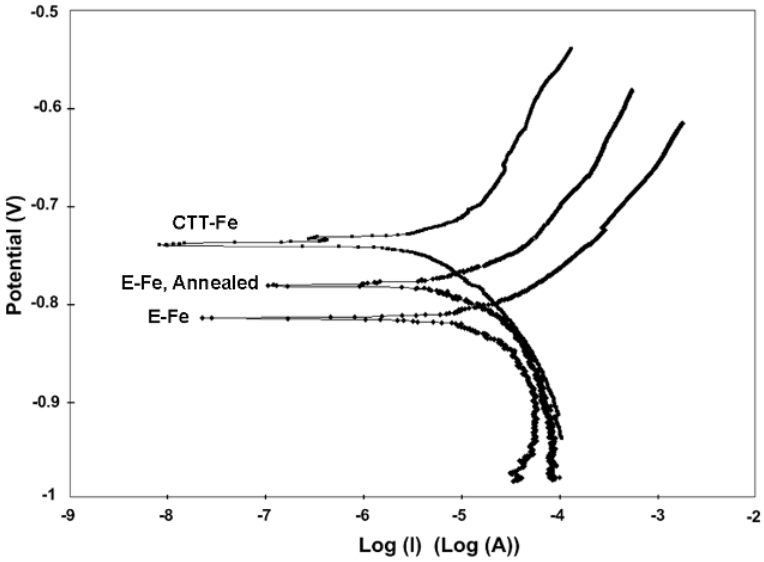

Figure 4.10- Potentiodynamic polarization curves for iron: CTT-Fe annealed at 550˚showed the highest corrosion potential and the lowest corrosion current, while E-Fe had the lowest corrosion potential and the highest corrosion current.

This higher corrosion rate is related to the fine microstructure of the electroformed material, with smaller grains and a higher volume of grain boundaries, which have higher potential for corrosion and act as active sites for faster degradation. Also, microstructural defects and the strong preferred texture produced by electroforming initiate corrosion reactions and increase the general corrosion rate of E-Fe compared with CTT-Fe. For many materials, the susceptibility of single crystals to corrosion has been shown to be related to crystallographic orientation. In the case of bcc Fe, crystals of the close-packed planes of

(110) have been found to be the most susceptible to corrosion [129]. Therefore, preferred grain orientations may play a role in the higher degradation rate of E-Fe. The suggested reasons for the slower corrosion rate of AE-Fe compared with E-Fe are the lower internal stress, the smaller number of strained grains and fewer defects than E-Fe, which give it lower potential for corrosion and a more moderate corrosion rate.

Table 4.3- Potentiodynamic polarization data of electroformed and pure Fe extracted from polarization curves.

Material	i_{corr} (μAcm^{-2})	CR (mm $year^{-1}$)	Corrosion potential (mV)
E-Fe	73.4 ± 4.2	0.85 ± 0.05	-824 ± 18
E-Fe - annealed	44.3 ± 5.8	0.51 ± 0.06	-776 ± 20
CTT-Fe - annealed	14 ± 1.3	0.16 ± 0.04	-732 ± 16
Fe-35Mn alloy [6]	36.6 ± 3.4	0.44 ± 0.04	-740
AM60B-F Mg alloy [9]	406	2.78	-1750

4.6 Conclusions

The electroforming technique developed provided a simple way of producing Fe without requiring the equipment and the energy consumption of the CTT method. E-Fe possesses a highly textured and fine-grain structure, and interesting mechanical properties with yield strength comparable with that of 316L SS. The elongation of E-Fe was improved to 18% with annealing at 550˚C for 1 h. Heat treatment caused a decrease in the strength of E-Fe, with σ_y and σ_{UTS} reaching 270 and 292 MPa, which is still superior to the mechanical properties of annealed CTT-Fe and Mg alloys and close to those of Fe-35Mn alloy and 316L SS. E-Fe exhibited a higher corrosion rate than pure CTT-Fe and Fe-35%Mn alloy, but lower than Mg alloys. Figure 4.11 presents a semi-quantitative comparison of the cardiovascular stent materials based on their mechanical properties and degradation behaviour. It could be concluded that AE-Fe possesses interesting mechanical properties and corrosion rate and is a candidate for application as a biodegradable stent material. Moreover, using a cylindrical cathode, the electroforming technique could be used to produce Fe mesh tubes in a direct bottom- up method. This will provide a new way for direct electroforming of metallic stents in their final form. Further experiments are being

done to fabricate E-Fe mini-tubes and to study their microstructure, mechanical and degradation properties.

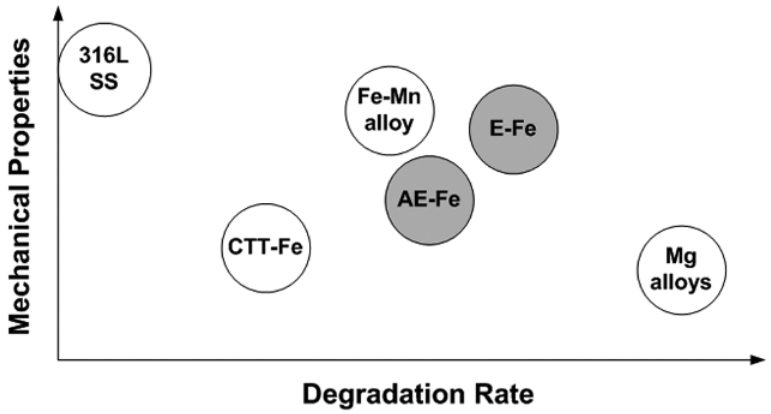

Figure 4.11- Comparison of different cardiovascular stent materials in terms of mechanical properties (yield strength and ductility) and degradation rate. 316L SS is not degradable and is presented in this figure as the reference stent material for comparison.

Chapter 5. Electroformed iron as a new biomaterial for degradable stents: In vitro degradation and preliminary cell viability studies

5.1 Résumé

Dans la recherche d'un matériau métallique avec une dégradation modérée et uniforme pour des applications comme stents dégradables, le fer électroformé a été évalué grâce à des tests de dégradation in vitro et de viabilité cellulaire. Les tests d'immersion statique et de dégradation dynamique ont été utilisés pour évaluer le taux de dégradation du matériau, et le test de viabilité cellulaire a été utilisé pour évaluer sa cytotoxicité. Les résultats ont été comparés à ceux du fer fabriqué par moulage et traitement thermomécanique précédemment étudié comme matériau pour les stents dégradables. Le fer électroformé a une dégradation plus rapide que le fer fabriqué par moulage (0,25 vs 0,14 mm an^{-1}) et son mécanisme de dégradation est uniforme. Les résultats de la viabilité cellulaire ont montré que l'activité métabolique de cellules musculaires lisses de rat n'a pas diminué après une exposition au fer électroformé. Toutefois, le fer électroformé a provoqué une diminution de la prolifération cellulaire qui pourrait être bénéfique pour l'inhibition de la resténose intra-stent.

5.2 Abstract

In the search for a metallic material showing moderate and uniform degradation for application as degradable cardiovascular stents, electroformed iron (E-Fe) was evaluated by in vitro degradation and cell viability tests. Static immersion and dynamic degradation were used to evaluate degradation rate and mechanism, while cell viability assay was used to assess cytotoxicity. The results were compared with those of iron fabricated by casting and thermomechanical treatment previously investigated as a stent material. Electroformed iron

showed faster degradation than iron fabricated by casting (0.25 vs. 0.14 mm $year^{-1}$), with a uniform degradation mechanism. Cell viability results showed that E-Fe did not result in a decrease in metabolic activity when exposed to primary rat smooth muscle cells. However, it caused a decrease in cell proliferation activity which could be beneficial for the inhibition of in-stent restenosis.

5.3 Introduction

Coronary stents have been developed to provide metal scaffolding for the angioplastied vessel in an attempt to limit negative remodelling of the arteries [130]. Stents have undergone enormous development since their first introduction in 1987, with 40 different types of stents commercially available today and more under development. This growing interest in stenting has been mainly due to their success in enlarging the vessel lumen, reducing restenosis rates, being able to cover dissections, and reducing early ischemic complications compared with angioplasty alone [131]. Despite the development and progression of bare metallic stents and their effectiveness in the prevention of recoil and late restenosis after coronary angioplasty, some concerns still remain because of their permanent nature [40,132]. Drug-eluting stents are designed to reduce restenosis rates of bare metal stents through localized release of *anti-proliferative* drugs such as sirolimus and paclitaxel. However, there is still a risk of late stent thrombosis associated with drug-eluting bare metal stents [56]. It is claimed that the role of stenting is temporary and is limited to intervention and a short period until healing and re-endothelialization are achieved. Beyond that, no advantage for stents has been demonstrated, and their presence could cause late thrombosis and chronic inflammation. Thus, the concept of biodegradable stents has emerged as an alternative to permanent stents [5]. Degradable stents are expected to provide the scaffolding effect to heal the diseased artery, then degrade and finally be eliminated from the body by physiological pathways. These stents could also be envisaged as a delivery vehicle for agents such as drugs and genes, and would perhaps have a role in the treatment of vulnerable plaque [40]. Metallic degradable stents made from iron-based and magnesium-based alloys are attractive mainly because they have the potential to perform similarly to 316 L stainless steel (316L SS) metal stents [56].

Theoretically, degradable materials for stents should have a controllable dissolution rate. An implant made of such a material should be able to function fully until the diseased vessel completely recovers. After that, the stent should be gradually dissolved, consumed or absorbed [44]. Uniform degradation is also desirable for the material to avoid localized attack which could result in implant failure, which is particularly catastrophic in the first weeks of implantation when the surrounding tissues have not completely healed [46]. The other important issue for degradable materials is their potential toxicity in body fluids in which released particles are supposed to circulate, or in tissue and organs in which they could accumulate. The toxicity of metallic materials is governed mainly by the toxicity of the component elements and the toxicity of the degradation products [48].

In the search for metallic degradable stent material, in vitro degradation tests followed by cytotoxicity tests and *in vivo* implantation have been performed to evaluate candidate materials. Generally, in vitro corrosion tests are used to approximate the degradation process that the material would undergo *in vivo* [46]. Electrochemical corrosion testing, including Potentiodynamic polarization [10,43-45,47,48], impedance spectroscopy [44,47,49] and immersion testing [43-46,48,49,59] are the conventional in vitro methods used to estimate the corrosion rate and mechanism of degradable metals for cardiovascular and orthopaedic applications. Although these methods are useful before *in vivo* implantation, it has been shown that the estimated corrosion rates of magnesium alloys AZ91D, LAE442 [43] and pure iron [5] were higher than those measured *in vivo*. The mismatch might be partially attributed to the dynamic nature of *in vivo* conditions due to blood flow compared with the static nature of conventional corrosion-testing methods [43]. Therefore, a new test bench was specifically designed by Lévesque et al. [46] which simulates dynamic conditions *in vivo*. This test bench was specially designed to test candidate materials for cardiovascular stent applications and reproduces the physiological conditions to which stents are submitted when implanted in coronary arteries. This dynamic degradation test has been already used to validate degradable AM60B-F and Fe-Mn alloy [43,45]. Hanks' [10,44-46,48], SBF (simulated body fluid) [47,49] and Ringer [5] solutions have been reported as degradation milieus in which the corrosion of alloys is investigated. These solutions simulate the ionic composition of blood plasma and usually contain Na^+, K^+, Mg^{2+}, Ca^{2+}, Cl^-, HCO_3^- and PO_4^{2-} ions with concentrations close to those in blood.

Degradation of magnesium alloys AE21 [37], WE43 [38] and pure iron [5,6] stents have been investigated under *in vivo* implantation, while in vitro degradation testing methods were used to evaluate iron-manganese alloy [9,10,45] and Mg alloys, including AM60B-F [46] and heat-treated WE43 [133]. *In vivo* implantation revealed high corrosion rates for AE21 [37]and WE43 [38] stents, leading to the loss of mechanical integrity in 3 months, while pure iron stents showed slower *in vivo* degradation than that estimated in vitro [5]. AM60B-F also showed a high corrosion rate with localized filiform corrosion which limits its application for stents. Finally, a moderate in vitro degradation rate was reported for iron–manganese alloy (Fe-35Mn) and heat-treated WE43. Among degradable materials investigated for stent applications, pure iron represents a very interesting candidate because of its relatively low degradation rate, mechanical properties comparable with those of 316L SS, and acceptable biocompatibility due to its biological role as an essential element for human body. The aim of this work was to evaluate the in vitro degradation properties of pure iron fabricated by electroforming. In a previous study [134], electroformed iron (E-Fe) showed superior mechanical properties to iron fabricated by casting and thermomechanical treatment (CTT-Fe) [134] which had been used for fabrication of degradable stents implanted *in vivo* [5,6]. Also E-Fe presents a fine microstructure with average grain size 4 μm, which is supposed to provide a higher degradation rate compared with CTT-Fe [134].

In the present study, static immersion and dynamic degradation tests were used to investigate the degradation behaviour of E-Fe, and the results were compared with the degradation rates of CTT-Fe and other degradable metals for stents. Results from static and dynamic degradation were also compared with those obtained previously from the potentiodynamic polarization test. A preliminary cytotoxicity assay was performed to investigate the cell response to E-Fe. The cell viability of CTT-Fe and 316 SS were also studied for comparison.

5.4 Materials and methods

5.4.1 Materials

Electroformed iron foils 80–100 μm thick were used for the degradation studies. The details of the electroforming process were presented in a previous study [134]. CTT-Fe foils 125 μm

thick (Fe > 99.9%, as-rolled, Goodfellow, USA) were used for comparison. These CTT-Fe foils were found to have the closest thickness to that of produced E-Fe among the available commercial pure Fe foils. Annealing at 550˚C was performed on E-Fe foils as well CTT-Fe foils to remove the stress produced by electroforming and rolling. As-electroformed Fe, annealed E-Fe and annealed CTT-Fe were examined in this study.

5.4.2 Microstructure

Microstructure evaluation before degradation was performed to investigate the microstructure-degradation behaviour relationship of the materials studied. Fe foils were cut, mounted in acrylic resin, polished with SiC 1000-4000 abrasive papers and 0.05μm alumina paste, and etched with 2% nital solution. Scanning electron microscopy (SEM; JSM-840A, JOEL) was used for microstructure observation of annealed E-Fe and CTT-Fe. The average grain size from SEM micrographs was identified using image analysis software by Clemex Technology Inc. The microstructure of as-polished E-Fe was observed by orientation imaging microscopy (OIM). OIM was performed using electron back-scattered diffraction (EBSD) to establish accurately the specific orientation of individual grains in polycrystalline electrodeposited iron foils. OIM maps were generated using a computer software program by TSL-EDAX from back-scattered electron Kikuchi patterns collected in a SUPRA 55 VP-Zeiss scanning electron microscope. The grain size identification was performed using the orientation images obtained.

5.4.3 Degradation solution

Degradation testing of iron in Hanks' solution, which simulates the ionic composition of blood plasma, was performed. The solution was prepared by dissolving Hanks' modified salt (H1387, Sigma Aldrich, USA) in deionized water with the addition of sodium bicarbonate (SX0320-1, Merck KGaA, Germany), Hepes sodium salt (sodium 4-(2-hydroxyethyl)-1-piperazineethanesulfonic acid, DB0265, Bio Basic, Canada) and Hepes acid (4-(2-hydroxyethyl)- 1-piperazineethanesulfonic acid, H3375, Sigma Aldrich, USA) as buffers to adjust the pH to 7.4. During degradation testing, the solution temperature was adjusted and maintained at 37 ± 1˚C. The composition of Hanks' solution was reported by Lévesque et al. [46].

5.4.4 Static degradation test

In this test, based on ASTM G31 standard [135], specimens (20×10×0.08 mm^3) were polished with 4000 grit SiC paper, cleaned with ethanol in an ultrasonic bath, dried and weighed. Three samples were tested from each material. They were then immersed in Hanks' solution for 336 h (14 days). The pH of the testing solution was measured every 48 h during the test. After the test, the specimens were removed, rinsed with water and ethanol and dried. The degradation layer of specimens was evaluated by SEM-EDS (energy dispersive spectrometry). The degradation layer was removed by peeling and then by dissolving in 10 M NaOH solution. The specimens were subsequently rinsed with deionized water and ethanol, dried and stored in a desiccator for 48 h before weighing. The degradation rate was calculated based on the weight loss of specimens according to [135]:

$$DR = {}^{4}\frac{W}{A.t.\rho} \qquad \textbf{Equation 5-1}$$

where DR is degradation rate in mm per year (mm/y), W is weight loss (g), A is area (cm^2), t is time of exposure (h), and ρ is density (g/cm^3).

5.4.5 Dynamic degradation test

Figure 5.1 shows a schematic of the dynamic test bench used in this work. The specimens, with surface area 20×10 mm^2, were mounted in acrylic resin and polished with 4000 grit SiC paper, rinsed with deionized water and ethanol and dried. They were then installed in a specimen holder and exposed to circulation of the testing solution (Hanks' solution) for 336 h. The pH was measured at 48-h intervals; 5 ml of the testing solution was taken out and replaced with fresh Hanks' solution. The solution samples were analysed by atomic absorption spectroscopy (AAS; Model 3110, Perkin Elmer) for the measurement of Fe^{2+} ions. This analysis was used to compare the ion release behaviour of different iron specimens (electroformed and CTT) vs. time. After the test, samples were dried and SEM-EDS and X-ray diffraction (XRD; Siemens D5000) analysis were performed on the surface degradation layer. The degradation layer was then removed using the same method as in the static degradation tests. Specimens were mounted in acrylic resin, polished with 1000-4000 SiC abrasive paper and 0.05 μm alumina paste, and etched with 2% nital solution. An

Olympus PME3 optical microscope was used to study cross-sections of the corroded specimens to analyse and compare the degradation rates.

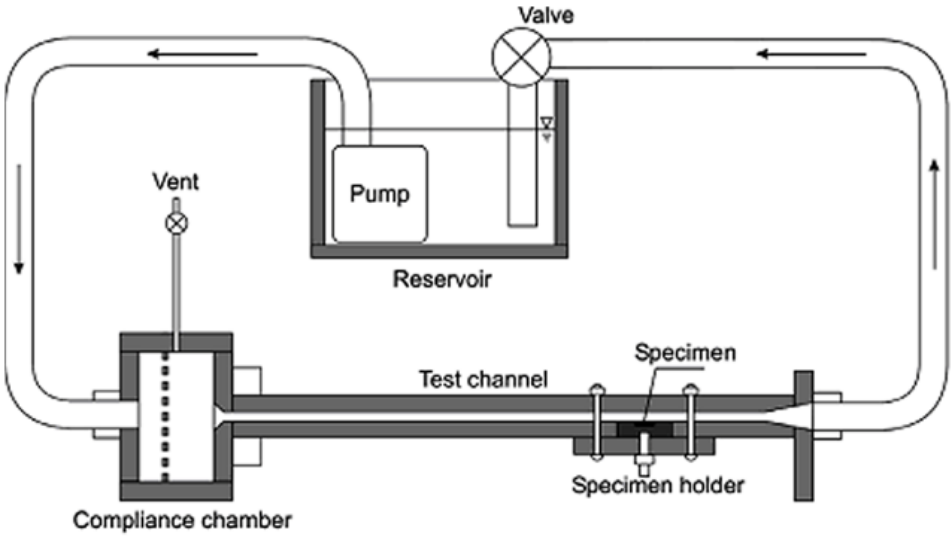

Figure 5.1- Schematic view of the dynamic test bench.

5.4.6 Cell viability test

Although the biocompatibility of iron has been shown *in vivo* [5,6] and in vitro [136], a cell viability test was performed in this study to investigate the effect of E-Fe on the viability and proliferation of smooth muscle cells (SMC). The authors believed that a cell viability essay of E-Fe was necessary for material screening because it was produced from an electrochemical method which could potentially induce contamination to the material. The cell viability tests were adapted from a method used in Refs. [48,137] with some modifications. Specimens of 316L SS, E-Fe, annealed E-Fe and CTT-Fe were polished with 4000 grit SiC abrasive paper, cut into 2×2 mm^2 pieces and ultrasonically cleaned in acetone, water and ethanol, respectively. 316L SS was used as reference for the cell viability test, as it is the gold standard material for metallic stents. Prior to treatment, specimens were sonicated in 75% ethanol, rinsed with PBS solution, and air dried in a laminar hood. The tests were carried out by indirect contact with the primary rat vascular SMC. They were cultured in SmBM (Lonza, Switzerland) with 10% fetal bovine serum, 100 U ml^{-1} penicillin and 100

mg ml^{-1} streptomycin at 37˚C in a humidified atmosphere of 5% CO_2. The number of passage was maintained at less than five. The cells were incubated in 24-well tissue culture plates at 30,000 cells $well^{-1}$ for 24 h to allow cell attachment. Medium containing the disc specimens was then added to the wells, with 3 μm tissue culture inserts placed above the cells. At least six replicates for each material, including E-Fe, annealed E-Fe, CTT-Fe and 316L SS, were assessed to obtain averages and standard deviations. Since both metabolic activity and cell proliferation assays were performed for 24, 48 and 72 h, a total of 36 specimens were used from each material. After 24, 48 and 72 h incubation, the cell metabolic activity was assessed using water-soluble tetrazolium-based assay (10% WST-1) for 1 h. The absorbance of WST-1 of the solutions was measured spectrophotometrically at 440 nm by VersaMax microplate reader (Molecular Devices, Sunnyvale, USA). The cell proliferation was also measured by cell counting method using a hemacytometer with the addition of trypan blue. The statistical analysis of cell metabolic activity and cell proliferation was carried out using the Prism 5 software (GraphPad Software Inc., San Diego, CA).

5.5 Results and discussion

5.5.1 Microstructure

The microstructures of the polished surfaces of E-Fe, E-Fe annealed at 550˚C, and CTT iron annealed at 550˚C are shown in Figure 5.2. The grains of E-Fe could not be revealed by SEM and, therefore, OIM characterization was carried out to indicate the microstructure. OIM of E-Fe indicated fine grains with a highly oriented texture. The blue colour in the orientation map is related to the <111> direction, suggesting that the majority of grains are oriented in this direction. The average grain size was 4 μm. Since the grain boundaries of annealed E-Fe could be observed by SEM, the recrystallization of E-Fe by annealing could be speculated. The average grain size was 6 μm for annealed E-Fe, while CTT-Fe had an average grain size of 25 μm. The finer grain size observed for E-Fe is related to the electrodeposition process, which is a technique for the fabrication of fine-grain metals [113].

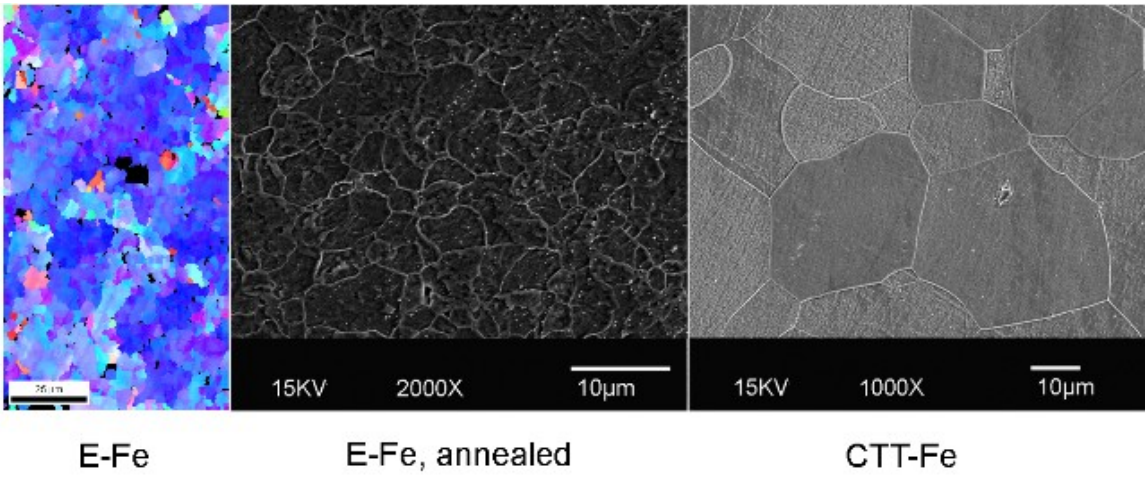

Figure 5.2- Microstructure of as-deposited E-Fe, E-Fe annealed at 550˚C and CTT-Fe; the average grain size of CTT-Fe is much larger than that of E-Fe and annealed E-Fe.

5.5.2 Degradation testing

5.5.2.1 Static degradation test

Degradation started immediately after immersing E-Fe and annealed E-Fe in Hanks' solution, as the surface of the specimens was rapidly covered by bubbles of reducing hydrogen from the electrolyte. After 24 h, the surfaces were completely covered by brownish degradation products. For CTT-Fe, the degradation attack was slower, and the surface was completely covered after 7 days of immersion. The pH value of electroformed specimens reached 7.7 from 7.4 during the first 48 h and then stabilized. The initial increase in pH could probably be related to the rapid corrosion of the metal, which resulted in hydrogen evolution. For CTT-Fe, pH reached 7.6 and stabilized thereafter. Figure 5.3 shows the morphology of degradation products of the surface of E-Fe. The cracks are probably caused by dehydration of the degradation layer after removal from the electrolyte during air-drying. EDS analysis detected iron, oxygen, phosphorus, chlorine and calcium in the degradation layer. The brownish degradation layer was removed easily by peeling, but a second, dark greyish, layer was detected on the surface, which was removed by chemical dissolution. This layer was composed mainly of iron and oxygen.

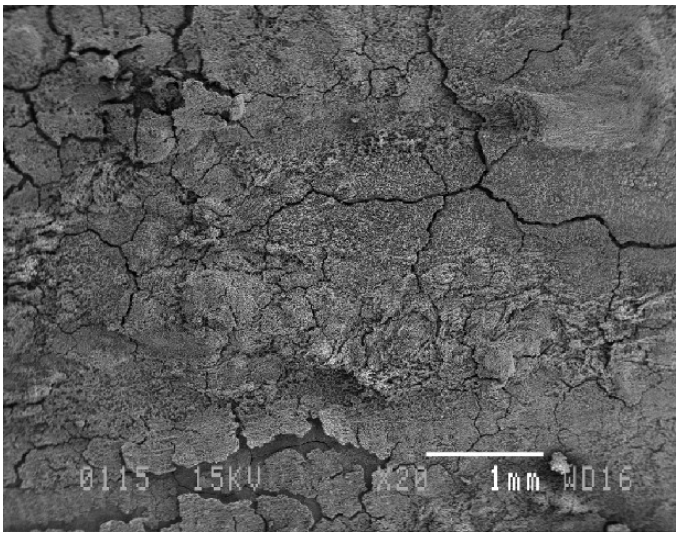

Figure 5.3- Degradation layer on E-Fe after static test: the cracks are caused by dehydration of the degradation layer.

The surface morphology of the E-Fe and annealed E-Fe after the degradation products were removed is presented in Figure 5.4. The degradation of E-Fe and annealed E-Fe appears to be uniform, as no localized attack could be found on the surface. However, it can be seen that as-electroformed Fe is more degraded than annealed E-Fe, since deeper corrosion can be seen in Figure 5.4 (a).

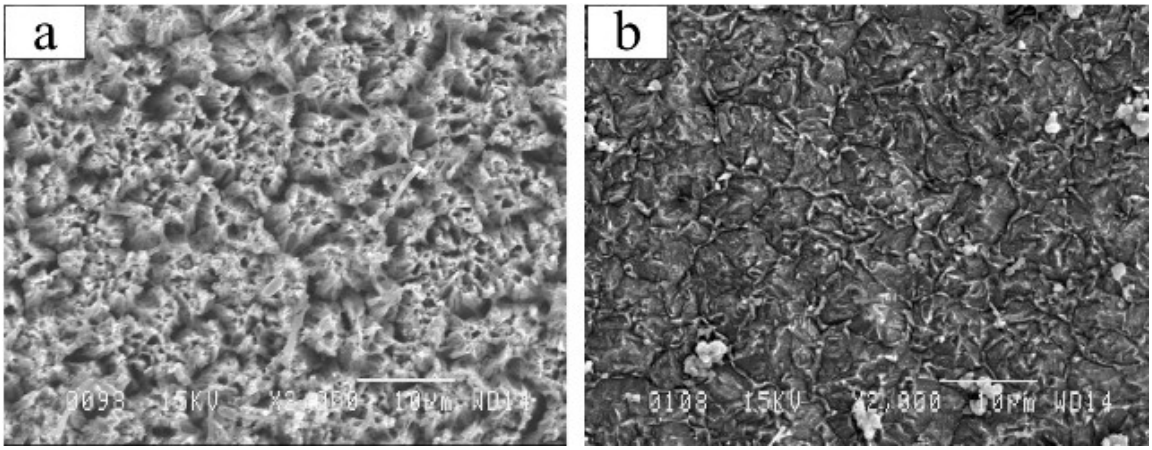

Figure 5.4-Degraded surface of (a) E-Fe and (b) annealed E-Fe: neither image shows signs of localized attack. Deeper corrosion could be seen for E-Fe than for annealed E-Fe.

The degradation rates of Fe calculated by static test, and those of other degradable alloys obtained from literature, are presented in Table 5.1. The degradation rate of as-electroformed Fe (0.4 mm $year^{-1}$) was almost three times higher than that of CTT-Fe (0.14 mm $year^{-1}$). This might be attributed to the fine-grain structure and structural defects of E-Fe resulting from electrodeposition, which provides a surface potentially prone to corrosive attack. This is confirmed by observation of electroformed Fe samples, which were covered by corrosion products much faster than CTT-Fe samples. After annealing, the degradation rate of electroformed Fe decreased to 0.25 mm $year^{-1}$, due to the decrease in the density of defects, stress relief and partial grain growth occurring in annealing. The degradation rate of annealed E-Fe is comparable with that of Fe–35Mn alloy (0.25 vs. 0.26 mm $year^{-1}$) and is much slower than degradation of AM60B-F alloy (2.78 mm $year^{-1}$). It has a moderate degradation rate among degradable metals which could make it a good candidate for degradable stents. Comparison of potentiodynamic polarization [134] and static degradation methods shows that, although both methods showed a higher corrosion rate for as-electroformed Fe than for CTT-Fe, different corrosion rate values were obtained from these methods. While the corrosion rate for E-Fe was 0.85 mm $year^{-1}$ by the potentiodynamic test [134], a degradation rate of 0.40 mm $year^{-1}$ was calculated from the static immersion test. This significant difference could be attributed to the effect of the testing conditions. Potentiodynamic polarization is a short-term corrosion-testing method in which time-dependent degradation phenomena cannot be clearly observed. During this test, no precipitation (from Hanks' solution) or observable degradation products were formed on the iron surface. The sample surfaces were always exposed to the solution during the electrochemical measurement [134]. In contrast, in the static test the testing duration from which the degradation rate was calculated was 336 h. As mentioned above, the surface of E-Fe was completely covered by precipitation from the testing solutions and by the brownish hydroxide degradation layer. This layer resulted in the lowering of the degradation rate, because the metal surface was not in direct contact with the corrosive milieu, and degradation had to occur by diffusion of Fe^{2+} through the layer. This is in agreement with the precipitation layer observed by Lévesque et al. [46] for Mg alloy, in which further degradation continued by the diffusion of Mg ions through the layer. For CTT-Fe, this significant difference in degradation rate was not observed, since the degradation layer

(in static test) was completed in 168 h, before which the fresh metallic surface was in contact with the corrosive solution.

Table 5.1- Degradation rate values calculated from static test for E-Fe, annealed E-Fe and CTT-Fe; degradation rates of Fe-Mn alloy and AM60B-F alloys were extracted from the literature for comparison; for all materials, the degradation rate was calculated based on the weight loss during the test.

Material	As-electroformed Fe	E-Fe annealed	CTT-Fe annealed	Fe-35Mn alloy [9,45]	AM60B-F Mg alloy [45]
DR(mm/y)	0.40 ± 0.03	0.25 ± 0.02	0.14 ± 0.02	0.26	2.78

5.5.2.2 Dynamic degradation

The Fe ion release behaviour of E-Fe, annealed E-Fe and CTT-Fe are presented in Figure 5.5. The amount of Fe ion in the solution samples from E-Fe increased rapidly during the 144 h of dynamic testing, after which the ion release rate (IRR) was lower. This is also related to the formation of degradation products in the dynamic test, similar to what happened for static testing. However, in the dynamic test, the formation of the thick degradation layer occurred after a longer period compared with the static test, because the dynamic solution flow could partially ‘‘wash” the degradation products, providing a ‘‘fresh” metallic surface for degradation. Figure 5.5 shows that Fe^{2+} ion release of E-Fe was higher than that of CTT-Fe, which is consistent with the results for the degradation rate from static and potentiodynamic polarization tests [134]. Electroformed Fe was more prone to degradation because of the fine grains and microstructural defects, which resulted in the release of a higher quantity of Fe^{2+} measured by AAS. The pH of all three Fe specimens reached 7.6 after 48 h and stabilized thereafter. This change in pH was slightly lower than in the static test because of the solution flow in the dynamic bench, which limited the local increase in pH.

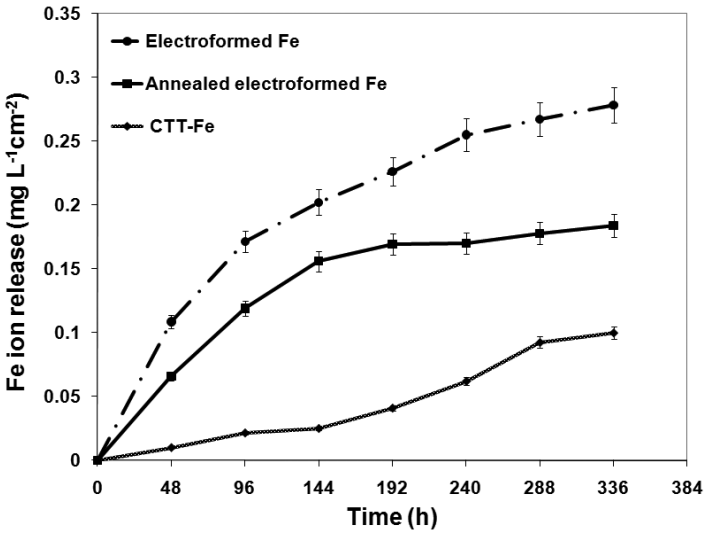

Figure 5.5- Fe ion release behaviour of electroformed and CTT iron: E-Fe released ahigher quantity of Fe ion than CTT-Fe did during the testing period. After annealing, the ion release of E-Fe decreased. However, it was still higher than that of CTT-Fe.

In order to investigate the kinetics of ion release, the IRR of iron was calculated from the curves in Figure 5.5 by plotting ion release (mg L^{-1} cm^{-2}) vs. square root of time ($h^{1/2}$). Figure 5.6 shows the lines obtained, their calculated correlation coefficient (R) and the calculated IRR. Acceptable R values (>0.95) were obtained for E-Fe (0.9954) and annealed E-Fe (0.9760), suggesting that Fe^{2+} release behaviour was parabolic for these materials. However, the ion release of CTT-Fe was not linear, which might be due to the slower growth of degradation on its surface. Based on the lines obtained, the IRR for E-Fe can be expressed as 0.016x, where x is $t^{1/2}$, while it would be 0.011x for annealed E-Fe. This calculation is important to assess the toxicity of E-Fe stent in terms of daily permitted intake level of iron in the human body.

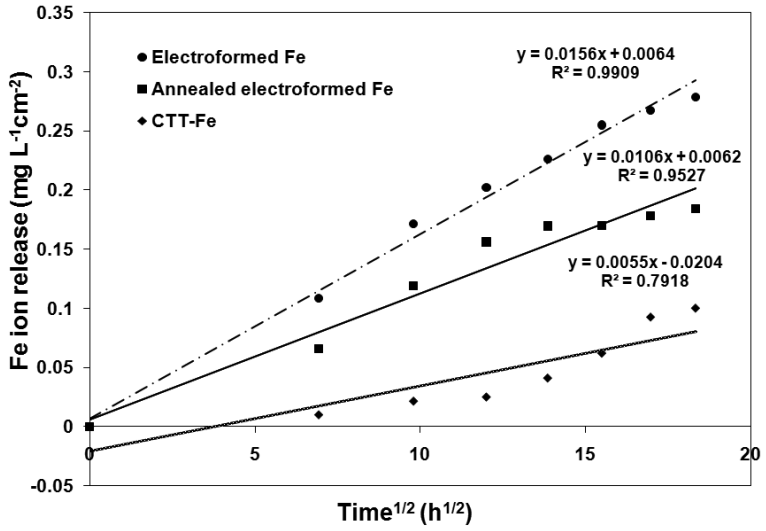

Figure 5.6- IRR of iron calculated from curves in Figure 5.5: the IRR of the studied material was calculated from the lines.

The daily permitted intake of iron is 6–40 mg, while its blood level is 447 mg L^{-1} [138]. Based on the present results, an electroformed Fe implant with a surface area of 1 cm^2 would theoretically release 0.418 mg L^{-1} of iron into the blood in 30 days. Therefore, the average daily release of iron would be 0.014 mg L^{-1}, which is far below the iron level of 447 mg L^{-1} in blood. The average daily release for an annealed electroformed Fe would be 0.01 mg L^{-1} based on the same estimation method. Hence, both as-electroformed and annealed electroformed Fe are assumed to be safe for implantation in terms of Fe^{2+} intake level in the human body. In comparison with Fe–35Mn and AM60B-F alloys, which had been studied using the same degradation method, the IRR of annealed E-Fe was very close that of Fe–35Mn ($0.01t^{1/2}$) [45], while the IRR of as-electroformed Fe was slightly higher. CTT-Fe showed the lowest rate ($0.005t^{1/2}$), which confirmed its slow degradation reported by Peuster et al. [5]. Iron-based metals showed much slower degradation compared with AM60B-F (the IRR of Mg^{2+} was $1.173t^{1/2}$) [46], which makes them more interesting candidates for stent application.

Morphology of the degradation layer on iron samples after dynamic degradation is shown in Figure 5.7. The morphology is very similar to that of the degradation layer from the static immersion test, with cracks caused by dehydration of the layer. EDS analysis revealed the

presence of iron, oxygen, phosphorus and calcium in the degradation layer. This is the same elemental composition found on static test sample surfaces. XRD characterization of the degradation layer is presented in Figure 5.8. A mixture of crystalline and amorphous phases was detected in the layer, where the crystalline phases were goethite (FeO(OH)) and magnetite ($FeO.Fe_2O_3$). Although calcium and phosphorus were found on the surface of corroded iron specimens by EDS, the formation of hydroxyapatite ($Ca_{10}(PO_4)_6(OH)_2$), which had been reported for AZ31 Mg alloys immersed in SBF solution [49], could not be confirmed by the XRD results.

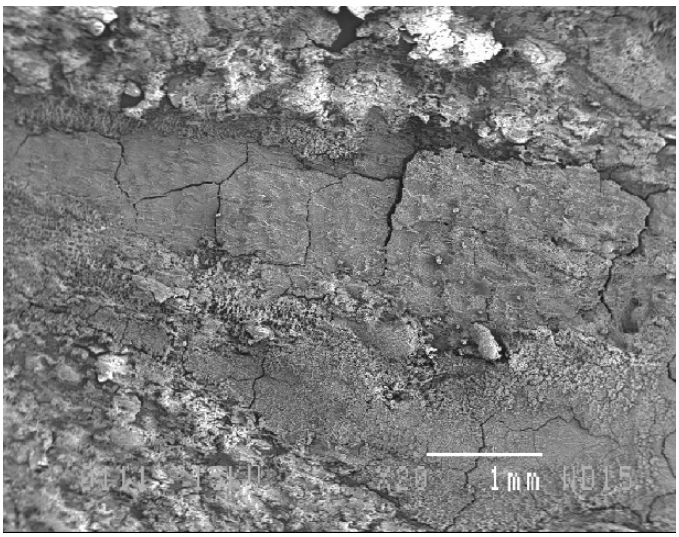

Figure 5.7- Degradation layer on the surface of samples after the dynamic test: the layer is cracked because of dehydration after the test. The morphology is similar to that of the static test.

Based on the corrosion products detected by EDS and XRD on the surface of corroded electroformed Fe, the degradation mechanism is suggested as follows.

When iron is immersed in the solution or exposed to the solution flow, it is oxidized to Fe^{2+} ions based on the following reactions:

anodic reaction: $Fe \rightarrow Fe^{+2} + 2e^-$ (1)

cathodic reaction: $\frac{1}{2} O_2 + H_2O + 2e^- \rightarrow 2\ OH^-$ (2)

ferrous hydroxide formation: $Fe^{+2} + 2\ OH^- \rightarrow Fe(OH)_2$ (3)

Some of the Fe^{2+} ions produced could be transformed to Fe^{3+} ions under the condition of alkaline pH and the oxygen environment of Hanks' solution [139], and ferric hydroxide is produced:

$Fe^{+2} \rightarrow Fe^{+3} + e^{-}$

$Fe^{+3} + 3OH^{-} \rightarrow Fe(OH)_3$

As the solution is aerated and in the presence of chloride ions, ferric hydroxide is hydrolysed and goethite (α -FeO(OH)) precipitates [140]. Ferrous hydroxide will then react with a part of FeO(OH) and magnetite is formed [141]:

$Fe(OH)_2 + 2FeO(OH) \rightarrow Fe_3O_4 + H_2O$

Precipitation of calcium and phosphorus from the solution along with the hydroxide and oxide formed on the surface of Fe was responsible for the decrease in the IRR after the first few days of dynamic testing. The presence of a degradation layer on the iron surface would not be a concern in case of *in vivo* implantation, because it has been shown in the case of iron stent implantation that Fe degradation products were cleared by macrophages, and no toxic effect was observed due to the local accumulation of degradation products [5,136].

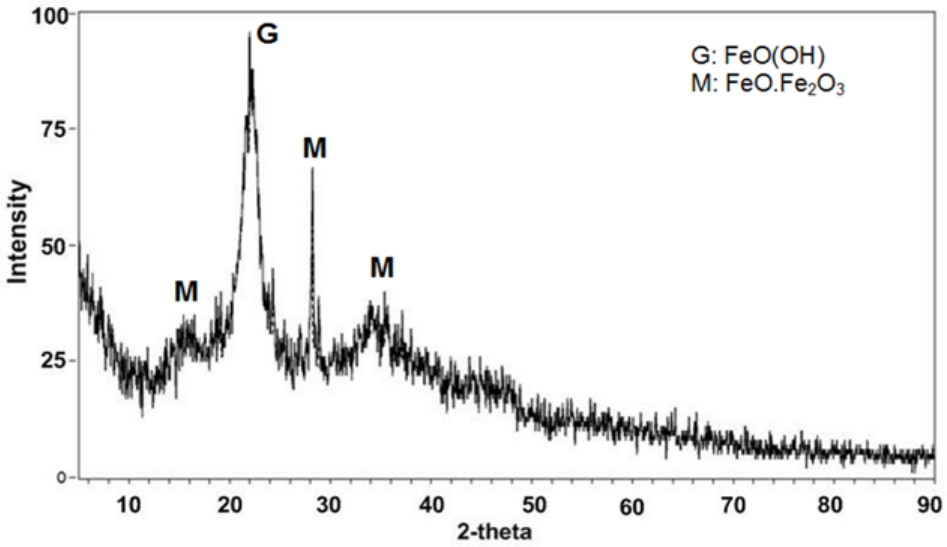

Figure 5.8- XRD pattern of degradation layer from dynamic test: goethite (JCPDS No. 29-0713) and magnetite (JCPDS No. 19-0629) were detected in degradation layer.

The cross-section of E-Fe and annealed E-Fe before and after the dynamic degradation test are shown in Figure 5.9. Columnar grains which are the typical grain structure for electrodeposited metals [66] can be observed for E-Fe (Figure 5.9(a)), while in annealed E-Fe (Figure 5.9(c)) the grain structure has changed and includes large columnar grains as well as equiaxed grains. The thickness of E-Fe was ~ 90 μm, which reduced to 65 μm after dynamic degradation (Figure 5.9(b)). The degradation was uniform, as shown in Figure 5.9(b), with no signs of localized attack. The degradation of annealed E-Fe was lower than that of E-Fe, as shown in Figure 5.9(d). For annealed E-Fe, the degradation is also uniform, although the morphology of the degraded surface is different from as-electroformed Fe. The average thickness of annealed E-Fe after dynamic degradation was 76 μm. Figure 5.9(e) and (f) shows global pictures at lower magnification of as-polished electroformed and annealed E-Fe in which uniform degradation could be observed. The dynamic degradation rate of E-Fe and annealed E-Fe was calculated based on the decrease in their thickness during the dynamic test. The estimated degradation rate for E-Fe and annealed E-Fe was 0.65 and 0.37 mm $year^{-1}$, respectively.

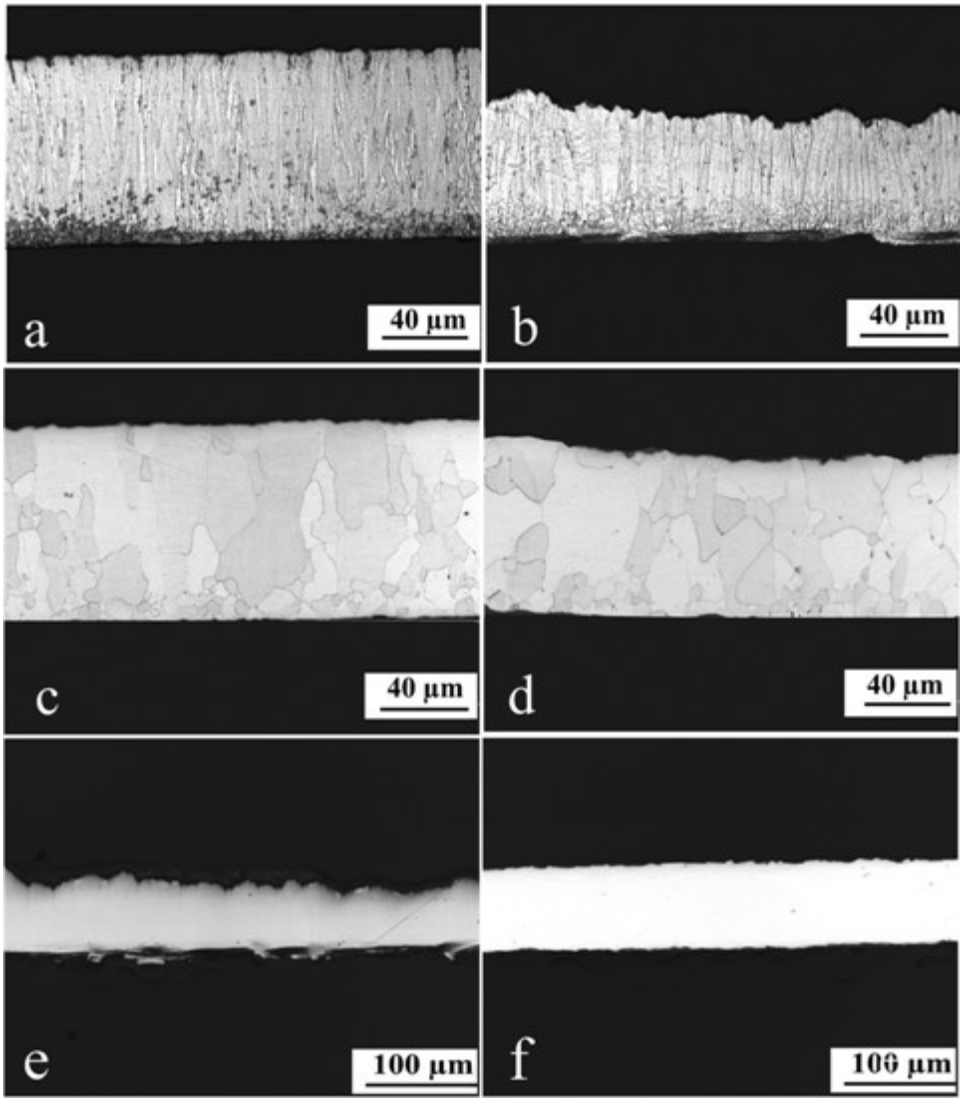

Figure 5.9- Cross-section of as-electroformed Fe (a) before and (b) after dynamic test; annealed E-Fe (c) before and (d) after dynamic test; (e) as-electroformed Fe and (f) annealed E-F after degradation. (a–d) shows the etched cross-sections at 200X, while (e and f) are from as-polished samples at 50X.

These values are different from the degradation rates calculated by Potentiodynamic polarization and static immersion tests, mainly because of the different conditions applied in these three methods. In the dynamic degradation test, although the formation of the degradation layer occurred later than in the static test, this layer lowered the release rate of Fe^{2+} ions (as shown in Figure 5.5) and thereby lowered the degradation rate. Therefore, the calculated degradation rate is lower than the corrosion rate calculated in the

Potentiodynamic polarization test, in which the testing time was 1 h. Still, the degradation rate of the dynamic test is higher than that of the static test because of the solution flow, which resulted in the formation of the degradation layer in a longer period. Although different degradation rate values were obtained from the three degradation testing methods applied in this study, all the methods showed a higher degradation rate for E-Fe compared with CTT-Fe. Fine-grain structure, internal stress and structural defects of E-Fe produced by electrodeposition [66] could be the main cause of this behaviour. Also, the degradation rate of annealed E-Fe was found to be lower than that of as-electroformed Fe according to all three methods, owing to the effect of stress relief, decrease in defect density and partial grain growth occurring in annealing.

5.5.3 Cell viability

Relative cell metabolic activity and total cell counting as a function of incubation time are presented in Figure 5.10. Results showed that both CTT-Fe and electroformed Fe discs had no significant inhibition effect on the cell metabolic activity at 24, 48 and 72 h incubation time, showing a similar effect to 316L SS, which has no inhibition of cell metabolic activity due to its inert behaviour. The cell counting measurement (Figure 5.10, right axis) shows different cell numbers for the materials studied, which correspond to proliferation rate of the rat SMC. The cells incubated with E-Fe showed a slight decrease in cell number at 24 h of incubation compared with other materials. The decrease could be related to the rapid corrosion of E-Fe, which releases $Fe2^{+}$ ions into the culture medium. At 48 h of incubation, a more significant decrease in cell proliferation is observed for all three iron materials caused by the increased release of Fe^{2+} ions. The decrease in cell proliferation continued for iron materials at 72 h and was more noticeable for E-Fe owing to its high degradation rate (0.4 mm $year^{-1}$ for E-Fe vs. 0.14 mm $year^{-1}$ for CTT-Fe based on static degradation test results). The decrease in proliferation of human SMC caused by Fe^{2+} ions has already been reported by Mueller et al. [136]. They investigated the interaction of individual corrosion products from biodegradable iron stents with cells from the adjacent tissue using a cell culture model at the phenotypic and molecular levels. They found that, when soluble ferrous ions were added to the cell culture medium, the cell growth rate was reduced,

suggesting that specific iron stent degradation products could have a beneficial effect in the control of neointimal proliferation. Based on the present results, one may therefore conclude that the decrease in SMC cell number could make electroformed Fe beneficial for application as a cardiovascular stent material, since it could inhibit cell proliferation after stent implantation. 316L SS did not cause any significant difference for cell counting assay at all incubation periods, suggesting that this material is relatively inert compared with iron.

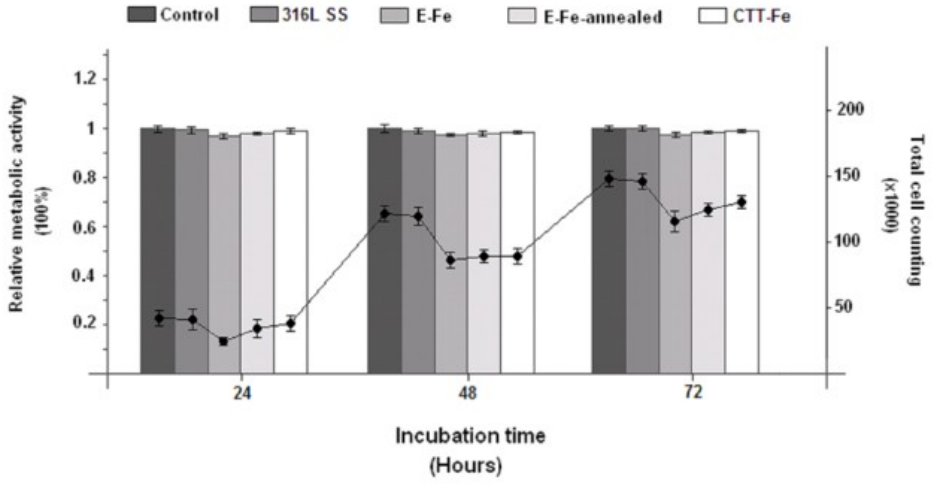

Figure 5.10- Cell viability of iron and 316L SS: the column charts are related to the relative cell metabolic activities as a function of incubation time at 24, 48 and 72 h (left axis), while the curve is the total cell count measured at 24, 48, and 72 h (right axis).

Although cell proliferation was inhibited by iron material, cell metabolic activity did not change, suggesting that there was an increase in the metabolic activity of the remaining cells. This increase could be speculated to be as a consequence of Fe^{2+} release in the culture medium, which requires cells to regulate the excess of ferrous iron. This regulation of excess ferrous ions is needed, as the free extracellular ferrous ions could participate in the Fenton reaction. This reaction is known to have adverse effects on the cells, since it could generate hydroxyl radicals which induce lipid peroxidation, DNA damage and altered calcium homeostasis [142,143]. Thus, to prevent this adverse reaction, the ferrous ions preferably bind to transferrin, a regulatory protein that transports excess ferrous ions. To meet this need, more metabolic activity is needed in order to fulfil the adenosine

triphosphate (ATP) demand of the cells to produce transferrin and the iron storage protein called ferritrin, as well as mobilizing the ferrous ions within the cell.

5.6 Conclusions

Static immersion and dynamic degradation methods showed uniform degradation with a moderate rate for electroformed Fe. The methods applied also confirmed that E-Fe had faster degradation than CTT-Fe. This suggests that E-Fe is an interesting alternative to CTT-Fe. The in vitro degradation tests were useful for investigating the degradation behaviour of the materials studied in order to select a suitable candidate before proceeding to *in vivo* studies. Preliminary cell viability results showed no inhibition of primary rat SMC metabolic activity by E-Fe and also suggested that this material could be beneficial in the inhibition of cell proliferation if implanted as a cardiovascular stent. However, biological response to E-Fe during and after degradation needs to be carefully assessed.

Chapter 6. Effect of electrodeposition current density on the microstructure and the degradation of electroformed iron for degradable stents

6.1 Résumé

Le fer pur est devenu l'un des matériaux les plus intéressants pour les stents métalliques dégradables en raison de ses propriétés mécaniques élevées et de sa dégradation modérée. Dans ce travail, nous avons étudié l'effet de la densité de courant d'électrodéposition sur la microstructure et la dégradation des films de fer pur produits par dépôt électrolytique sur un substrat en alliage Ti pour application comme stents dégradables. Les feuilles de fer ont été produites par électrodéposition en utilisant quatre différentes densités de courant (1, 2, 5 et 10 $A.dm^{-2}$). Les films ont ensuite été étudiés par le microscope électronique à balayage (MEB) et diffraction d'électrons rétrodiffusés (EBSD) afin d'observer la morphologie de la surface, la taille et l'orientation des grains. Les tests de corrosion par polarisation potentiodynamique et l'immersion statique ont été utilisés pour déterminer le taux de corrosion et étudier le comportement de dégradation des films de fer. La densité de courant a un effet significatif sur la texture, la taille et la forme des grains du fer électrodéposé. À des densités de courant de 1, 5 et 10 $A.dm^{-2}$, des textures faibles correspondant aux directions <1 0 1>, <1 1 1> et <1 1 2> dans la direction normale ont respectivement été obtenues. À ces densités de courant, une taille moyenne inférieure à 3 μm a également été obtenue. Cependant, à 2 $A.dm^{-2}$, une forte texture de direction <1 1 1> parallèle à la direction normale avec une densité de 7,4 (mean uniform distribution) a été obtenue avec des grains de taille moyenne de 4,4 μm. La microstructure des échantillons de fer a changé après un recuit à 550 °C à cause de la recristallisation induite. Différents taux de corrosion ont été obtenus à partir des courbes de polarisation potentiodynamique des films de fer déposés à différentes densités de courant. Le Fe-2 a montré le plus faible taux de corrosion en raison de ses grains plus grands et sa texture. Les taux de corrosion de tous les échantillons de fer ont diminué après le recuit. La dégradation statique a montré des taux de

corrosion inférieurs à ceux obtenus pas polarisation potentiodynamique en raison de la formation d'une couche de dégradation sur la surface des échantillons qui réduit le taux de dégradation. La morphologie de dégradation est uniforme pour le Fe-2 en raison de sa forte texture. D'autre part, des piqûres microscopiques ont été trouvées pour le Fe-1, Fe et Fe-5-10.

6.2 Abstract

Pure iron has become one of the most interesting candidate materials for degradable metallic stents due to its high mechanical properties and moderate degradation. In this work we studied the effect of electrodeposition current density on microstructure and degradation of pure iron films electrodeposited on Ti alloy substrate for degradable metallic stent application. Iron sheets were produced by electrodeposition using four different current densities 1, 2, 5 and 10 $A.dm^{-2}$. The films were then studied by SEM (scanning electron microscope) and EBSD (electron backscatter diffraction) to observe the surface morphology, grain size and orientation. Potentiodynamic polarization and static immersion tests were used to determine the corrosion rate and to study the degradation behaviour of iron films, respectively. The Current density was found to significantly influence the texture, the grain size and the grain shape of the electrodeposited iron. At current densities of 1, 5 and 10 $A.dm^{-2}$, weak textures corresponding to <1 0 1>, <1 1 1> and <1 1 2> in the normal (electrodeposition) direction were obtained, respectively. At these current densities, an average grain sizes smaller than 3 μm were also obtained. However, at 2 $A.dm^{-2}$, a strong <1 1 1>//ND texture with density of 7.4 MUD was obtained with larger average grain size of 4.4 μm. The microstructure of iron samples changed after annealing at 550˚C because of the induced recrystallization. Different corrosion rates were obtained from potentiodynamic polarization curves of iron films deposited at different current densities because of their microstructures. Fe-2 showed the lowest corrosion rate due to its larger grains size and its texture. The corrosion rates of all iron samples decreased after annealing. Static degradation showed lower corrosion rates for iron because of the formation of a degradation layer on samples surface which reduced the degradation reaction rate. The degradation morphology was uniform for Fe-2 due to its strong texture. On the other hand, microscopic pits were found for Fe-1, Fe-5 and Fe-10.

6.3 Introduction

Coronary stents are mesh-like tubular scaffolds which are inserted on angioplasty balloon and expanded in blocked coronary arteries to keep them open [4]. Current stent technology is based on the use of permanent stents made from corrosion resistance materials such as 316L stainless steel. However, it has been shown that the role of stenting is temporary and limited to several months after implantation during which the artery is remodelled. After this period, the presence of stent in the artery could not provide any beneficial effects [23]. In this context, degradable metallic stents have been developed and evaluated during the last decade. These stents provide the required scaffolding to the artery and degrade gradually by physiological ways [5,31]. Although corrosion is generally considered as a failure in metallurgy, for specific applications it might be useful, such as degradable stents. The stent is expected to degrade and corrode when implanted into the physiological site, and surrounded by physiological media, blood, and the surrounding cells and tissue. The corrosion products are expected to be removed by the body physiological pathways. Therefore, the candidate metals for this application should not induce toxic effects to the cells, tissues and the overall body [5,22]. Magnesium and iron-based alloys are two candidates suitable for degradable stents. These are both essential elements for the body with higher daily intake levels compared to other metals [5,37]. Uniform and moderate (around 12 months) degradation is also a requirement for degradable stents because localized corrosion could result in mechanical failure of the metallic implant and very fast corrosion (less than 6 months) may results in total dissolution of the implant in a short period of time, and therefore leads to clinical complications. [22].

We previously reported the fabrication and evaluation of electroformed pure iron aimed to degradable stents [134,144]. Electrodeposition is a technique generally used to produce coatings which improve the surface conditions of the substrate metal [66]. However, we have shown that this technique can be used for production of iron films with targeted mechanical and degradation properties for a structural application as degradable stent. Metals with fine grain size, different microstructures and textures, different forms and thicknesses can be produced by electrodeposition [13,75]. The microstructure and texture of electrodeposited metals is strongly affected by the deposition conditions and is particularly sensitive to parameters including current density, electrolyte composition, temperature, pH and

substrate [64,75]. The corrosion resistance of electrodeposits depends in particular on their chemical composition and also on their crystallographic orientation [145,146]. It has been shown that when a metal is exposed to a corrosive environment, the corrosion resistance of each grain varies because of the difference in the binding energy of atoms between the crystallographic planes [147]. Therefore, crystallographic orientation (texture) plays an important role on the corrosion rate and form of metals and it is essential to investigate the relation between texture and corrosion for degradable stent materials. In the case of electroformed iron, a strong (1 1 1) texture with grain size of 4 μm was obtained at current density of 2 Adm^{-2}. This texture showed a uniform corrosion faster than that of Armco ® iron with 25 μm grains [134,144]. However, the corrosion behavior of electroformed iron with other textures has not yet been studied. In this work, we report the effect of electrodeposition current density on microstructure, crystallographic orientation and thereby corrosion rate and form of iron. This information is mandatory in order to produce iron stents with targeted microstructure and targeted degradation.

6.4 Materials and Methods

The details on electrodeposition set-up and parameters including electrolyte, additives, temperature, pH, cathode and anode were presented elsewhere [134]. Different current densities of 1, 2, 5 and 10 Adm^{-2} were applied for 8, 4, 2 and 1h respectively to obtain ~100-μm thick foils with different microstructures. Based on the electrodeposition current density, iron samples will be named as Fe-1, Fe-2, Fe-5 and Fe-10 thereafter. Foil-shaped samples were used in this study mainly for the feasibility of further characterizations that require planar specimens. However, mini-cylindrical samples (diameter of 2-4 mm) can also be produced by this technique. The foils were removed mechanically from the substrate after the electrodeposition process. They were annealed at 550˚C for 1 h in high purity argon atmosphere. Annealing of as-laser-cut stents is an important step in stent fabrication in order to remove the stress from laser cutting and to induce recrystallization in as-drawn stent tube which is initially in cold-worked state. For 316L SS stents, the annealing is usually performed in a vacuum furnace at 1100-1200˚C to produce a recrystallized and fine microstructure [8,148]. In case of electroformed iron, we have shown that annealing at 550˚C produces a recrystallized structure and highly increases the ductility

[134]. Therefore, the microstructural observation and degradation testing were performed on electroformed iron on both as-deposited and annealed state.

The surface morphology of as-electroformed films was studies using Scanning Electron Microscope (SEM; JOEL JSM-840A). To investigate the texture of deposits, Orientation Imaging Microscopy (OIM) was performed using Backscatter Electron Microscope. For EBSD investigation, the cathodic surface of the specimens (electrodeposit-substrate interface) were mechanically ground with 1000 grit SiC paper using water as lubricant, and then successively polished with 15, 9, 3 and 1 μm diamond pastes a few minutes each. The final step was a surface polishing with an alkaline colloidal silica solution (0.04 μm granulation) for 2 minutes. The samples were cleaned with warm water and dried with compressed air. EBSD measurements were performed using a Hitachi SU-70 FE-SEM equipped with an EBSD system from Oxford HKL. The microscope was operated with an accelerating voltage of 20 kV and a probe current of 3 nA. The automatic beam scanning used step sizes of 0.5-0.7 μm. A magnification of 700× was used to analyze the specimens' surfaces. The magnification used to analysis the specimens cross section was chosen depending on their thickness. The SEM/EBSD data were acquired and processed by the Oxford HKL CHANNEL 5 software.

Corrosion form and rate of the samples were investigated in Hank's solution which simulated the ionic composition of blood plasma. The solution was prepared by dissolving Hank's modified salt (H1387, Sigma Aldrich, USA) in deionized water and its temperature and pH were adjusted to 37˚C and 7.4 respectively. The composition of Hank's solution was presented in Ref. [46]. Two different corrosion testing techniques including potentiodynamic polarization and static immersion were applied. Potentiodynamic polarization (ASTM G59) test was carried using a Princeton Applied Research Model 273 galvanostat/potentiostat. A platinum electrode with the surface area of 1 cm^2 was used as counter electrode while an Ag/AgCl saturated electrode was used as reference electrode. Iron foils were cut into pieces of 1 cm^2 surface area each and mounted in acrylic resin. The surface was then polished with 2400 and 4000 grit SiC paper before the electrochemical testing. The corrosion current density was determined from Tafel extrapolation of the resulting potential-current curves and the corrosion rate was subsequently calculated based on the corrosion current density according to the following equation [52]:

$$CR = - \frac{EW}{\rho}$$ **Equation 6.1**

In this equation CR is the corrosion rate (mm $year^{-1}$), i_{corr} is the corrosion current density (μA cm^{-2}), EW is the equivalent weight (28 g eq^{-1} for Fe) and ρ is the material density in g cm^{-3} (7.87 for Fe).

In static immersion test, based on ASTM G31 standard [135], iron specimens (20×10×0.1 mm^3) were polished by 4000 grit SiC paper, cleaned in ultrasonic bath by deionized water and ethanol, dried and weighted. They were then immersed in Hank's solution for 336 h (14 days). After that period, the specimens were removed from the solution, rinsed by water and ethanol and dried. The degradation layer was then removed by peeling. The specimens were subsequently rinsed with deionized water and ethanol, dried and stored in desiccator for 48 h before being weighted. Degradation rate was calculated based on the weight loss of specimens according to Equation 6.2,

$$DR = \frac{W}{A.t.\rho}$$ **Equation 6.2**

where *DR* is the degradation rate in mm per year (mm y^{-1}), *W* is the weight loss (g), *A* is the area (cm^2), *t* is the time of exposure (h) and ρ is the density (g cm^{-3}). The surface of samples after the degradation products were removed was studied using SEM to identify the form of corrosion in the surface.

6.5 Results

6.5.1 Microstructure

SEM images of the surface morphology of iron (electrodeposit-bath interface) deposited at different current densities are presented in Figure 6.1. In this Figure, electrodeposit-bath interface is shown as this surface can better show the effect of current density on crystalline growth of the iron foils. As the images show, the crystallite size appeared to decrease with the increase of current density from 1 to 10 $A.dm^{-2}$. The shape of the crystallites also changed significantly with increasing of the current density as they appeared to be sharper at higher current densities.

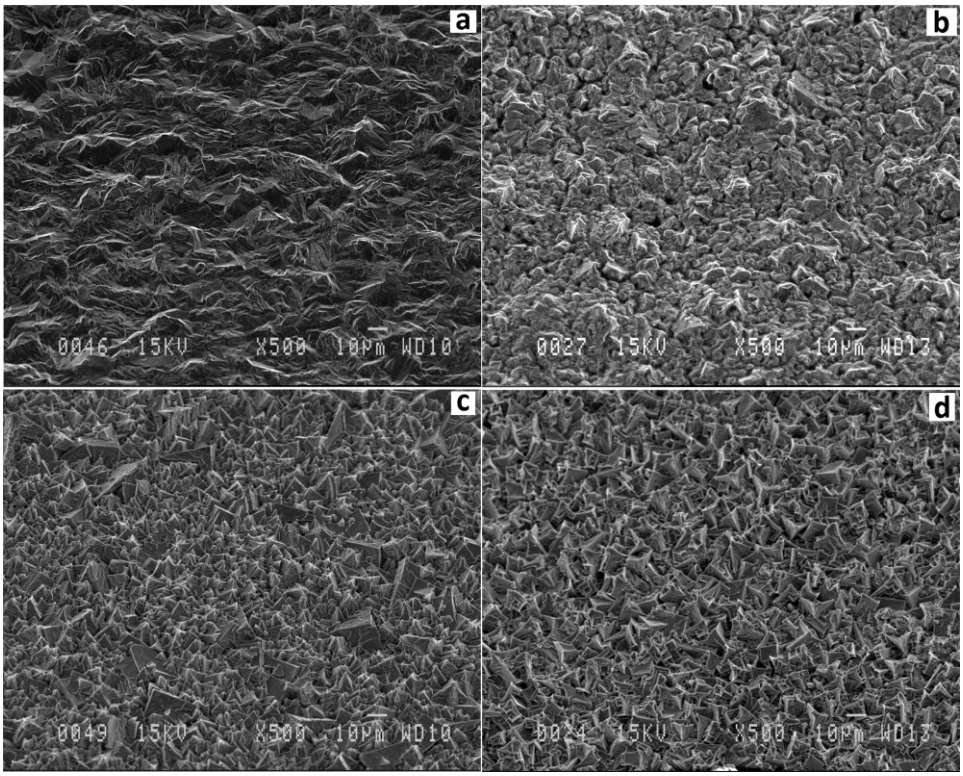

Figure 6.1- Surface morphology of electroformed iron deposited at (a) 1, (b) 2, (c) 5 and (d) 10 Adm^{-2}.

Figure 6.2 shows the color key code inverse pole figure used for OIM imaging. Figure 6.3 presents the normal direction orientation EBSD maps in the color-key mode of the cathodic surfaces and cross-sections of electroformed iron. The cathodic surface was selected for microstructural studies and corrosion testing since this surface would be the one in contact with blood (more corrosive attack) if an electroformed iron stent is implanted. The grain size distribution charts showed in Figure 6.3 are related to the surface images. For the studied iron samples, the values of the average grain size and the maximum texture intensity as expressed in MUD (mean uniform distribution) are presented in Table 6.1.

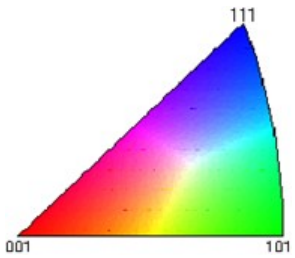

Figure 6.2- Color key code inverse pole figure used for OIM imaging.

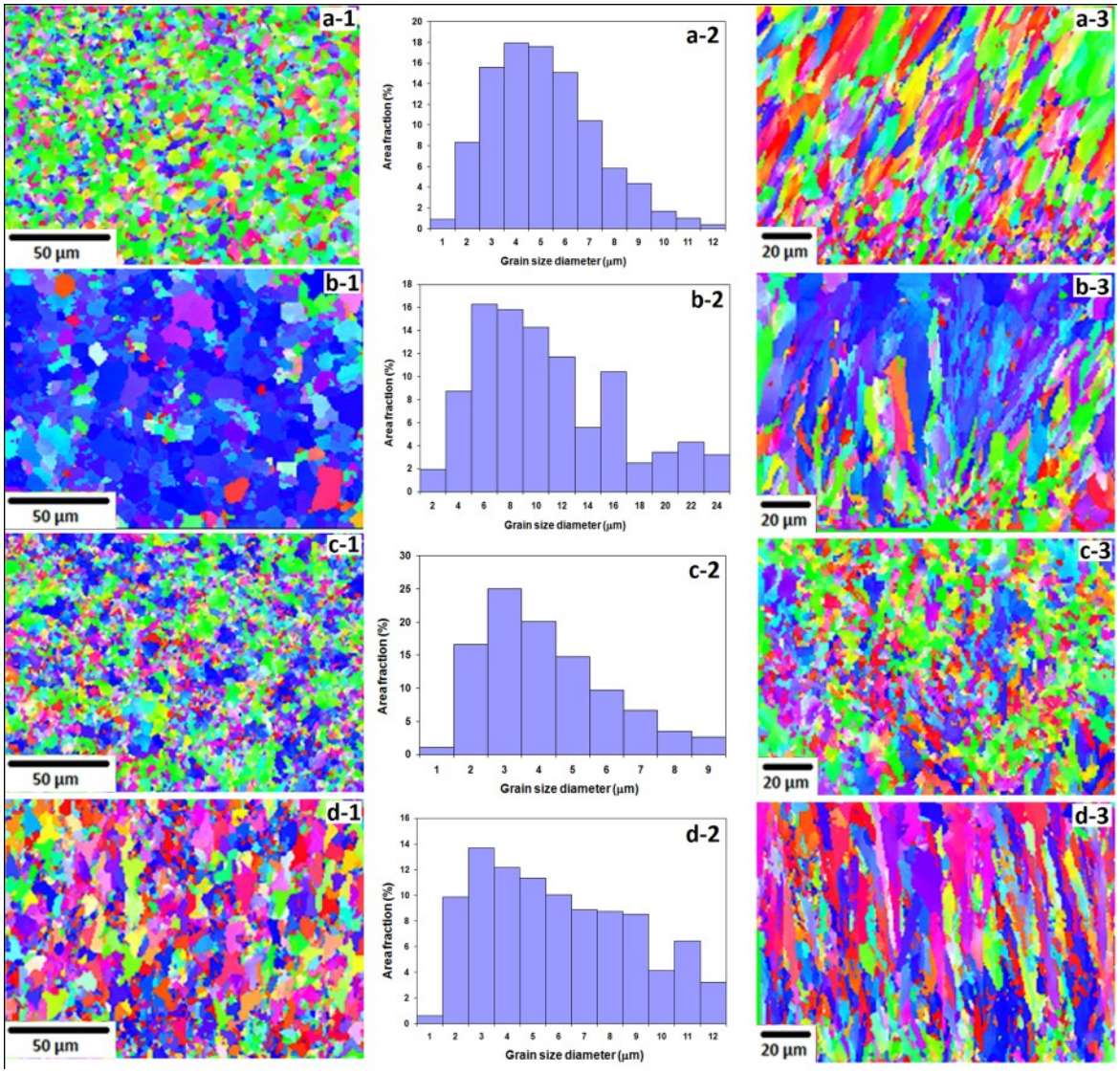

Figure 6.3- Normal direction maps as shown with color key code inverse pole figure and grain size distribution of iron electrodeposited at : (a) 1, (b) 2, (c) 5 and (d) 10 Adm^{-2}. Column 1 displays the surfaces while column 3 shows the cross-sections of the electrodeposited samples.

Table 6.1- Average grain size and preferential orientation information of electrodeposited iron as determined from Figure 6.3.

Current density	1 Adm^{-2}	2 Adm^{-2}	5 Adm^{-2}	10 Adm^{-2}
Average grain size (µm)	2.5	4.4	2.5	3

Preferential orientation	<1 0 1>//ND	<1 1 1>//ND	<1 1 1>//ND	<1 1 2>//ND
Maximum texture intensity (MUD)	2.28	7.39	1.69	1.37

At current density of 1 Adm^{-2} a fine-grain microstructure was produced with the average grain size of ~ 2.5 μm. Although strong fiber texture was not observed for iron deposited at this current density, there was a weak preferential orientation of grains with (1 0 1) planes parallel to the sheet surface (green grains). The maximum intensity of this <1 0 1> fiber texture was 2.28 MUD. According to the grain size distribution chart, most grains are smaller than 4 μm while few larger grains could be observed. The cross section image shows small equiaxed grains in the cathodic face of the layer which was formed on the substrate (the lower part of Figure 6.3.a-3). These equiaxed grains were seen in the first 20 μm of the layer thickness and later grew to columnar larger grains and as shown in Figure 6.3.a-3, the grains are larger in the center and upper part of the iron layer. As the current density increased to 2 $A.dm^{-2}$, a strong texture in the normal direction (i.e <1 1 1> fiber texture) with a density of 7.39 MUD was found in the perpendicular direction to the surface of iron film (blue grains). It can also be seen that the grains were larger for the film deposited at 2 $A.dm^{-2}$ compared to the 1 $A.dm^{-2}$ (4.4 μm versus 2.5 μm). The cross-section image (Figure 6.3.b-3) confirms also the preferential orientation of <1 1 1>//ND and shows the presence of columnar grains almost all over the thickness of iron film. An increase in the current density to 5 $A.dm^{-2}$ resulted in grain refinement and a significant change in texture. The strong <1 1 1> fiber texture cannot be found for the iron film deposited at this current density and the grain orientation is almost random and composed of two weak <1 1 1>//ND and <1 0 1>//ND textures. The average grain size also decreased to 2.5 μm. As Figure 6.3.c-3 demonstrates, no columnar growth could be seen for this current density and all grains were equiaxed in cross-section. However, at 10 $A.dm^{-2}$, a slight grain growth was observed for iron films with strong columnar growth as shown in Figure 6.3.d-3, and a weak <1 1 2> texture in the normal direction was noted (pink grains).

Annealing of the electrodeposited iron at 550˚C significantly changed its microstructure and texture as illustrated in Figure 6.4. Annealing resulted in recrystallization in all iron films deposited at different current densities. After annealing, iron deposited at 1 $A.dm^{-2}$ recrystallized with a slight grain growth as the average grain size increased from 2.5 to 3.7

µm. The preferential orientation of <1 0 1>//ND also change to a stronger texture <1 0 1>//ND with the maximum intensity of 2.8 MUD. The cross-section image (Figure 6.4.a-3) shows that the columnar grains changed after annealing to more equiaxed grains with different sizes depending on the layer thickness. Indeed, the initial grains formed on the substrate are still much finer than the ones on the outer layers which grew more significantly by annealing.

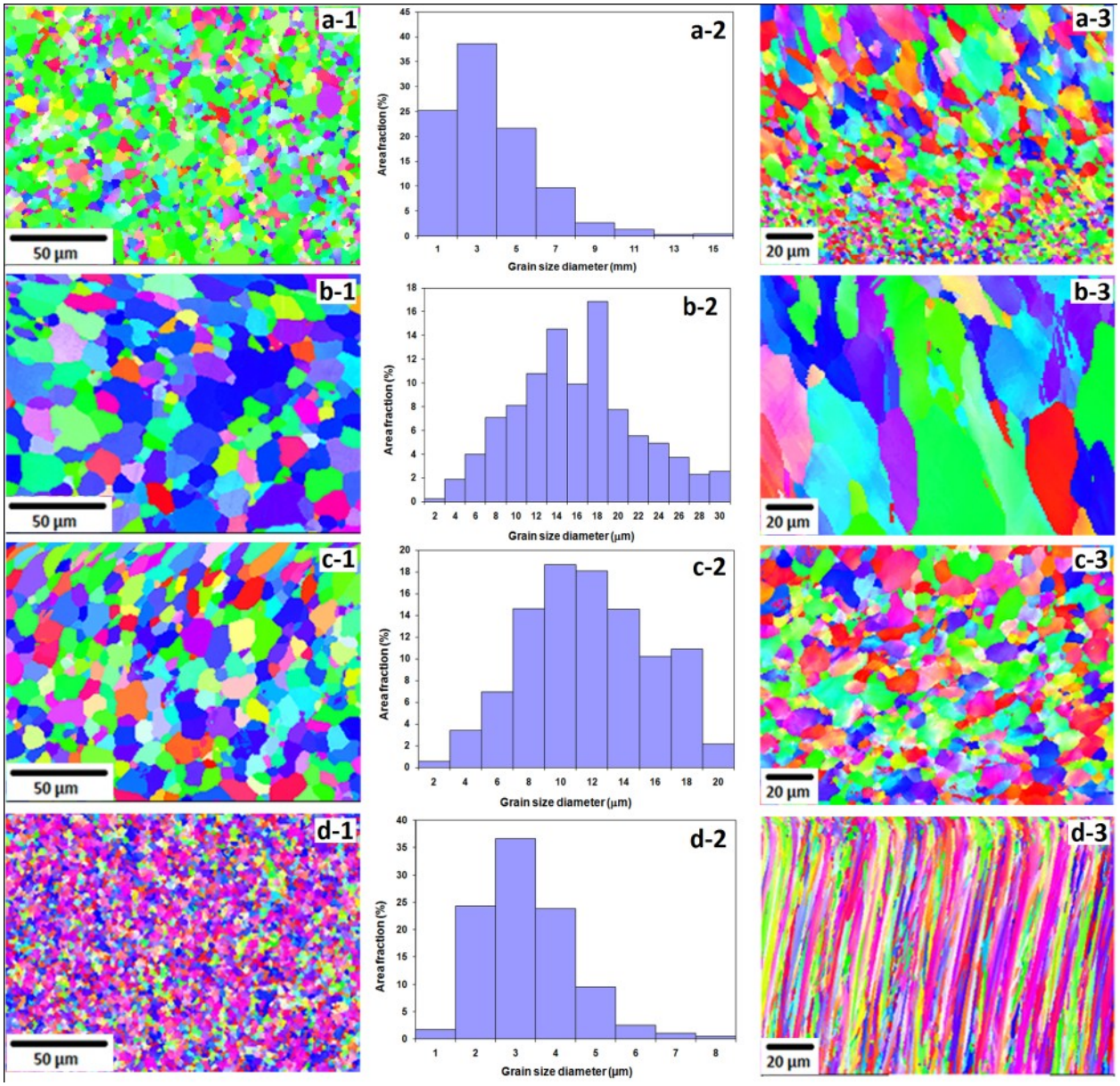

Figure 6.4- EBSD orientation images and grain size distribution of iron electrodeposited at (a) 1, (b) 2, (c) 5 and (d) 10 Adm^{-2} annealed at 550˚C for 1 h. Column 1 displays the surfaces while column 3 shows the cross-sections of the annealed samples.

Table 6.2- Average grain size and preferential orientation information of electrodeposited iron annealed at 550˚C for 1 h. Data were extracted from Figure 6.4.

Current density	1 Adm^{-2}	2 Adm^{-2}	5 Adm^{-2}	10 Adm^{-2}
Average grain size (μm)	3.7	7.6	6.1	1.9
Preferential orientation	<1 0 1>//ND	<1 1 1>//ND	<1 1 1>//ND	<1 1 2>//ND
Maximum texture intensity (MUD)	2.8	3.54	1.64	2.31

For iron film deposited at 2 $A.dm^{-2}$, annealing resulted also in both recrystallization and grain growth. The intensity of <1 1 1> fiber texture component decreased from 7.4 to 3.5 MUD showing that annealing produced a more random distribution of grains while the average grain size nearly doubled by the annealing. After annealing, the presence of columnar grains is still visible although their shape and size has changed due to recrystallization and grain growth. A similar behavior was observed for iron deposited at 5 $A.dm^{-2}$. Annealing increased the grain size from 2.5 to 6.1 μm which confirms the significant grain growth induced by the thermal treatment. However, there was no change in texture after annealing. Iron film electrodeposited at 10 $A.dm^{-2}$ recrystallized to a finer microstructure. The average grain size decreased from 2.5 to 1.9 μm. However, unlike the other iron films, the initial texture component increased after annealing as the intensity of <1 1 2> fiber increased to 2.31 MUD. The cross-section image of the annealed microstructure (Figure 6.4.d-3) shows that although the columnar grains are formed all over the thickness of the film, their diameter has noticeably decreased. Also, the few equiaxed grains seen in the microstructure before annealing could not be found in the annealed microstructure.

6.6 Corrosion testing

6.6.1 Potentiodynamic polarization

Potentiodynamic polarization curves of as-electrodeposited iron films are presented in Figure 6.5 and the resulting corrosion current density and corrosion potential related to the curves are summarized in Table 6.3. The corrosion current densities were determined from Tafel extrapolation of the curves presented in Figure 6.5. The lowest corrosion current and the highest corrosion potential were observed for iron deposited at 2 A.dm^{-2} showing that it had the lowest corrosion rate and it is the least active among the studied samples. The calculated corrosion rates based on the corrosion currents are shown in Figure 6.6. The highest corrosion current found for iron deposited at 5 Adm^{-2} while the corrosion potentials of Fe-5 and Fe-1 were almost the same. The corrosion rate (CR) of iron films can be ordered as follows: CR Fe-2 < CR Fe-10 < CR Fe-1 < CR Fe-5.

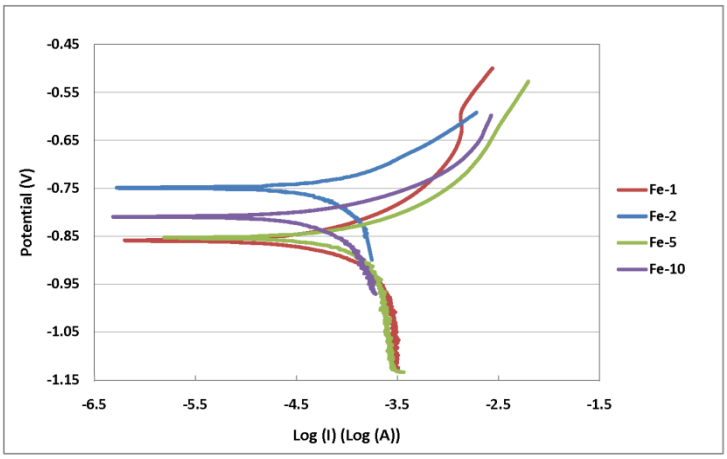

Figure 6.5- Potentiodynamic polarization curves of iron electrodeposited at different current densities.

Table 6.3- Corrosion current density and potential of iron electrodeposited at different current densities: the data were extracted from curves in Figure 6.5.

Electroforming current density (A dm^{-1})		1	2	5	10
Corrosion current density (µA cm^{-2})	i $_{corr}$ (µA cm^{-2})	120	81	161	107
	SD* (µA cm^{-2})	13	7	20	24

Corrosion potential (mV vs. Ref.)	**E_{corr} (mV)**	859	750	853	810
	SD (mV)	9	30	17	16

*standard deviation

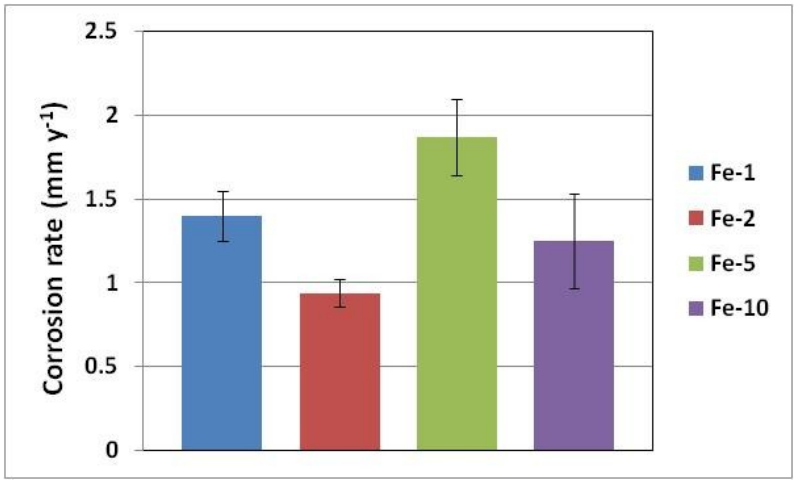

Figure 6.6- Corrosion rates of iron electrodeposited at different current densities: the rates were calculated from corrosion current density values presented in Table 6.3.

After annealing, the potentiodynamic polarization curves of iron electrodeposited films changed as shown in Figure 6.7. It can be seen that for all iron films deposited at different current densities the corrosion potential increased while the corrosion current decreased. This can confirm that annealing decreased the activity of all Fe samples and also decreased their corrosion rate. Among iron films, Fe-5 had the lowest corrosion potential and highest corrosion current. As shown in Table 6.4, Fe-2 showed a lower corrosion potential than that of Fe-1 and Fe-10. However, its corrosion current was also lower than Fe-1 and Fe-1 showing that it had a slower corrosion (Figure 6.8). Although the corrosion rate of electroformed iron decreased after annealing, the same order in corrosion rates was observed for iron films deposited at different current densities i.e. : CR Fe-2 < CR Fe-10 < CR Fe-1 < CR Fe-5.

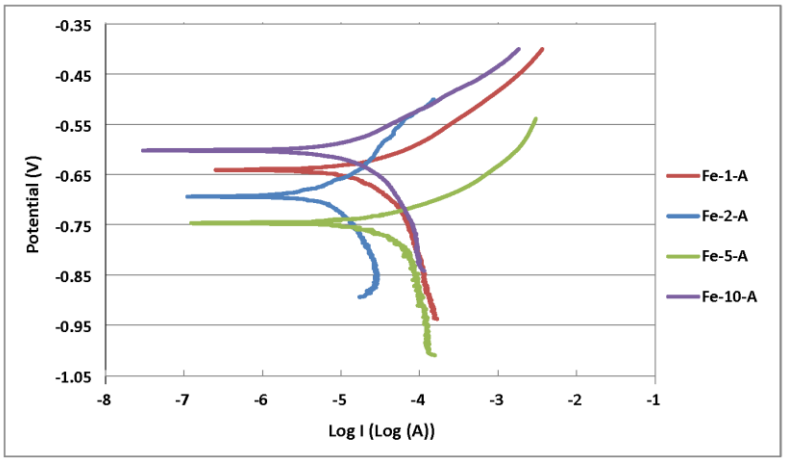

Figure 6.7- Potentiodynamic polarization curves of iron electrodeposited at different current densities and annealed at 550˚C for 1 h.

Table 6.4- Corrosion current density and potential of iron electrodeposited at different current densities and annealed at 550˚C for 1 h: the data were extracted from curves in Figure 6.7.

Electroforming current density (A dm^{-1})		**1**	**2**	**5**	**10**
Corrosion current density (µA cm^{-2})	**i_{corr} (µA cm^{-2})**	83	40	105	63
	SD (µA cm^{-2})	13	8	16	5
Corrosion potential (mV vs. Ref.)	**E_{corr} (mV)**	642	693	747	602
	SD (mV)	13	30	45	18

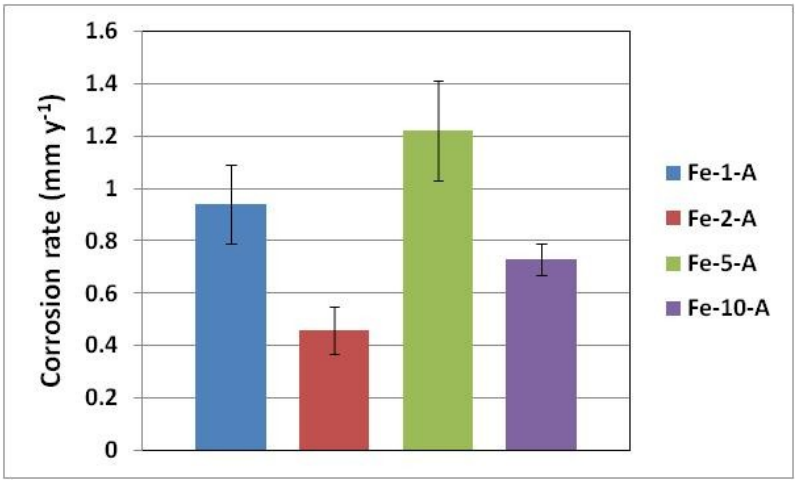

Figure 6.8- Corrosion rates of iron electrodeposited at different current densities: the rates were calculated from corrosion current density values presented in Table 4.

6.6.2 Static degradation

The corrosion rates calculated from the weight loss of iron samples were different from the corrosion rates calculated by potentiodynamic polarization test (Figure 6.9 versus Figure 6.6). The DRs from static tests are much smaller than CRs from potentiodynamic polarization. Fe-5 had the highest DR rate and the order of degradation rates for iron films was almost the same as that of potentiodynamic polarization. However, very small difference in DR was observed for iron samples deposited at 1, 2 and 10 $A.dm^{-2}$ and they had very similar degradation rates.

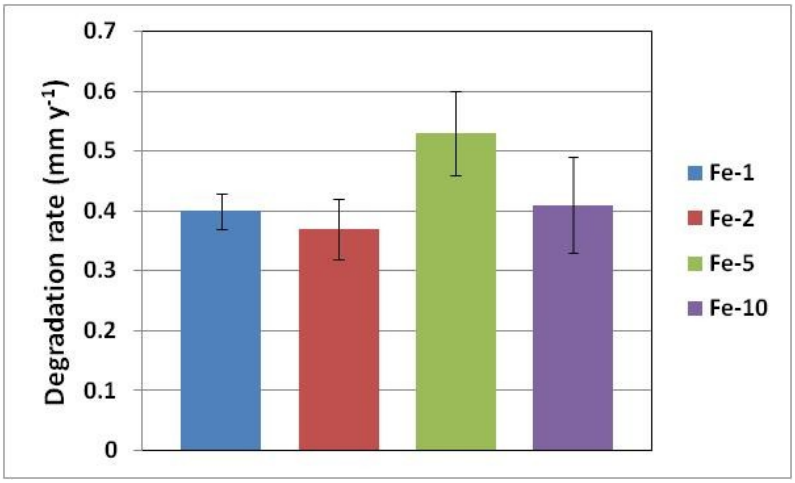

Figure 6.9- Degradation rate of as-deposited iron calculated from static degradation test based on specimen's weight loss during the test.

The morphology of the degraded surfaces showed different corrosion forms for iron films. As Figure 6.10 illustrates, the degradation forms appeared to be uniform for all samples and there was no noticeable localized attack at macroscopic scale. However, in high magnification images shown at the top-left of each figure, microscopically localized degradation can be observed. Fe-1 showed microscopic pitting while the corrosion was more uniform for Fe-2 with a similar effect to etching as the grain boundaries were revealed (Figure 6.10-b). For Fe-5, the corrosion appeared to be more severe with more noticeable pits than other microstructures which is in accordance with its higher DR compared to other samples. The microstructure of Fe deposited at 10 $A.dm^{-2}$ also showed microscopic pitting attack.

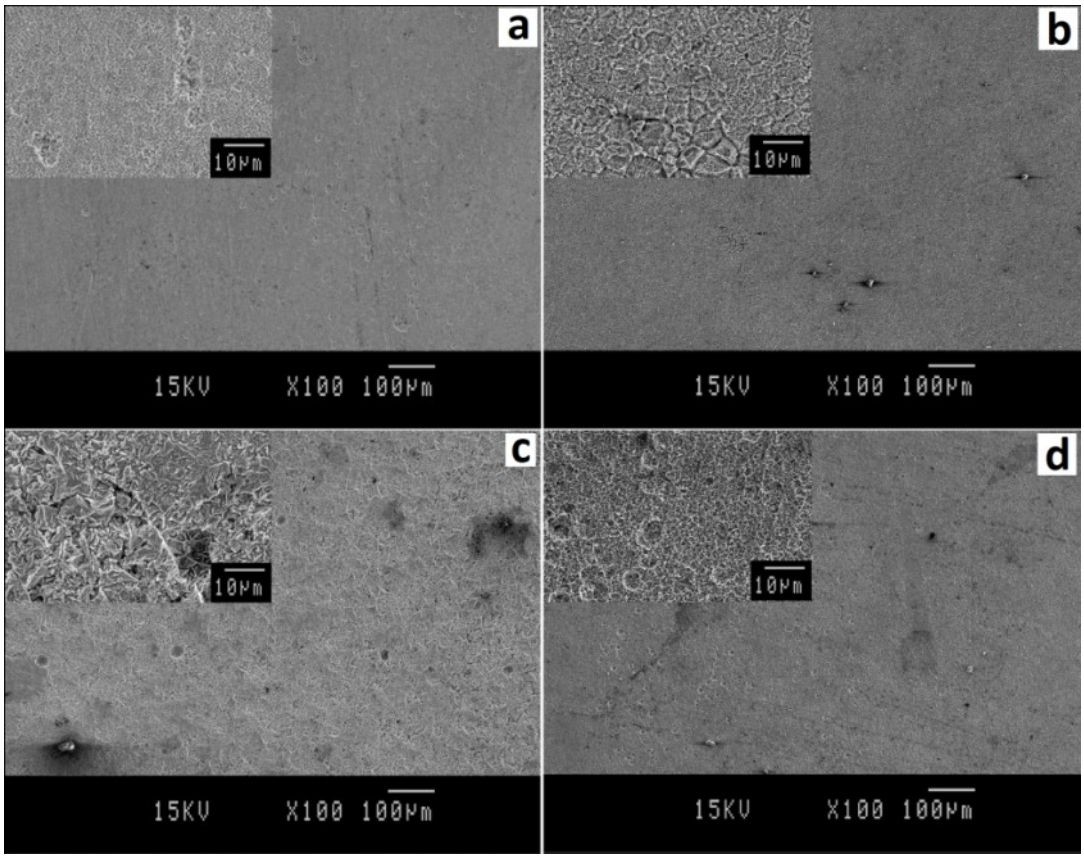

Figure 6.10- Surface morphology of iron deposited at different current densities after static degradation (after the corrosion products were removed). (a) 1, (b) 2, (c) 5 and (d) 10 Adm^{-2}, Small images on top-left show the same surface at higher magnification.

The static DRs of annealed samples were still lower than those of as-electrodeposited sample as was observed for potentiodynamic polarization test. As shown in Figure 6.11, the DR decreased to 0.23-0.28 mm y^{-1} after annealing and the values were in the same range for all the iron films.

Despite the difference in degradation morphology of annealed Fe samples, no obvious localized attack was observed (Figure 6.12). The degradation morphology was similar to etching effect in Fe-1 and Fe-2 as the grain boundaries can be seen for these microstructures. The corrosion attack appeared to be more intense for Fe-5 and Fe-10 which can be confirmed by their slightly higher DR rate.

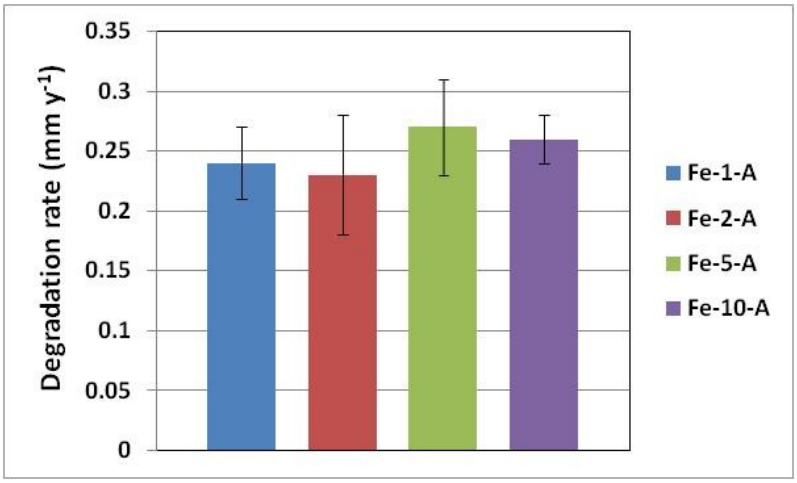

Figure 6.11- Degradation rate of electroformed iron annealed at 550˚C calculated from static degradation test based on specimen's weight loss during the test.

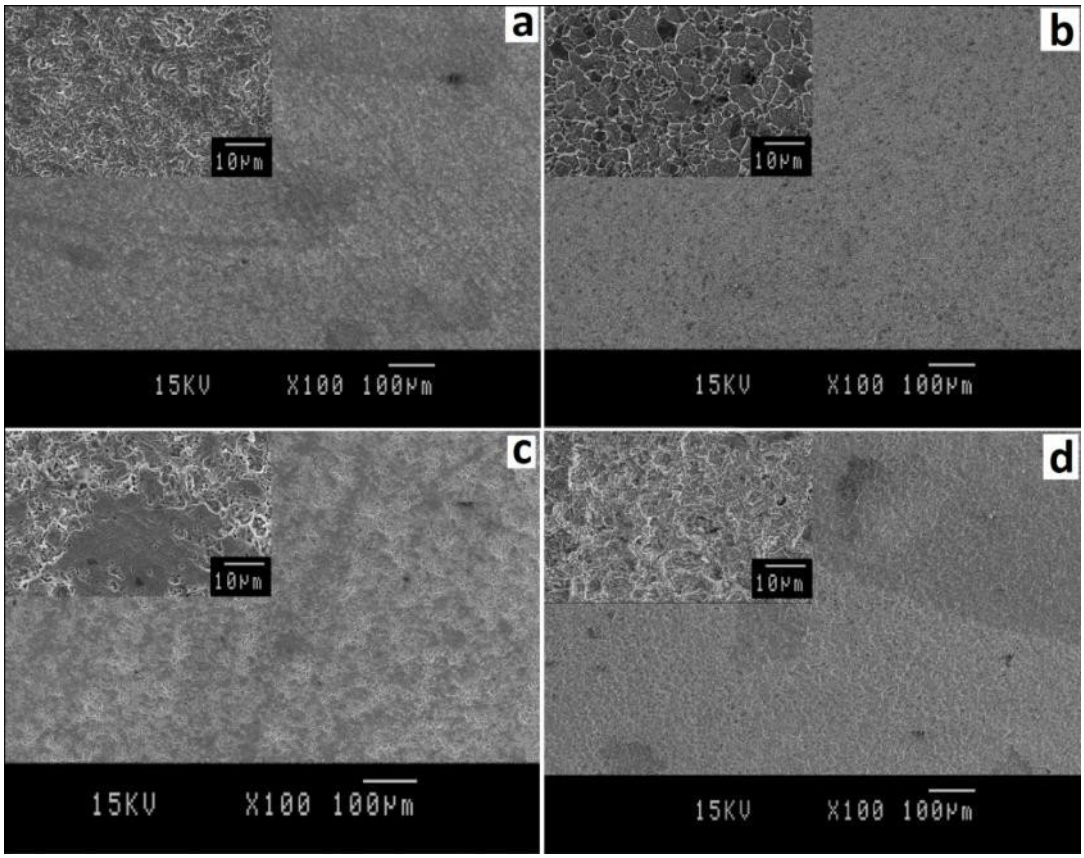

Figure 6.12- Surface morphology of iron deposited at different current densities and annealed at 550 ˚C after static degradation (after the corrosion products were removed). (a) 1, (b) 2, (c) 5 and (d) 10 Adm^{-2}, Small images on top-left show the same surface at higher magnification.

6.7 Discussions

6.7.1 Microstructure

Electrodeposition is a feasible method to produce metallic layers with different microstructures and properties. Many parameters are involved in the electrodeposition process including the type of electrolyte, the concentration of ions, pH, the bath temperature, the degree of agitation, the substrate overpotential and/or current density, the mode of deposition (d.c. versus pulse plating), and the presence of additives in the electrolyte. In this work we found that current density strongly influenced the microstructure of electrodeposited iron. As Figure 6.1 shows, at 5 and 10 A.dm^{-2} well-faceted grains can be observed on the surface morphology of iron which are different from

the morphology of Fe-1 and Fe-2. The appearance of faceted grains with pyramidal shapes at 5 and 10 A.dm^{-2} might be explained by the significant evolution rate of hydrogen gas bubbles which increases with current density [88]. It is also generally believed that increasing the current density results in a decrease in the crystallite size of electrodeposits by increasing the nucleation rate [106]. This hypothesis primarily seemed to be true in this study as the crystallites appeared to be smaller and sharper as the current density increased from 1 to 10 A.dm^{-2} (Figure 6.1). However, some believe that higher current densities result in the increase of crystallite size and surface roughness [149]. Jartych et al. [121] observed an increase in the crystallite size of iron layer electrodeposited from chloride solution when the current density increased from 0.8 to 1.6 A.dm^{-2}. Based on our results from EBSD, we found that there was no direct correlation between the electrodeposition current density and crystallite size. At 1 A.dm^{-2} a fine microstructure with the average grain size of 2.5 μm and a weak <1 0 1>//ND texture was formed. The growth of columnar grains observed in the cross-section image (Figure 6.3.a-3) is a common property of electrodeposited metals in which the diameter of columnar grains increases with the deposit thickness. Li et al. [150] observed that at lower current densities i.e. 0.1 – 1 A.dm^{-2}, <1 1 0> texture was obtained for iron electrodeposited from chloride solution at 70˚C and pH=1.7. Since (1 0 1) and (1 1 0) planes belong to the same family of planes in bcc structure, it can be speculated that our result was similar to those previously obtained. Yoshimura et al. [106] also observed by XRD that the orientation index of (1 1 0) planes in electrodeposited iron (in a ferrous chloride-calcium chloride solution at pH= 2 and T=40˚C) was at its maximum when the current density was in the range of 0.1 - 1 A.dm^{-2}.

In this study, when the current density increased to 2 A.dm^{-2} a highly <1 1 1> oriented texture was formed and the grain size increased. The increase of the grain size can be related to the presence of the texture which results in the growth of previously formed grains with (1 1 1) planes parallel to the sheet surface and inhibits the formation of new grains in other directions. Different theories have been developed to explain the texture formation during electrodeposition. The most realistic is called the geometrical selection theory, which suggests that the texture formation is attributed to the difference in the advance rate between different planes, and also attributed to the deposit surface morphology. In case of iron, it has been demonstrated that the texture growth resulted from

minimizing the free energy of the system, and that the surface energy anisotropy played an important role in the formation of fiber texture which changes by varying the current density and other deposition parameters [150]. The microstructure changed significantly when the current density was increased to 5 $A.dm^{-2}$. The strong (1 1 1) texture almost disappeared and the grain size decreased to ~ 2.5 μm. Unlike Fe-1 and Fe-2, in which columnar grains were formed, equiaxed grains were observed in the cross-section of Fe-5 without the presence of columnar grains. For electrodeposited metals, in order to obtain equiaxed grains, continuous nucleation of new grains should occur during the deposition. In general, factors that promote the formation of defects (e.g., dislocations and twins) tend to reduce the crystallite size of metallic deposits [149]. Fe film deposited at 5 $A.dm^{-2}$ had a higher density of observable defects such as porosity compared to other Fe films. Generally, the increase of the current density leads to the formation of more defects in the microstructure. Therefore, the grain refinement and the formation of equiaxed grains can be attributed to the presence of more microstructural defects for Fe-5. Increasing the current density to 10 $A.dm^{-2}$ resulted in a decrease in the texture intensity and a change into (1 1 2) texture. The increase in texture index of (2 1 1) planes (similar to (1 1 2) planes in bcc system) at current density of 10 $A.dm^{-2}$ was already reported by Yoshimura et al [106]. The overall decrease in texture density is attributed to an increase of the nucleation rate when the current density increases; the increased nucleation does not favor the selective grain growth, and is, therefore, responsible for lowering the texture strength as the deposition rate increases [150]. Although a decrease in grain size was expected for Fe-10, it slightly increased to ~ 3 μm with the increase of current density and the columnar grains were observed. The increase in the grain size can again be related to the growth of columnar grains, though their formation at such a high current density is not clear. Jartych et al. [121] mentioned that at higher current densities, dendrite structures are formed leading to the formation of coarser and spongy electrodeposits. This could therefore be the reason for the slight grain coarsening in Fe-10. Generally, the changes in texture of electrodeposited Fe with the deposition condition could be attributed to the hydrogen co-deposition which may modify the surface-energy anisotropy of the deposit. When the hydrogen co-deposition takes place, it affects the surface energy of the deposit and the surface energy is lowered. Lowering the surface-energy is different for various crystallographic planes because of their different adsorption

abilities. It is, therefore, expected that, as the hydrogen co-deposition increases, the texture will change from one type to another, due to the changes in the surface-energy anisotropy [150,151].

The annealing of different electrodeposited metals even at low temperatures has been shown to change significantly their microstructure through recovery and recrystallization. It has been shown that the activation energy for recrystallization of electrodeposited copper is considerably less, by a factor of two to three, than that for recrystallization of the bulk wrought copper [77]. For Fe-1, the recrystallization of a new microstructure with larger grains and stronger texture after annealing confirms this hypothesis. Electrodeposited metals contain a large concentration of point (vacancies), linear (dislocations) and planar defects (twins). These defects originate intrinsically as a result of the electrodeposition process. They increase the stored energy of the metal which is the activation energy for recrystallization upon annealing. The defect movement is thermally activated and annealing of deposits produces large changes in the electron transport, mechanical, crystallographic texture, and microstructural characteristics. During annealing, the defects either merely rearrange themselves in a different configuration (recovery), or anneal out, reducing the defect concentration and causing corresponding microstructural changes (recrystallization) [76]. The probability of nucleation in each grain during recrystallization is related to the stored energy of that grain. Therefore, the nucleation of new grains is closely related to the initial orientation of each grain before annealing. The slight grain growth observed after the annealing of Fe-1 can be due to the fact that its recrystallization temperature was slightly lower than the annealing temperature of 550˚C and therefore, grains growth occurred after recrystallization. For Fe-2, a more significant grain growth was observed after annealing. This can be explained possibly by the higher quantity of stored energy by electrodeposition at 2 $A.dm^{-2}$ which had a strong <1 1 1>//ND texture. It has been shown that in cold-rolled iron, <1 1 1> texture contains more stored energy than other textures [152]. This can lead to the initiation of recrystallization of iron at lower temperatures and consequently grain growth at 550˚C.

Although the intensity of <1 1 1>//ND texture in Fe-2 decreased by recrystallization and the formation of a more random orientation was observed, it retained a texture density of 3.54 MUD which relates to the higher stored energy of <1 1 1> texture. Hansen et al. [153] have

reported that the electrodeposited silver microstructure consisted of nanocrystalline grains with strong preferred grain orientations transformed during room temperature storage into a self-annealed microstructure with considerably larger grains and altered preferred orientations. Since the nucleation factor for (1 1 1) grains is higher than other orientations due to their higher stored energy, the probability of formation of these grains is higher. The presence of (1 1 1) texture with a density of 3.54 MUD after the recrystallization of Fe-2 can be explained based on this theory.

Grain growth was also observed for Fe-5 after annealing without any noticeable changes in the texture. As the density of defects increases with current density, a higher stored energy could be expected for Fe-5 and therefore, recrystallization could occur at lower temperature. Hence, heating at 550˚C resulted in grain growth as observed in Figure 6.4. However, this behavior was not observed for Fe-10. The <1 1 2>//ND texture intensity increased and the grain size decreased with annealing. This observation might be due to a second recrystallization in microstructure. As the density of structural defects was supposed to be higher at 10 $A.dm^{-2}$, first recrystallization could have happened at lower temperatures leading to the formation of a randomly oriented microstructure. A second re-crystallization started at higher temperatures which once again arranged the crystallites along the (1 1 2) planes parallel to the sheet surface and formed fine columnar grains during the annealing process. Such observation of two-step recrystallization during annealing has been reported by Qi et al. [154] and Enriquez et al [155,156] for electrodeposited CdTi films.

6.7.2 Corrosion and degradation testing

Degradation of metallic implants in corrosive media such as physiological media is affected both by the properties of the materials (e.g. composition and microstructure) and the properties of the electrolyte (e.g. pH, temperature, ions, etc). As our aim was to develop and evaluate degradable electroformed iron for stents, this study focused on the effect of microstructure on degradation in a physiologically-simulated electrolyte (Hank's solution). For many materials, the susceptibility of single crystals to corrosion has been shown to be related to crystallographic orientation. Therefore, it is expected that electrodeposited iron films with different textures show different degradation rates and forms. Potentiodynamic polarization test showed different corrosion rates for iron films electrodeposited at different

current densities. It is believed that in the case of bcc Fe single crystals, the close-packed planes be the most susceptible to pitting corrosion [129]. Schreiber et al. [156] studied the effect of grain orientation and grain boundaries on anodic dissolution rate of iron and found that grains with (1 1 1) planes parallel to the surface had the highest dissolution rate. They presented a geometrical model to explain the correlation between electrochemical behavior and atom density on (1 0 0), (1 0 1) and (1 1 1) planes in iron. They explained that although (1 1 1) has the largest atom density in the top layer, the distance to the next layer is larger and the surface atoms are less strongly bound. (1 0 1) has also large distance to the next atom layer and trenches in the surface, which mean a partial hydration of the surface atoms. Therefore, these planes are more susceptible to corrosion. However, (1 0 0) plane seems to be the most stable against active dissolution. The surface shows trenches, but the next iron layer is closer to the top layer compared with the other orientations. Hence, this stabilizes the surface atoms against corrosion [146]. We observed that the lowest corrosion rate was found for Fe-2 which had a strong <1 1 1>//ND texture. The reason for this contradiction can be attributed to the largest average grain size of Fe-2 compared to other iron foils. It can be seen from Figure 6.3-b that Fe-2 had the largest grains and therefore the lowest volume of grain boundaries. Since grain boundaries have a higher potential for corrosive attack than the grains, Fe-2 was less prone to corrosive attack and had therefore a slower corrosion. Fe-10 had a higher corrosion rate that Fe-2 but lower than that of Fe-1 and Fe-5. The microstructure of Fe-10 showed randomly-oriented grains (weak <1 1 2>//ND texture) with columnar grains smaller than those of Fe-2 but larger than those of Fe-1 and Fe-5. Its corrosion rate was therefore higher than Fe-2 because of its higher volume of grain boundaries and also higher density of microstructural defects. The highest corrosion rate was found for Fe-5. It had smallest average grain size with equiaxed grains which could provide it with the highest volume grain boundaries. Also, additional porosity was observed for Fe-5 than for other samples showing that it could have more structural defects and hence, a faster corrosion attack. Fe-1 showed the second highest corrosion rate. Although Fe-1 deposited at the slowest rate, it has smaller grains than that of Fe-2 and a weak <1 0 1>//ND texture. Since (1 0 1) planes are considered to be close-packed in bcc structure, it could be considered more susceptible to corrosion attack than other planes [157]. The presence of (1 0 1) planes parallel to the surface can therefore play a role in the faster corrosion of

Fe-1 compared to Fe-2 and Fe-10. Although it has already been shown that grains with (1 1 1) planes parallel to the surface are the most susceptible grains to corrosion attack in iron, the presence of other grains with different orientations and thereby corrosion susceptibilities could increase the overall corrosion rate as (1 1 1) can act as anodic sites in presence of more «cathodic» grains. This can explain the higher corrosion rate of Fe samples which had weaker textures compared to Fe-2.

Although the grain size and microstructure of Fe samples change after annealing, the same order in their corrosion rate was observed. Basically, the corrosion rate of all samples decreased significantly after annealing. This is due to the fact that annealing induces recrystallization in iron films which reduces the density of structural defects of as-deposited material also release the internal stress produced by electrodeposition. The decrease in the volume fraction of grain boundaries due to annealing can be another reason for the decrease in corrosion rate. The newly recrystallized grains are therefore less susceptible to corrosion and this can decrease the overall corrosion rate. Annealed Fe-2 had the lowest corrosion rate as its grains were the largest among all microstructures. Fe-5 showed the highest corrosion rate in spite of its grain growth. The presence of equiaxed grains could be the reason for this behavior. Elongated grains were still present after annealing of Fe-1 and Fe-10 which can reduce the total volume of grain boundaries. In Fe-10, small grains observed in the surface (Figure 6.4.a-1) were elongated all over the thickness of the film, shown in cross-section image, which reduced the grain boundary volume. Also, a <1 1 2> texture formed after annealing of Fe-10 which could slightly reduce its corrosion rate as (1 1 2) planes are less closely-packed and therefore less susceptible to corrosion.

The values of degradation rates calculated from static immersion tests were lower than those determined from potentiodynamic polarization tests. This was due to the formation of a degradation layer on the surface of the samples after 24-48 h of immersion. This degradation layer was found to be composed of iron, oxygen, phosphorus, chlorine and calcium [144] and decreased the degradation rate of all samples. Since the degradation after the formation of this layer should continue by the diffusion of Fe ions through the layer, slower degradation rate is obtained compared to potentiodynamic polarization test which is a rapid corrosion testing in which the surface remains intact until the last stages of the test. Potentiodynamic polarization of Fe-2 showed a decrease in the rate of its anodic reaction

compared to other samples which can be related to the initial formation of corrosion products on its surface. The static degradation corrosion rates of iron samples determined from immersion tests were in the following order: Fe-2 < Fe-1 ≤ Fe-10 < Fe-5. This order is in accordance which that of corrosion rates determined from potentiodynamic polarization tests. However, the values of the degradation rates varied from 0.35 to 0.52 mm y^{-1} with a slight difference between the studied samples. This is obviously attributed to the formation of degradation layer on the surface of the samples which not only lowers the degradation rate but also reduces the effect of microstructure of each samples on its degradation rate since the surface would not be exposed directly to the electrolyte. However, the morphologies of the degraded surface of the samples were different after the degradation layer was removed. Fe-2 was the only microstructure in which microscopic pits were not observed. Since Fe-2 has a very strong <1 1 1> texture, its uniform degradation can be related to this texture. Microscopic pits observed for other microstructures including Fe-1, Fe-5 and Fe-10 could be caused by their more randomly distributed grains and textures. Because the susceptibility of different crystallographic planes are not the same for polycrystalline materials, the grains oriented in more susceptible directions could act as anodic sites and localized attack (pitting) occurs. Also, structural defects produced by electrodeposition including porosity, dislocations, grain boundaries, twins, etc. could play an important role in the formation of anodic sites and thereby micropits. These micropits showed to increase the total degradation rates compared to Fe-2 which had the more uniform degradation and therefore could be interesting for application as degradable stents. A more rapid corrosion is desired for pure iron as a degradable metal for stents since its *in vivo* degradation is slower than the value calculated *in vitro*. The reason for the slower *in vivo* degradation is that the stent material is covered firstly by blood and then by cells after the implantation [3]. The presence of micropits could be beneficial provided that they are shallow and uniformly distributed in order to avoid any deeper localized attack which could lead to the failure of implant.

After annealing the static degradation rates of the samples decreased to 0.23-0.27 mm y^{-1} which can be related to the effect of heat treatment on microstructure. However, the DRs of all samples after annealing were nearly the same because the microstructural effects on degradation were reduced by the formation of degradation layer. The uniform degradation

observed for all iron samples after annealing (Figure 6.12) can be attributed to the decrease in the density of structural defects and internal stress which are actually considered to increase the formation of localized corrosion.

6.8 Conclusions

Electroformed iron films with different texture and microstructure were effectively produced by varying the electrodeposition current density to 1, 2, 5 and 10 $A.dm^{-2}$. Iron deposited at 2 $A.dm^{-2}$ had a strong <1 1 1>//ND texture with the average grain size of ~ 4 μm while other films had more randomly oriented microstructures with smaller grain size and weak <1 0 1>//ND and <1 1 2>//ND textures. Annealing at 550˚C for 1 h was found to change the microstructure of electroformed iron by inducing recrystallization. In Fe-10, annealing resulted in recrystallization of new finer grains compared to as-electrodeposited iron while in Fe-1, Fe-2 and Fe-5, grains growth was observed after annealing. Recrystallization of electrodeposited iron after annealing can be attributed to the high amount of stored energy in the material due to the high density of structural defects produced by electrodeposition. The study of the corrosion of electroformed iron by potentiodynamic polarization revealed that texture and microstructure including grain boundaries volume fraction play an important role on the corrosion rates. The corrosion rate of iron samples increased by changing the current density in the following order: Fe-2 < Fe-10 < Fe-1 < Fe-5. In the case of the immersion tests, the effect of microstructure on degradation rate was less significant especially after annealing since in long-term degradation testing, a degradation layer is formed shortly after the test which inhibits the direct contact of the sample surface with the electrolyte. Different degradation morphologies were observed for iron samples deposited at different current densities after the static test. Fe-2 with strong <1 1 1>//ND texture showed the most uniform degradation form while other samples developed micropits caused by preferential corrosion attack on different grains. The formation of micropits could be interesting for the application of electroformed iron as degradable stent material since they can increase the overall degradation rate. The study of the distribution of pits and the long term degradation evaluation of iron samples deposited at different current densities is mandatory to ensure that the localized attack would not lead to mechanical failure of the implant.

Chapter 7. Fabrication of iron degradable stent from electroformed tube

7.1 Résumé

Un processus d'électroformage a été développé pour produire des tubes de fer pour la fabrication de stents. Un substrat cylindrique en étain a été utilisé comme cathode sur laquelle les tubes de fer ont été déposés. Les tubes de fer ont été ensuite polis et coupé au laser pour produire des stents. Un traitement thermique de recuit a été réalisé à 550 °C pendant 1 h afin de réduire la contrainte interne de l'électrodéposition et de la découpe au laser ainsi que pour induire la recristallisation. Un décapage à l'acide a ensuite été effectué pour retirer les parties non désirées du stent ainsi que les bavures de découpe au laser. La microstructure du tube électroformé, du tube coupé, du tube recuit et du stent après décapage à l'acide a été étudiée en utilisant le microscope électronique à balayage et la microscopie optique après attaque chimique avec une solution de nital à 2%. Les résultats ont montré que les stents de fer pourraient être fabriqués avec succès à partir du tube du fer électroformé en utilisant la méthode de découpe au laser. La microstructure du tube électroformé est composée de grains colonnaires recristallisés avec des grains fins et équiaxes d'une taille moyenne de 5 µm après recuit. Cette microstructure à grains fins pourrait fournir des propriétés mécaniques élevées pour les stents de fer électroformés.

7.2 Abstract

An electroforming process was developed to produce iron tubes for fabrication of stents. Cylindrical Sn substrate was used as cathode on which iron tubes were electrodeposited. Iron tubes were then ground and laser-cut to produce stents. Annealing was performed at 550˚C for 1 h in order to reduce the internal stress from electrodeposition and laser-cutting and to induce recrystallization. Acid pickling was subsequently performed to remove the undesired parts of stent was well as laser cutting burrs. The microstructure of as-

electroformed tube, as-cut tube, annealed and acid pickled stent was studies using scanning electron microscope and optical microscope after etching with 2 % nital solution. The results showed that iron stents could be successfully fabricated from electroformed tube using laser cutting method. Microstructure of electroformed tube showed columnar grains which recrystallized to fine equiaxed grains with the average size of 5 μm upon annealing. This fine-grain microstructure could potentially provide high mechanical properties for the electroformed iron stents.

7.3 Introduction

The use of metallic stents for the treatment of occluded coronary arteries has been a standard practice for more than a decade. Current stent technology is based on the use of corrosion-resistant metals such as 316L stainless steel, Nitinol and cobalt-chromium alloy. Although bare metallic stents have been proved to be effective in the prevention of reocclusion in atherosclerotic vessels, it is suggested that the required function of stents in temporary and limited to a period of 6-12 months after the implantation until the arterial remodelling and healing is achieved. Therefore, the implantation of degradable stents which provide scaffolding effect and are removed gradually from the artery can be a logical solution for the complications of permanent stents [23]. In the last decade, several researches have been published on *in vitro* and *in vivo* evaluation of iron and magnesium based degradable stents. Pure iron stents [5,6] and magnesium alloy AE21[37] and WE43 [38] have been investigated under *in vivo* implantation. However, no study on the fabrication process and characterization of these degradable stents has been published. Generally, stents are laser cut from metal tubes. Tubing is typically produced in either welded-redrawn or seamless form. Despite the robustness of modern welding equipment and continuous on line inspection systems, it is not possible to guarantee a fully defect-free weld without localized micro-contamination and segregation. Therefore, the tubing utilized for stents and other implantable devices should be seamless. Next, an adequate degree of control in the tube drawing process is required to ensure repeatable properties for the tubing. While stainless steel exhibits a moderate sensitivity to processing parameters, Nitinol is more difficult to control and can show wide ranges in its properties, depending on processing [8].

Laser cutting allows precise cutting of stent designs from tubes and because of its computer controlled mechanism, it is flexible in stent designs. After laser cutting, annealing is performed in order to relieve the residual stress produced during tube drawing and laser cutting and to improve the mechanical properties of the stent [148]. Annealed cut tubes are then acid pickled to remove the undesired part of cut tubes as well as burrs and debris.

In this work, we have investigated the feasibility of fabricating iron stent from electroformed tube. Iron tubes were produced by electroforming on a tin cylinder. They were then laser cut using the same laser cutting parameters as of Apolo 316L SS stent. The effect of each fabrication step on microstructure of iron stent was studied.

7.4 Materials and Methods

7.4.1 Tube Electroforming

Iron tubes were electroformed in a 400 g L^{-1} ferrous chloride- 80 g L^{-1} calcium chloride bath. 1 g L^{-1} of sodium saccharin was added to the solution as stress-reducer while 0.25g L^{-1} of sodium dodecyl sulfate was added as anti-pitting additive. Solution pH was adjusted to 1 with the addition of HCl and temperature was maintained at 90˚C. High purity tin rod was used as cathode for electroforming. 5 mm diameter tin rod (Sn≥ 99.9%) was purchased from Goodfellow, USA and its diameter was reduced to 3.1 mm using a wire drawing machine. The drawn rod was then cut into 4 cm rods which were cleaned in ethanol and subsequently water in an ultrasonic bath prior to electrodeposition. Two Armco® iron sheets (Fe≥ 99.8, Goodfellow, USA) of 60 × 20 × 2 mm were used as soluble anodes. Figure 7.1 shows a schematic view of the electroforming set-up. Constant current density of 2 Adm^{-2} was applied using a power source to the system for 300 min in order to obtain 150 µm-thick deposits. After electroforming, the rods were cleaned with water and ethanol to remove the residues from electrolyte. Top and bottom parts of the Fe-deposited rods were cut using diamond wheel in order to expose the two extremities of tin rods. The rods were transferred to a furnace preheated to 300˚C where they were held for 5 min until the tin rods were completely melted. The melts were removed from iron tubes using a desoldering pump

. The internal surface of the tubes was polished by Compound 320 grit abrasive to remove the traces of tin while the exterior surface was polished by 600-grit SiC abrasive paper.

7.4.2 Stent fabrication

35 mm iron tubes were cut into 3 slotted-tube stents using laser cutting machine. Nd-YAG laser with wavelength of 1064 nm, pulse frequency of 5300 Hz, pulse duration/pulse width of 10 μs and nominal power of 100 W was used for cutting in oxygen. Apolo stent design for fabrication of up to 3 mm expanded 316L stainless steel stent was used for laser cutting. As-cut tubes were then annealed at 550˚C in high purity Ar atmosphere for 1 h to relieve residual stress from electroforming and laser cutting. Acid pickling of annealed tubes was performed in a 2% solution prepared by dissolving a commercial iron stain powder (Super Iron Out®) in deionized water. The composition of the powder is presented in Table 7.1. The tubes were immersed in the solution at room temperature and pH of 6.9 in ultrasonic bath for 2 min at room temperature to remove the undesired parts of laser cutting. The final stents were then cleaned in ethanol and deionized water.

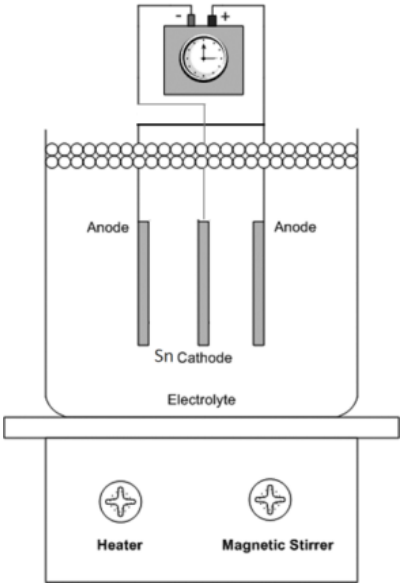

Figure 7.1- Schematic view of iron tube electroforming

Table 7.1- Ingredients of Super Iron Out® powder used in pickling of iron stents

Ingredients	CAS #	Wt. %
Sodium hydrosulfite	7775-14-6	3 -60
Sodium carbonate	497-19-8	3-7
Sodium chloride	7647-14-5	15-40
Sodium metabisulfite	7681-57-4	15-40
Citric acid	77-92-9	0.1-5

7.4.3 Characterization

SEM-EDS analysis as well as optical microscopy observation was performed on as-electroformed tube, ground tube, laser-cut tube, annealed tube and stent after acid pickling in order to investigate the effect of each fabrication step on shape, microstructure and composition. For microstructural studies, tubes and stent were vertically mounted in acrylic resin and their cross section was polished using 1000, 2400 and 4000 SiC abrasive paper and 0.05 μm silica paste. The polished surface was then etched by 2% nital solution to reveal the microstructure.

7.5 Results

7.5.1 Electroformed tube

Figure 7.2-a shows the image of electroformed iron tube and Figure 7.2-b shows SEM image of the surface morphology of the tube at high magnification. As-electroformed tube had relatively rough surface morphology as shown in Figure 7.2-b caused by the growth of crystallites as the deposit thickness was ~150 μm.

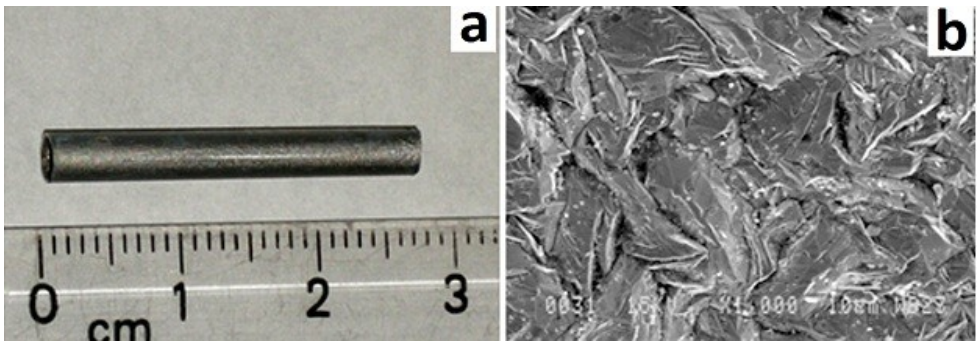

Figure 7.2- As-electroformed iron tube: (a) image (b) SEM surface morphology

Polished cross-section of iron tube is demonstrated in Figure 7.3-a. The image shows that although the tube thickness was relatively uniform, a layer of impurity can be seen in the interior surface. EDS analysis (Figure 7.3-b) revealed that the layer was composed of Sn showing that it was not completely removed from iron tube by melting.

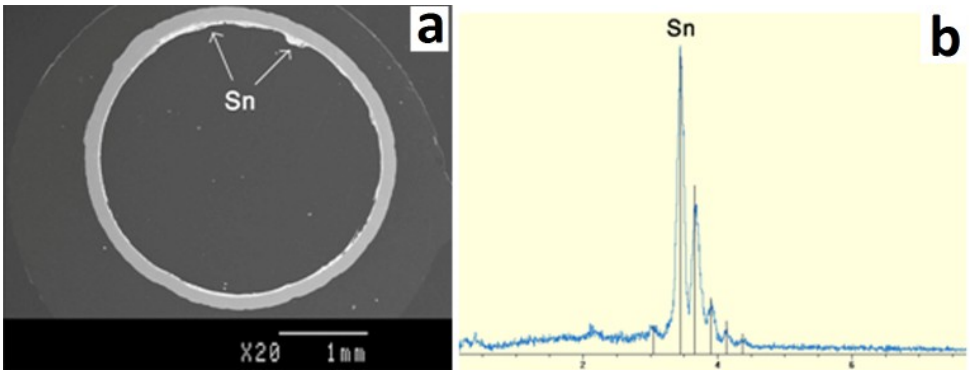

Figure 7.3- Cross-section of as electroformed tube (a) and EDS analysis of the white layer inside the tube (b)

The surface and polished cross-section of iron tube after grinding are presented in Figure 7.4. The roughness of iron tube decreased significantly by grinding as shown in Figure 7.4-a and c. However, the grinding lines are visible as the final grinding was by 600-grit SiC paper. As it can be seen in the cross-section image, the thickness of the tube was reduced by grinding, yet the traces of Sn could still be observed inside the tube. Grinding was not apparently acentric since the thickness of as-ground tube was not uniform as demonstrated in the Figure 7.4-b.

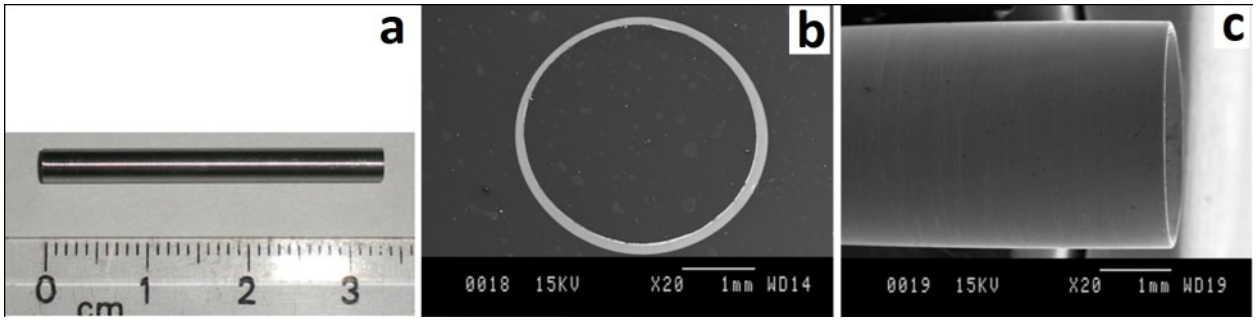

Figure 7.4- Electroformed iron tube after grinding: (a) image, (b) cross-section and (c) surface by SEM.

7.5.2 Stent fabrication

The laser cutting process was effective in production of stents from electroformed iron tube as presented in Figure 7.5. Laser cutting removed mostly the undesired parts of the stent as can be seen in Figure 7.5-a. However, cutting burrs and debris produced by laser cutting can still be seen in Figure 7.5-b. The burrs were mainly composed of Fe and oxygen as analyzed by EDS. The cross-section image of the as-cut tube shows that although some of the stent struts could be revealed; there were still the undesired part of stent which remained after laser-cutting. These parts are identified by arrow in Figure 7.5-c.

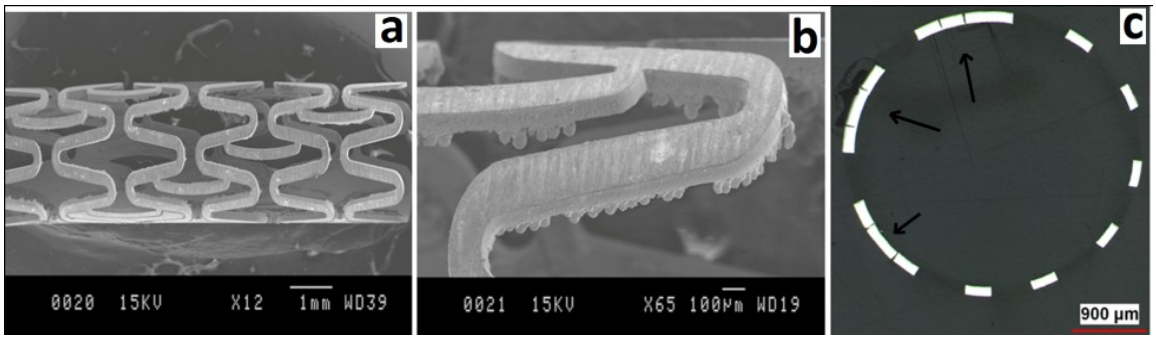

Figure 7.5- As-cut iron tube: (a) and (b) SEM micrographs and (c) microscopic image of polished cross-section.

The microstructures of annealed laser-cut tube before and after acid pickling are presented in Figure 7.6 while Figure 7.7 shows the as-polished cross section of annealed cut tube before and after acid pickling.

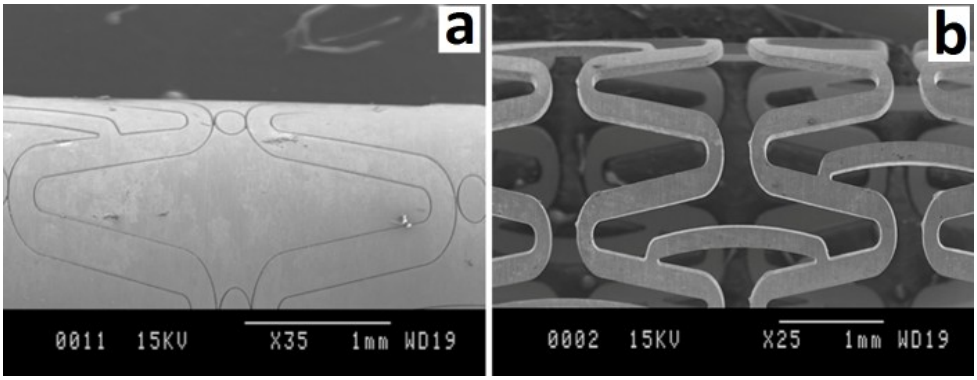

Figure 7.6- SEM micrograph of annealed cut iron tube (a) before and (b) after acid pickling.

As Figure 7.6 illustrates, the undesired parts of stent as well as laser cutting burrs and debris were removed by acid pickling and the final form of iron stent was achieved using the applied processing method. The surface finish of the stent also improved due to the removal of debris and levelling effect of the acid pickling. Figure 7.7 also shows that only the final stent struts were remained after acid picking and other parts were removed.

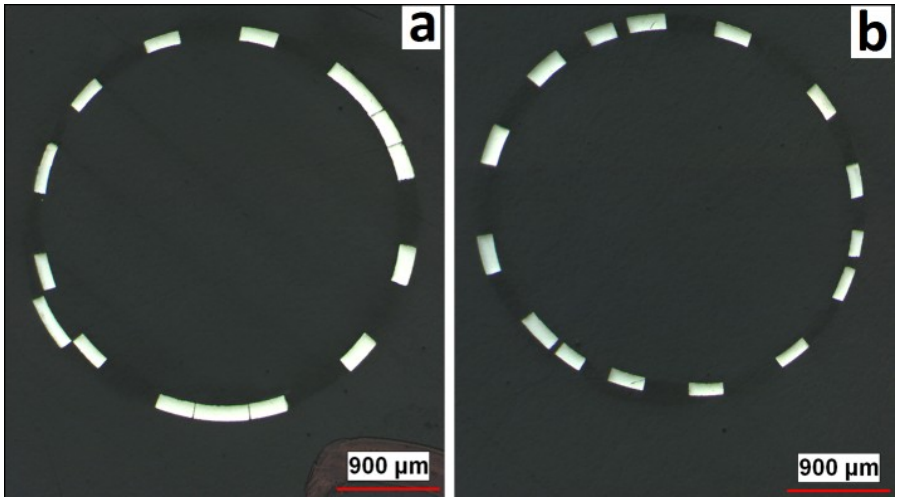

Figure 7.7- Polished cross section of annealed laser-cut iron tube (a) after annealing, (b) after acid pickling.

The dimensional parameters of the final iron stent are presented in Table 7.2.

Table 7.2- Dimensional parameters of iron stent.

Outside diameter (mm)	Wall thickness (mm)	Strut width (mm)	Connector width (mm)	Curvature width (mm)
3.36 ± 0.06	0.14 ± 0.02	0.25 ± 0.02	0.20 ± 0.01	0.16 ± 0.01

The general effect of each processing step of stent fabrication is presented in Figure 7.8 and EDS analysis data of different points of iron tubes and stent identified in Figure 7.8 are given in Table 7.3. In Figure 7.8 , A, B and C represent the laser-cut tube, the annealed laser-cut tube and the final stent after acid pickling respectively. The laser cutting lines can be seen in Figure 7.8-a. Inside the lines, the cutting debris are identified as point A2 which was composed on iron oxide as iron and oxygen were detected at this point using EDS analysis (Table 7.3). However, the stent strut (point A1) was only composed of iron and laser cutting had no effect (e.g. oxidation) on the other parts of the tube. After annealing (Figure 7.8-c), the oxide layer can still be detected in the cutting grooves (point B2) but still only iron was found at point B1.

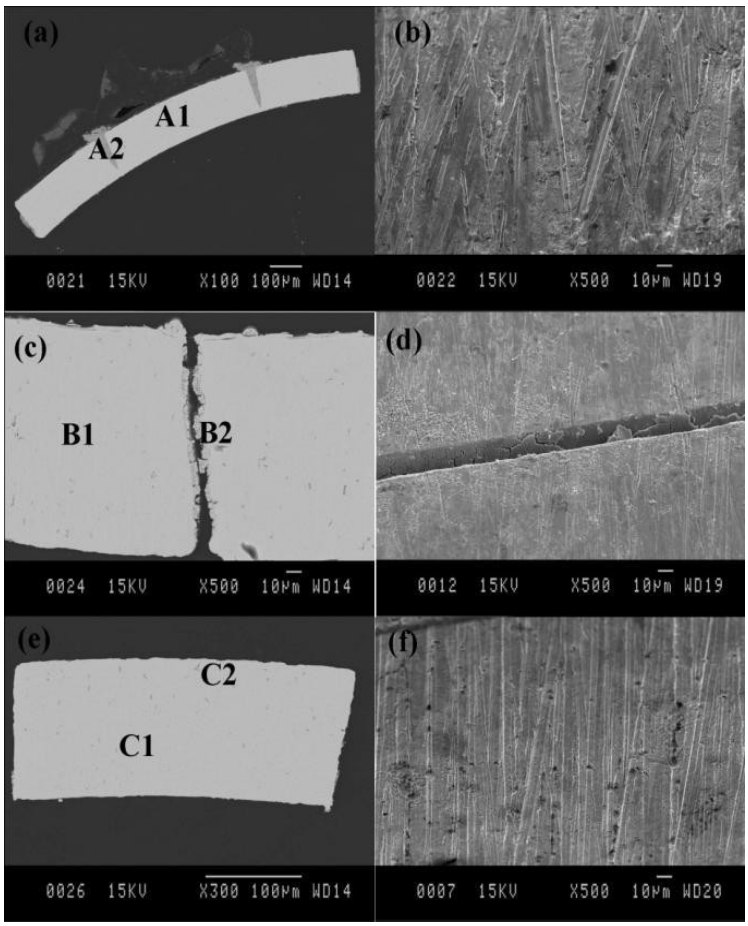

Figure 7.8- SEM images of cross sectional (left) and surface (right) of Fe stents: (a,b) laser cut minitube; (c,d) annealed laser cut minitube; (e,f) acid pickled minitube (stent).

Table 7.3- Composition of different points in laser-cut tube (A), annealed cut tube (B) and final stent (C).

Point	Form	Fe	O
	Laser cut tube		
A1	Metal	✓	-
A2	Burr	✓	✓
	Annealed laser cut tube		
B1	Metal	✓	-
B2	Burr	✓	✓
	Stent		
C1	Metal	✓	-
C2	Inclusion	✓	✓

After pickling, the struts were detached and the laser cutting oxide layer could not be detected. The general composition of the struts (e.g. point C1) was pure iron. However, small inclusions were detected as points near the borders of the struts which composed of iron and oxygen. The oxide inclusion may be formed by the corrosive effect of the solution during pickling.

7.5.3 Microstructure

The 2% nital etched microstructure of the cross-section of iron laser-cut tube, annealed laser-cut tube and final stent are presented in Figure 7.9-a, b and c, respectively. The arrow shows the direction of electrodeposition. The microstructure of as-cut tube (Figure 7.9-a) contained fine columnar grains which are typical grains for as-deposited metals [64]. After annealing, fine equiaxed grains (Figure 7.9-b) were produced in the structure of iron as a result of recrystallization of the material. Pickling step did not change the microstructure of annealed stent as seen in Figure 7.9-c. The equiaxed grains with the average size of 5 μm were detected in the struts of iron stents. The black dots seen in the microstructure were caused by prolonged etching.

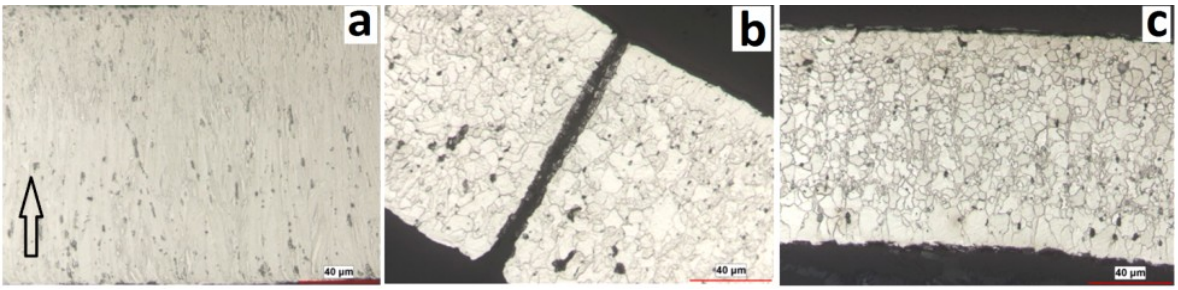

Figure 7.9- Optical micrograph of 2% Nital etched cross-section of (a) as –laser cut, (b) annealed laser cut Fe tube, and (c) pickled stent.

7.5.4 Discussion

This work has shown the feasibility of fabricating electroformed iron tubes for degradable stents. The main challenges in this process were finding the optimum electrodeposition parameters to produce iron layers with interesting mechanical properties including yield and tensile strength as well as high ductility. Decreasing the surface roughness and porosity was also an important requirement in this process. Although we has previously produced and optimized the electrodeposition parameters in order to fabricate iron foil with interesting properties [134], the fabrication of cylindrical samples was a major challenge. Finding a suitable cylindrical conductive cathode which could be removed after the electroforming was the most important step for iron tube fabrication. We have firstly tried a Ti6Al4V alloy cylinder as cathode since this material showed to have no adhesion with iron deposits in case of iron foils and could be easily removed after the process. However, the preliminary experiments showed that the removal of iron tube from Ti6Al4V cylinder was impossible because of the strong mechanical bonding of the two metals. Graphite also seemed to be an interesting candidate as a cathode for electroforming of Fe tubes as it is a soft material which could potentially be removed by machining. However, the surface preparation of graphite was an important challenge because of the porosity and softness of the material. Good surface finish of the cathode is generally important in order to achieve electrodeposits with low surface roughness. Based on the preliminary experiments with non-dissolvable cathodes, we decided to find a cathode which can be removed by dissolution. Since iron is a corrodible metal, a metallic dissolvable cathode could not be used as the dissolution process could attack the iron tube. Therefore, dissolvable polymers were another candidate since the organic solvents are not corrosive to iron tubes. It was

necessary for the polymer material to be resistant to iron electrodeposition conditions including chloride-based acidic electrolyte operated at pH=1 and temperature of 90˚C. PET (Polyethylene terephthalate) was selected to be the candidate polymer for this application as it is resistance to high temperature acidic solutions and could also be dissolved in an organic solution of 60% phenol and 40% tetrachloroethane. However, it was still necessary to render the surface of PET conductive before the electrodeposition. Iron coating was the most suitable choice since the deposition of other materials on the surface of PET could contaminate the electroformed iron tube. Electron-beam and thermal evaporation as well as electroless plating of iron were tried to produce Fe coating on PET. Unfortunately, evaporation techniques were not practical to produce thick coatings of Fe on PET as Fe has a relatively high melting point (1540˚C) and therefore needs longer time for evaporation. Electroless plating of iron was not successful either. Generally, electroless plating is performed in highly alkaline electrolytes [158] (pH ≥10) and iron precipitated at such high pHs into hydroxide form. Therefore, not enough iron ions were available to be reduced on the surface of PET. Because the use of polymer cathode showed to be impractical for iron electroforming, we finally decided to try low melting point metals as cathode. Lead, tin, bismuth and their alloys are considered low melting point metals and can potentially be applied as cathode for other metals with higher melting points in electroforming. These cathodes can be melted away from the electroformed metal by heating at temperatures lower than 300˚C [70]. We have selected high purity Sn as cathode since it has higher toxicity level in body that lead and bismuth. Its melting point is around 232˚C which is much lower than that of iron being 1540˚C. Sn could be removed easily by heating in a furnace at 300˚C. Although our result showed that after melting, the traces of Sn were found inside the Sn tube, no trace of Sn found in the final stent. Grinding of as-electroformed Fe tube was effective to increase its interior and exterior surface quality and to remove the traces of Sn. However, the grinding was not eccentric as it produced a non-uniform thickness distribution. Therefore, the grinding process should be improved to increase the thickness uniformity of iron tubes.

We have subsequently shown that it is feasible to fabricate degradable iron stents from electroformed tube using the same processing steps as of a commercial 316L stainless stent steel which is currently the gold standard material for stents. The same laser cutting

machine and parameters could be used for iron tubes, which is a significant advantage of this process since the already established technique for laser cutting can be applied to iron without a major adjustment.

Annealing of laser-cut stent tubes is an important step in stent fabrication. Generally, stents are laser-cut from as-drawn tubes which are in cold-worked state. Stainless steel tubes are annealed at 1100-1200˚C in vacuum for 1-2 h in order to produce a fine-grain recrystallized material and to improve the ductility of the tube after tube drawing. Annealing also helps reduce the internal stress of as-cut tubes caused by laser cutting [8,148]. In case of electroformed iron, we have shown that annealing at 550˚C for 1 h can induce recrystallization and fine-grain microstructure is subsequently produced. Annealing at this relatively low temperature also reduces the internal stress of electrodeposition and increases the ductility of iron significantly [134]. It is interesting that as-electroformed iron tube has high levels of stored energy as cold-worked metals. Generally, electroformed metals contain high density of structural defects such as point defect, dislocations and twins which increase the stored energy of these metals. This stored energy leads to recrystallization of a less-stressed and fine-grain structure upon annealing at lower temperatures [77]. Based on the applied standards, as-drawn stent tubes should have a grain size of ASTM 7 to 8, which indicates grain sizes of 24-34 μm [8]. After annealing, it is desirable to obtain the finest possible grain size for stents. A finer grain size reduces the risk of a stent strut breaking. The precipitation along the grain boundary is also minimised and the fatigue resistance is improved. Generally, the wall thickness of the tube should show a minimum of 8 to 10 grains [148]. Therefore, if the strut thickness of a stent is 100 μm, the average grain size should be 10-12.5 μm. In this work, we have shown that electroformed iron recrystallized with the average grain size of 5 μm. This fine grain size could not only provide more grains than 8-10 in a single strut (Figure 7.9-c), but can also provide higher mechanical strength for iron stent. Different studies have shown that the grain number requirement is not always achieved for 316L SS and could sometimes lead to the failure of the stent. Figure 7.10 shows the microscopic images of three 316L stainless steel stents adapted from different studies [148,159,160]. These images show that the minimum requirement of 8-10 grains in each strut was barely met and the grains are much larger than what we have observed for electroformed iron stent.

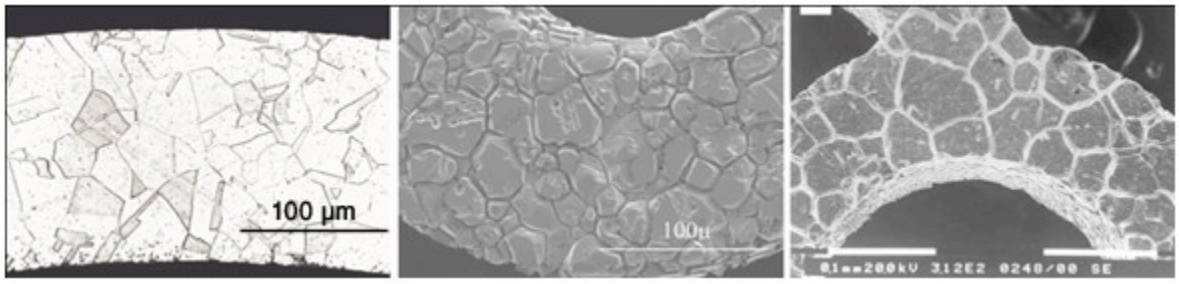

Figure 7.10- Microscopic images of 316L SS stent struts adapted from Refs. [148,159,160]

Acid pickling is an important step in stent fabrication performed after annealing in order to remove the undesired parts of stents as well as laser-cutting burrs and debris. For 316L SS, picking is performed in highly acidic solution containing HF and HNO_3 acids [152,153]. However, these solutions can be highly corrosive to the degradable stent materials such as iron and can either attack the surface of the stent or dissolve it completely. Therefore, special solutions with lower acidity should be developed for degradable stent materials. We have shown that a commercial solution used for removal of iron stains could be useful in pickling of iron stent since it removes the iron oxide formed in the laser-cutting lines of iron stent. The solution removed the cutting burrs and debris of laser cutting without corrosive effect to the stent.

7.6 Conclusions

This study showed that electroformed iron tube can be fabricated on a removable cylindrical Sn substrate which can be melted after electrodeposition. The resulting tube can used for fabrication of stent by applying the same laser cutting as of 316L SS following by annealing and acid pickling steps designed for iron. The produced stent had a fine microstructure with equiaxed grains having an average grain size of 5 µm which could potentially provide high strength and ductility for the stent. Although the preliminary stent fabrication process showed to be successful, the evaluation of mechanical properties and degradation of stents is necessary before further *in vivo* studies.

Chapter 8. General discussion and conclusions

This doctoral project has been a part of a general program for development and evaluation of metallic materials for degradable stents. These stents have emerged during the last decade as possible alternatives for the current permanent stents mainly because the temporary role of stenting has been clinically envisaged and the presence of stents after arterial remodeling would not be beneficial. In this context, iron and magnesium-based alloys are the candidate materials for degradable stents. Although extensive investigations have been performed on the application of magnesium alloys for degradable stents, these alloys show lower mechanical properties than iron and a very high degradation rate. Iron is interesting in terms of mechanical properties and shows a slower degradation. However, this slow degradation is a limiting factor for its application as degradable stent since iron stents did not corrode completely after 18 month of implantation in rabbits according to Peuster et al. [5]. This project aimed to modify the microstructure of iron in order to improve its mechanical properties and to decrease its corrosion resistance. We have selected the electrodeposition process in order to produce iron foils with different microstructure and properties. This project represents the first investigation of the feasibility of applying electroforming process towards the production of degradable stents. Currently, stents are laser cut from as-drawn tubes machined from metallic ingots. The ingots are produced either by casting or by powder metallurgy. The idea of applying electroforming in stent fabrication was to eliminate the numerous processing steps required for fabrication of metallic tubes by conventional metallurgical processes and also to modulate the microstructure. Using this technique, metallic tubes can be directly electroformed on a cylindrical substrate with the thickness of 100-200 μm which is the typical thickness of stent tubes. This technique is also specifically interesting for production of metallic layers as the structure of the metal is formed layer by layer. Although electrodeposition is generally used to fabricate metal coatings for corrosion protection or surface modification of a base metal, we have shown that it can be used to fabricate metallic materials for structural applications such as degradable stents in which certain mechanical properties are expected to provide the necessary support to the artery wall.

8.1 Electroforming process

The electroforming process was firstly developed in order to produce iron foils. The objective was to study the microstructure, mechanical properties and degradation of the electroformed material and these investigations were more feasible on flat specimens. The optimization of the electroforming process itself was a challenging task. The main challenge was to select a substrate which could be resistant to the corrosive attack of the electrolyte while being removable from the foils after the process. The optimization of the processing parameters including the electrolyte, temperature, pH and the current density was also challenge. 316L stainless steel was firstly selected as substrate since it was reported to be the most used substrate in electroforming. However, this material showed to adhere to the electrodeposited iron foils and its removal was almost impossible. Ti6Al4V was subsequently selected as substrate which proved not to have adherence with iron and the foils could be mechanically removed from this substrate by peeling. The selected electrolyte was Fischer-Langbien solution which has been reported to produce iron foils with higher ductility compared to other electrolytes for iron electrodeposition [64]. The temperature and pH were also selected to be 90˚C and 1 respectively based on the literature review in order to produce foils with higher ductility and strength [92,107]. However, the current densities in the range of 10-30 $A.dm^{-2}$ applied in the previous works on iron electrodeposition produced highly stressed foils with high surface roughness. Iron foils with higher ductility and lower surface roughness were produced at 2 $A.dm^{-2}$ and therefore, this current density was selected for production of the material. Organic additives including sodium saccharin and sodium dodecyl sulphate were also added to the electrolyte to decrease the internal stress of iron foils and to inhibit pitting in the deposits, respectively. The later acts as a surfactant and helps remove the hydrogen bubbles formed by the co-deposition of hydrogen on the cathode surface. The trapped hydrogen bubbles could produce significant porosity on electrodeposited iron foils in the additive-free bath.

It is worth mentioning that the electroforming process and the adjustment of its parameters was a challenging step which took almost one year to accomplish, since it was not available

at the beginning of the project. The developed electroforming process and parameters produced iron foils removable from the substrate, with acceptable surface roughness and relatively high ductility compared to electrodeposited metals. The process in now repeatable with reproducible results which can be applied easily for production of iron foils and tubes in laboratory scale and different microstructures can be produced using this process by modification of the parameters.

8.2 Microstructure and mechanical properties

Electroformed iron foils produced using the parameters mentioned in previous section had a strong <111> fiber texture revealed by EBSD. The formation of texture is common for electrodeposited metals due to the difference in the growth rate of different crystallographic directions. Iron foils also showed fine-grain structure compared to iron fabricated by casting and thermomechanical treatment with an average grain size of ~ 4 μm. As-electroformed iron foil showed interesting mechanical properties with yield strength comparable with that of 316L SS. Although the ductility of electrodeposited metals is generally low because of the internal stress, electroformed iron deformed up to about 8 % before breaking during the tensile test. The elongation of electroformed iron was improved to 18% by annealing at 550˚C for 1 h. Annealing of electroformed iron at relatively low temperature of 550˚C was found to induce recrystallization due to the presence of stored energy in microstructure of iron. This stored energy which is comparable to that of cold-worked metals can be attributed to the high concentration of structural defects produced by electrodeposition. Annealing at 650˚C improved the ductility to about 30 %, however, grain growth was observed for electroformed iron at this temperature leading to a decrease in yield and tensile strength. The values for σ_y and σ_{UTS} for electroformed iron annealed at 550˚C were 270 and 292 MPa respectively which are still superior to the mechanical properties of Armco® iron and Mg alloys and were close to those 316L SS. The preliminary corrosion testing of electroformed iron performed by potentiodynamic polarization showed that this material exhibited a higher corrosion rate than iron fabricated by casting and thermomechanical treatment, but lower than Mg alloys. This can be considered as an important advantage of electroformed iron, since the increase in degradation rate of iron was one of the objectives of this work. The accelerated corrosion

can be attributed to the smaller grain size of electroformed iron compared to iron produced by conventional metallurgical methods. Electrodeposition produced fine grains with the average of 4 μm in a single step process without any further requirement for grain refinement which is mandatory for as-cast metals. The finer grains of electroformed metal provided more grains boundaries which are more susceptible to corrosive attack and thereby increase the corrosion rate. Also, the high density of structural defects of electrodeposited iron can be held responsible for the acceleration of corrosion.

8.3 Degradation behavior cell viability study

Since the electrodeposited iron in this work was produced for application as degradable stent, the investigation of its degradation in physiologically simulated electrolytes was necessary for prediction of the degradation mechanism of the material before proceeding to *in vivo* implantation. Degradation behavior of iron electrodeposited foils was studied using static immersion and dynamic degradation methods. Static immersion test is a common method to study the corrosion of metals after aging in an electrolyte. However, dynamic degradation was performed in a specifically designed test bench which simulates the condition of a stented artery in which blood circulates. This technique has been developed in the Laboratory of Biomaterials and Bioengineering in Laval University and is the first method specified for degradation testing of metals for stent application. Hank's solution was used as the electrolyte as it simulates the ionic composition of blood plasma. In both degradation testing techniques, the pH and temperature of the electrolyte were 7.4 and 37˚C, respectively. Both of the applied techniques showed uniform degradation with a moderate rate for electroformed iron. The testing methods applied also confirmed that electroformed iron had a faster degradation than iron fabricated by casting and thermomechanical treatment. The reason for the faster degradation of electroformed iron is the finer grains observed for this material as well as the high density of structural defects produced by electrodeposition. This work demonstrates the potential of electrodeposition for production of metals with different microstructures than those obtained with conventional metallurgical techniques. This potential may be used to "tailor" the microstructure of metals by adjusting the electrodeposition parameters. Although different degradation rates were obtained for electroformed and casted iron, the degradation

mechanism was found to be similar. The first stage of degradation was the oxidation of iron to ferrous ions. Ferrous ions then oxidized to ferric ions and produced ferric hydroxide. Since the solution contained chlorine ions and oxygen, the ferric hydroxide hydrolyzed and produced more complex iron hydroxides. These materials covered the surface of iron samples during degradation testing and thereby decreased the degradation rate. The *in vivo* degradation mechanism of iron stents could be different as the degradation products have been found to be removed by macrophages and a thick layer of hydroxide was not formed on the surface of stent [5]. However, blood proteins and endothelial cells can cover the surface of the stent after few days of implantation which could also decrease the degradation rate. Generally, *in vitro* degradation tests can be useful for investigating the degradation behavior of the candidate materials for stents in order to select a suitable candidate before proceeding to *in vivo* studies.

The preliminary cell viability test using rat smooth muscle cells (SMC) were performed to access the cells metabolic activity and proliferation when exposed to electroformed iron. The results showed no inhibition of SMC metabolic activity by electroformed Fe compared to control, 316L stainless steel and iron fabricated by casting and thermomechanical treatment. However, electroformed iron slightly decreased the cell number because of its faster degradation. This can suggest that this material could be beneficial in the inhibition of cell proliferation if implanted as a cardiovascular stent. Although the preliminary results are promising, biological response to electroformed iron during and after degradation needs to be carefully assessed by performing *in vivo* tests.

8.4 Effect of electrodeposition current density on microstructure and degradation

Based on the results presented in chapters 4 and 5, it was found that electroformed iron had a faster degradation than iron produced by casting and thermomechanical treatment mainly because of the difference in the microstructure. Therefore, it was interesting to investigate the effect of microstructure of electroformed iron on its degradation. As electrodeposition parameters play an important role in determining the texture and microstructure of metal, one of these parameters was selected to produce different structure. Current density had

been previously shown to have a significant influence on microstructure of iron [106]. Therefore, current density was varied in the range of 1-10 $A.dm^{-2}$ and the resulted electrodeposited foils were investigated as presented in chapter 6. The values of the selected current densities were 1, 2, 5 and 10 $A.dm^{-2}$. All films were annealed at 550˚C for 1 h since annealing of electroformed iron found to improve its ductility which is required for application as stent. The degradation testing was performed on all samples deposited at different current densities before and after annealing. The result of EBSD showed a strong (1 1 1) fibre texture for iron deposited at 2 $A.dm^{-2}$ with the average grain size of ~ 4 μm as had been already shown chapter 4. However, other films had more randomly oriented microstructures with smaller grain size and weak <1 0 1>//ND and <1 1 2>//ND textures. For all current densities, columnar grain growth was observed in cross-section images of the foils except for 5 $A.dm^{-2}$ which produced equiaxed grains. These results clearly confirmed that various microstructures with different grain size and texture could be produced by adjusting the deposition parameters. Lower current densities favoured the formation of a texture while higher current densities of 5 and 10 $A.dm^{-2}$ produced more randomly oriented microstructures. Annealing at 550˚C for 1 h was found to change the microstructure of electroformed iron by inducing recrystallization as the texture and grain size changed after annealing for all iron samples. The recrystallization of electrodeposited iron after annealing can be attributed to the high amount of stored energy in the material due to the high density of structural defects produced by electrodeposition. A partial grain growth was also observed by annealing for all samples except for the one deposited at 10 $A.dm^{-2}$.

Corrosion testing performed by potentiodynamic polarization showed that the texture and microstructure play an important role on the corrosion rates of electroformed iron. However, no direct correlation between the electrodeposition current density and corrosion rate was found. The grain size and total grain boundary volume was the most influential factor affecting the corrosion rate. Fe deposited at 5 $A.dm^{-2}$ had the fastest corrosion due to its fine and equiaxed grains providing the most volume of grain boundaries. The microstructural defects could also affect the corrosion rate. The highest amount of porosity was observed for Fe-5 which had the highest corrosion rate. The corrosion rates of all samples decreased after annealing as a result of recrystallization and grain growth.

Although annealing has a positive effect on ductility of electroformed iron as it reduces the structural defects and stress, it can reduce the degradation rate which is not desirable for iron stent. However, it is an inevitable step in stent fabrication to provide the required mechanical and microstructural properties.

As presented in chapter 6, the effect of microstructure on degradation rate was less significant in the static immersion test, especially after annealing. Because of the formation of degradation products on the surface shortly after the test, the degradation rate decreased in static immersion. As the degradation products diminished the ion release of the samples, the difference in degradation rate of iron samples was less than what observed in potentiodynamic polarization. However, different degradation morphologies were observed for iron samples deposited at different current densities after the static test. All samples showed uniform degradation in macroscopic scale. This uniform degradation is an interesting property of iron, as localized corrosion may lead to the failure of implanted stents. In microscopic scale, Fe-2 with strong <1 1 1>//ND texture showed the most uniform degradation form while other samples developed micropits caused by preferential corrosion attack on different grains. The formation of pits in microscopic scale could help accelerate the degradation of iron and therefore could be interesting for application of as degradable stent.

8.5 Fabrication of stent from electroformed iron tube

The last part of the project was the fabrication of stents from electroformed iron tube and their microstructural evaluation. Tube electroforming was one on the most important objectives of the project, as stents are laser cut from metallic tubes. After using several cylindrical substrates for tube electrodeposition, high purity Sn cylinder was selected. The advantages of Sn are its low melting point, i.e. 231˚C compared to iron and its resistance to the highly acidic electrolyte. Iron tubes were electroformed on Sn cylinder, 3 mm in diameter, and the substrate was removed after electroforming by melting at 300˚C. Although traces of Sn were found in the interior of iron tubes, grinding could remove these traces and improve the surface finish of the tubes. The produced tubes were successfully used for fabrication of stents by applying the same laser cutting process as of 316L stainless

steel Apolo stent. Annealing and acid picking steps were subsequently performed on the leaser-cut tubes based on the processing parameters especially designed for iron. In case of degradable stents, it is mandatory to develop annealing and descaling processes suitable for these materials because those used for 316L stainless steel can deteriorate the mechanical properties and attack the surface prior to application. For instance, the annealing temperature of stainless steel stents is 1100-1200˚C at which recrystallization occurs in as-drawn tube and fine-grain recrystallized microstructure is produced to increase the ductility and strength of the stent. However, these temperatures can result in a significant grain growth in pure iron which deteriorates its mechanical properties. Therefore, annealing parameters should be optimized for pure iron to produce fine recrystallized microstructure without significant grain growth. This work has shown that annealing at 550˚C produced recrystallized equiaxed grain with the average size of 5µm. Acid pickling of stainless steel is also performed in highly acidic solutions containing HNO_3 and sometimes HF. These solutions can result in the corrosion of iron stent and could potentially dissolve it completely. The application of a slightly acidic solution for iron, presented in chapter 7, showed successful removal of the undesired part of iron stent without corrosive attack. The solution only dissolved iron oxides formed in the laser cutting lines and burrs and iron stent struts remained intact. Although the preliminary stent fabrication process showed to be successful, the evaluation of mechanical properties and degradation of stents is necessary before further *in vivo* studies.

8.6 Limits of the project

As explained in section 8.1, the objective of this work was to investigate the feasibility of fabricating iron by electroforming for application as degradable stents. The requirements for electroformed iron were high mechanical properties ideally comparable with those of 316L stainless steel and also uniform degradation faster than iron fabricated by casting and thermomechanical properties. It was shown that the developed electroforming process was successfully applied for fabrication for fabrication of iron foils. The electroforming parameters were selected in such a way to produce iron foils with low surface roughness and high ductility based on the literature review. However, the effect of each parameter including pH, temperature, current density and additive concentration was not studies

independently. Also, mechanical properties were measured only for electrodeposited iron deposited at certain parameters. The study of the effect of different electrodeposition parameters on mechanical properties was not investigated.

For degradation testing, the limits of the study include the use of an electrolyte which only contained ions similar to those of blood plasma and the effect of blood serum proteins was not studies. The main reason for that was to simplify the characterization of the degradation process. Also, the degradation testing was performed for only 14 days, while degradable stents are present in the artery for at least 6-12 months after the implantation. The reason was mainly because after this period (14 days), the formation of a degradation layer decreases significantly the degradation rate obtained from the test and the prolonged testing could not be more informative. Moreover, there are some differences between the *in vitro* and *in vivo* degradation mechanisms, as the effect of proteins and cells were not studied in degradation testing methods. The cell viability test in this investigation was performed using rat SMC. The more realistic test should be performed using human SMC and endothelial cells. The test was also conducted by indirect contact of iron samples with the serum in the culture wells. Therefore, the result might be disputable as the effect of the metal and its degradation products with direct contact with vascular cells under flowing conditions of blood in the artery could be different from what was performed in static conditions. However, this test was performed as a basic study of the effect of electroformed iron on cells in comparison with control and 316L stainless steel mainly to identify if electroformed iron could induce any negative effects on SMC viability.

As for the study of the effect of electrodeposition current density on microstructure and degradation of iron, the main limitation was the use of *in vitro* immersion test. Degradation products accumulated of the surface of the specimens and therefore, further degradation was limited after the formation of degradation layer which decreased the difference of degradation rates of samples deposited at different current densities. At more realistic conditions when the stent is implanted, the degradation products could be removed by macrophages and should not accumulate on the surface of iron [5,6].

In the 7th chapter, it was shown that iron stent can be successfully fabricated from electroformed iron tube. The main limitation was that iron tube was fabricated on Sn

substrate while Ti6Al4V alloy had been used as substrate for fabrication of iron foils in the previous studies. Although columnar grains were observed for iron tube electroformed on Sn similar to those observed with Ti alloy substrate, the texture could be different from the foils deposited on Ti alloy. The study of the texture of electroformed iron tube is therefore necessary. Also, the mechanical properties of the iron stents should be evaluated. Because stents are crimped on the catheter before implantation, they are firstly exposed to a compressive stress. During the implantation, the stents are expanded and go through a plastic deformation. The effect of compression and tensile plastic deformation on microstructure of the stents should be studies. Another limitation of this work was that the degradation studies were not performed on the fabricated stents. Degradation studies are necessary to investigate the effect of corrosion on stents before *in vivo* implantation. The other limitation would be the development of an electropolishing process for iron stents to improve their surface finish. This is a standard step in production of stents fabricated from different metals and should therefore be developed for iron.

8.7 Perspectives of the project

This project was the first to investigate the feasibility of applying electroforming process to fabrication of iron degradable stent. Although an electroforming process was developed and the properties of the produced iron foils and tubes were investigated, further developments and characterizations could be suggested to this project:

1. The effect of electroforming parameters including electrolyte pH and temperature on the microstructure and mechanical properties of iron: The effects should be studied since all of these parameters can influence the produced material.

2. Study of the effect of texture on mechanical properties of electroformed iron: Different grain size and textures affect the strength and ductility of the foils; therefore, it is helpful to investigate which microstructure would show higher mechanical properties.

3. The effect of plastic deformation of degradation behaviour of electroformed iron: Coronary stents are firstly crimped on a catheter before the implantation during

which they are exposed to compressive stress. During the implantation, the stents are expanded and plastically deformed to open the narrowed artery. Therefore, an implanted stent degrades after plastic deformation which can affect the corrosion process.

4. Study of the effect of using Sn as electroforming substrate on texture and mechanical properties of iron: Electroforming substrate has an important role on the texture of the deposited metal. Thus, the texture of the iron tube deposited on Sn cylinder can be different from the foil deposited on Ti alloy substrate. The study of the texture of iron deposited on Sn is therefore necessary.

5. Performing mechanical testing on the fabricated iron stents: Since iron stents would be subjected to compressive stress and tensile plastic deformation before and during the implantation, their radial strength should be evaluated. The effect of plastic deformation on different structural points of the stents can also be studied using mechanical behaviour modelling and experimental work.

6. Performing degradation testing on iron stents at different states: as-annealed, as-pickled, as-electropolished, as-crimpled and as-expanded: Each of these states can influence the microstructure of the stent and thereby affect the degradation mechanism and rate.

7. Study of the effect of grain refinement on mechanical properties and degradation of iron fabricated by casting and thermomechanical treatment and comparing the results to those of electroformed iron.

8. Development of an electroforming process for production of iron alloys in order to produce metals with higher degradation rate, and evaluation of the properties of the produced foils.

Biomedical Glossary

Angiography: the radiographic visualization of the blood vessels after injection of a radio-opaque substance

Angioplasty: surgical repair or recanalization of a blood vessel

Arterial Remodelling: changes in vascular dimensions during the development of atherosclerosis

Artery: any of the tubular branching muscular- and elastic-walled vessels that carry blood from the heart through the body

Atherectomy: surgical removal of atheromatous plaque from within a blood vessel by threading a catheter with a rotating cutting blade through blood vessels to the point of the lesion and using the blade to shave away the plaque

Atheroma: an abnormal fatty deposit in an artery

Atherosclerosis: an arteriosclerosis characterized by atheromatous deposits in and fibrosis of the inner layer of the arteries

Biocompatibility: the condition of being compatible with living tissue or a living system by not being toxic or injurious and not causing immunological rejection

Biodegradable: capable of being broken down especially into innocuous products by the action of living things (as microorganisms)

Carcinogen: a substance or agent causing cancer

Catheter: a tubular medical device for insertion into canals, vessels, passageways, or body cavities for diagnostic or therapeutic purposes (as to permit injection or withdrawal of fluids or to keep a passage open)

Enzyme: any of numerous complex proteins that are produced by living cells and catalyze specific biochemical reactions at body temperatures

Fibrin: a white insoluble fibrous protein formed from fibrinogen by the action of thrombin especially in the clotting of blood

Hyperplasia: an abnormal or unusual increase in the elements composing a part (as cells composing a tissue)

Hypertrophy: excessive development of an organ or part

Infarction: the process of forming an area of necrosis in a tissue or organ resulting from obstruction of the local circulation by a thrombus or embolus

Intima: the innermost coat of an organ (as a blood vessel) consisting usually of an endothelial layer backed by connective tissue and elastic tissue - called also tunica intima

Ischemia: deficient supply of blood to a body part (as the heart or brain) that is due to obstruction of the inflow of arterial blood (as by the narrowing of arteries by spasm or disease)

Lumen: the cavity of a tubular organ (the lumen of a blood vessel)

Necrosis: death of a portion of tissue differentially affected by local injury

Neointimal: a new or thickened layer of arterial intima formed especially on a prosthesis or in atherosclerosis by migration and proliferation of cells from the media

Patency: the quality or state of being open or unobstructed (evaluating arterial patency)

Plaque: an atherosclerotic lesion

Platelet: blood cell fragments that are involved in the cellular mechanisms that lead to the formation of blood clots

Proliferation: rapid and repeated production of new parts or of offspring (as in a mass of cells by a rapid succession of cell divisions)

Proliferative: capable of or engaged in proliferation

Pulmonary: relating to, functioning like, associated with, or carried on by the lungs

Restenosis: the reoccurrence of stenosis in a blood vessel or heart valve after it has been treated (as by balloon angioplasty or valvuloplasty) with apparent success

Revascularization: a surgical procedure for the provision of a new, augmented, or restored blood supply to a body part or organ

Sirolimus: a relatively new immunosuppressant drug used to prevent rejection in organ transplantation, and is especially useful in kidney transplants. It is also known as rapamycin.

Stenosis: a narrowing or constriction of the diameter of a bodily passage or orifice

Stent: an expandable wire mesh or hollow perforated tube that is inserted into a hollow structure of the body to keep it open

Stenting: a surgical procedure or operation for inserting a stent into an anatomical vessel

Strut: a structural component designed to resist longitudinal compression

Thrombogenicity: tending to produce a thrombus

Thrombosis: the formation or presence of a blood clot within a blood vessel

Thrombus: a clot of blood formed within a blood vessel and remaining attached to its place of origin

Sources:

1- Medical dictionary, Merriam Webster, http://www.nlm.nih.gov/medlineplus/mplusdictionary.html, Accessed on October 2010.
2- Wikipedia, the free encyclopedia, http://en.wikipedia.org/wiki/Main_Page , Accessed on October 2010.

References

1. Park JB, Lakes RS. Biomaterials : an introduction. New York: Springer; 2007. xi, 561 pp.
2. Bhat SV. Biomaterials. Boston: Kluwer Academic Publishers; 2002. xii, 265 pp.
3. Fox SI. Human physiology. Boston: McGraw-Hill Higher Education; 2009. xxiii, 808 pp.
4. Moore JE, Zouridakis G. Biomedical technology and devices handbook. Boca Raton: CRC Press; 2004.
5. Peuster M, Wohlsein P, Brugmann M, Ehlerding M, Seidler K, Fink C, Brauer H, Fischer A, Hausdorf G. A novel approach to temporary stenting: degradable cardiovascular stents produced from corrodible metal-results 6-18 months after implantation into New Zealand white rabbits. Heart 2001;86(5):563-569.
6. Peuster M, Hesse C, Schloo T, Fink C, Beerbaum P, von Schnakenburg C. Long-term biocompatibility of a corrodible peripheral iron stent in the porcine descending aorta. Biomaterials 2006;27(28):4955-4962.
7. Schlesinger M. Electrochemistry and Medical Devices Friend or Foe? The Electrochemical Society Interface 2003;12(3).
8. Poncin P, Proft J. Stent Tubing: Understanding the Desired Attributes. Materials & Processes for Medical Devices Conference: ASM; 2003.
9. Hermawan H, Dubé D, Mantovani D. Development of degradable Fe-35Mn alloy for biomedical application. Adv Mater Res 2007;15:107-112.
10. Hermawan H, Alamdari H, Mantovani D, Dube D. Iron-manganese: new class of metallic degradable biomaterials prepared by powder metallurgy. Powder Metall 2008;51(1):38-45.
11. Hart T, Watson A. Electroforming. Met Finish 2007;105(10):331-341.
12. Colombo A, Stankovic G, Moses J. Selection of coronary stents. JACC 2002;40(6):1021-1033.
13. MacGeough JA, Leu MC, Rajurkar KP, De Silva AKM, Liu Q. Electroforming process and application to micro/macro manufacturing. CIRP Annals-Manufacturing Technology 2001;50(2):499-514.
14. World Health Organization. https://apps.who.int/infobase/report.aspx?iso=CAN&rid=119&goButton=Go; Accessed on: 4 March 2010.
15. Developmental process of atherosclerosis. http://www.nlm.nih.gov/medlineplus/ency/imagepages/18020.htm; Accessed on March 2010.
16. Corwin EJ. Handbook of pathophysiology. Philadelphia: Wolters Kluwer Health/Lippincott Williams & Wilkins; 2008. xviii, 750 pp.
17. Chan AW, Moliterno DJ. In-stent restenosis: update on intracoronary radiotherapy. Cleve Clin J Med 2001;68(9):796-803.
18. El-Omar MM, Dangas G, Iakovou I, Mehran R. Update on In-stent Restenosis. Curr Intervent Cardiol Rep 2001;3(4):296-305.
19. UPMC. http://www.upmc.com/healthAtoZ/Pages/HealthLibrary.aspx?chunkiid=14867; Accessed on March 2010.

20. Schwertz DW, Vaitkus P. Drug-eluting stents to prevent reblockage of coronary arteries. J Cardiovasc Nurs 2003;18(1):11-16.
21. Mitka M. Drug-eluting stents show promise: but experts warn against enthusiasm outpacing science. JAMA 2004;291(6):682-683.
22. Erne P, Schier M, Resink TJ. The road to bioabsorbable stents: reaching clinical reality? Cardiovasc Intervent Radiol 2006;29(1):11-16.
23. Colombo A, Karvouni E. Biodegradable stents : "fulfilling the mission and stepping away". Circulation 2000;102(4):371-373.
24. Hermawan H, Dube D, Mantovani D. Developments in metallic biodegradable stents. Acta Biomater 2009;6(5):1693-1697
25. Saito S. New horizon of bioabsorbable stent. Catheter Cardiovasc Interv 2005;66(4):595-596.
26. Eberhart RC, Su SH, Nguyen KT, Zilberman M, Tang L, Nelson KD, Frenkel P. Bioresorbable polymeric stents: current status and future promise. J Biomater Sci Polym Ed 2003;14(4):299-312.
27. Tamai H, Igaki K, Kyo E, Kosuga K, Kawashima A, Matsui S, Komori H, Tsuji T, Motohara S, Uehata H. Initial and 6-month results of biodegradable poly-l-lactic acid coronary stents in humans. Circulation 2000;102(4):399-404.
28. Tsuji T, Tamai H, Igaki K, Kyo E, Kosuga K, Hata T, Nakamura T, Fujita S, Takeda S, Motohara S and others. Biodegradable stents as a platform to drug loading. Int J Cardiovasc Intervent 2003;5(1):13-6.
29. Peng T, Gibula P, Yao KD, Goosen MF. Role of polymers in improving the results of stenting in coronary arteries. Biomaterials 1996;17(7):685-694.
30. Maurus PB, Kaeding CC. Bioabsorbable implant material review. Oper Tech Sport Med 2004;12(3):158-160.
31. Hermawan H, Dube D, Mantovani D. Developments in metallic biodegradable stents. Acta Biomater 2010;6(5):1693-1697
32. Waksman R, Pakala R, Baffour R, Seabron R, Hellinga D, Tio FO. Short-term effects of biocorrodible iron stents in porcine coronary arteries. J Interv Cardiol 2008;21(1):15-20.
33. Peuster M, Beerbaum P, Bach FW, Hauser H. Are resorbable implants about to become a reality? Cardiol Young 2006;16(2):107-116.
34. Niemeyer M. Magnesium alloys as biodegradable metallic implant materials. 2001; Rimini, Italy. Euromat 2001, 7th Conference on Advanced Materials and Processes.
35. Witte F. The history of biodegradable magnesium implants: a review. Acta Biomater 2010;6(5):1680-1692.
36. Heublein B, Rohde R, Niemeyer M, Kaese V, Hartung W, Rocken C. Degradation of metallic alloys - A new principle in stent technology? JACC 2000;35(2):14a-15a.
37. Heublein B, Rohde R, Kaese V, Niemeyer M, Hartung W, Haverich A. Biocorrosion of magnesium alloys: a new principle in cardiovascular implant technology? Heart 2003;89(6):651-656.
38. Di Mario C, Griffiths H, Goktekin O, Peeters N, Verbist J, Bosiers M, Deloose K, Heublein B, Rohde R, Kasese V and others. Drug-eluting bioabsorbable magnesium stent. J Interv Cardiol 2004;17(6):391-395.
39. Zartner P, Cesnjevar R, Singer H, Weyand M. First successful implantation of a biodegradable metal stent into the left pulmonary artery of a preterm baby. Catheter Cardiovasc Interv 2005;66(4):590-594.

40. Waksman R, Pakala R, Kuchulakanti PK, Baffour R, Hellinga D, Seabron R, Tio FO, Wittchow E, Hartwig S, Harder C and others. Safety and efficacy of bioabsorbable magnesium alloy stents in porcine coronary arteries. Catheter Cardiovasc Interv 2006;68(4):607-617.
41. ASTM Standard G31 - 72. Standard Practice for Laboratory Immersion Corrosion Testing of Metals, ASTM International, West Conshohocken, PA, 2004, DOI: 10.1520/G0031-72R04 , www.astm.org, Accessed on October 2010.
42. Kuwahara H, Al-Abdullat Y, Ohta M, Tsutsumi S, Ikeuchi K, Mazaki N, Aizawa T. Surface reaction of magnesium in Hank's solutions. Magnesium Alloys 2000 2000;350-3:349-358.
43. Witte F, Fischer J, Nellesen J, Crostack HA, Kaese V, Pisch A, Beckmann F, Windhagen H. In vitro and in vivo corrosion measurements of magnesium alloys. Biomaterials 2006;27(7):1013-1018.
44. Song GL, Song SZ. A possible biodegradable magnesium implant material. Adv Eng Mater 2007;9(4):298-302.
45. Hermawan H, Moravej M, Dubé D, Fiset M, Mantovani D. Degradation behaviour of metallic biomaterials for degradable stents. Adv Mater Res 2007;15-17:113-118.
46. Levesque J, Hermawan H, Dube D, Mantovani D. Design of a pseudo-physiological test bench specific to the development of biodegradable metallic biomaterials. Acta Biomater 2008;4(2):284-295.
47. Kannan MB, Raman RK. In vitro degradation and mechanical integrity of calcium-containing magnesium alloys in modified-simulated body fluid. Biomaterials 2008;29(15):2306-2314.
48. Gu XN, Zheng YF, Cheng Y, Zhong SP, Xi TF. In vitro corrosion and biocompatibility of binary magnesium alloys. Biomaterials 2009;30(4):484-498.
49. Song YW, Shan DY, Chen RS, Zhang F, Han EH. Biodegradable behaviors of AZ31 magnesium alloy in simulated body fluid. Mater Sci Eng C-Biomimetic and Supramolecular Systems 2009;29(3):1039-1045.
50. Witte F, Feyerabend F, Maier P, Fischer J, Stormer M, Blawert C, Dietzel W, Hort N. Biodegradable magnesium-hydroxyapatite metal matrix composites. Biomaterials 2007;28(13):2163-2174.
51. Xin YC, Liu CL, Zhang XM, Tang GY, Tian XB, Chu PK. Corrosion behavior of biomedical AZ91 magnesium alloy in simulated body fluids. J Mater Res 2007;22(7):2004-2011.
52. ASTM G59 - 97. Standard Test Method for Conducting Potentiodynamic Polarization Resistance Measurements, ASTM International, West Conshohocken, PA, 2009, DOI: 10.1520/G0059-97R09, www.astm.org, Accessed on October 2010.
53. ASTM F2129 - 08. Standard Test Method for Conducting Cyclic Potentiodynamic Polarization Measurements to Determine the Corrosion Susceptibility of Small Implant Devices, ASTM International, West Conshohocken, PA, 2008, DOI: 10.1520/F2129-06 , www.astm.org, Accessed on October 2010.
54. Little BJ, Lee JS. Microbiologically influenced corrosion. Hoboken, N.J.: Wiley-Interscience; 2007. xii, 279 p. p.
55. Hermawan H, Purnama A, Dube D, Couet J, Mantovani D. Fe-Mn alloys for metallic biodegradable stents: Degradation and cell viability studies. Acta Biomater 2010;6(5):1852-1860.

56. Mani G, Feldman MD, Patel D, Agrawal CM. Coronary stents: A materials perspective. Biomaterials 2007;28(9):1689-1710.
57. Bonsignore C. A decade of evolution in stent design. SMST-2003: Proceedings of the International Conference on Shape Memory and Superelastic Technologies 2004:519-528.
58. Hanzi AC, Sologubenko AS, Uggowitzer PJ. Design Strategy for Microalloyed Ultra-Ductile Magnesium Alloys for Medical Applications. Light Metals Technology 2009 2009;618-619:75-82.
59. Hermawan H, Dube D, Mantovani D. Degradable metallic biomaterials: design and development of Fe-Mn alloys for stents. J Biomed Mater Res A 2010;93(1):1-11.
60. Callister WD, Rethwisch DG. Materials science and engineering : an introduction. Hoboken, NJ: John Wiley; 2009.
61. Mitchell BS. An introduction to materials engineering and science for chemical and materials engineers. Hoboken, NJ: John Wiley; 2004.
62. Wu MH. Fabrication of nitinol materials and components. Shape Memory Materials and Its Applications 2001;394-3:285-292.
63. Hermawan H. Conception, Développement et Validation d'Alliages Métalliques Biodégradables pour Emploi dans le Domaine de la Chirurgie Endovasculaire: Université Laval; 2004.
64. Schlesinger M, Paunovic M. Modern electroplating. New York: Wiley; 2000. xiv, 868 pp.
65. Rudzki GJ. Surface finishing systems : metal and non-metal finishing : handbook-guide. Metals Park, Ohio, U.S.A. Teddington, Middlesex, England: American Society for Metals ;Finishing Publications; 1983. 421 pp.
66. Kanani N. Electroplating: Basic Principles, Processes and Practice: Elsevier Science; 2005.
67. Paunovic M, Schlesinger M. Fundamentals of electrochemical deposition. Hoboken, N.J.: Wiley-Interscience; 2006. x, 373 pp.
68. Malone G, Browning ME. ASM handbook, Volume 05: Surface Engineering, Electroforming. Materials Park, OH: ASM International; 1990.
69. Hart AC. Electroforming as a Production Process. Metallurgia 1986;53(12):534.
70. Rodia CM. Electroforming. Met Finish 1995;93(1):369-378.
71. Landolt D. Electrochemical and Materials Science Aspects of Alloy Deposition. Electrochim Acta 1994;39(8-9):1075-1090.
72. Rashidi AM, Amadeh A. The effect of current density on the grain size of electrodeposited nanocrystalline nickel coatings. Surf Coat Tech 2008;202(16):3772-3776.
73. Srolovitz DJ, Mazor A, Bukiet BG. Analytical and Numerical Modeling of Columnar Evolution in Thin-Films. J Vac Sci Tech a-Vacuum Surfaces and Films 1988;6(4):2371-2380.
74. Weil R. The Structures of Electrodeposits and the Properties That Depend on Them. Annu Rev Mater Sci 1989;19:165-182.
75. Dini JW. Electrodeposition : the materials science of coatings and substrates. Park Ridge, N.J., U.S.A.: Noyes Publications; 1993. xiii, 367 pp.
76. Merchant HD. Annealing Kinetics and Embrittlement of Electrodeposited Copper. J Electron Mater 1993;22(6):631-638.

77. Merchant HD. Thermal Response of Electrodeposited Copper. J Electron Mater 1995;24(8):919-925.
78. Weil R, Sheppard K. The Structures of Electrodeposits - Their Characterization and the Properties They Affect. Mater Character 1992;28(2):103-112.
79. Safranek WH. The properties of electrodeposited metals and alloys; a handbook. New York: American Elsevier Pub. Co.; 1974. ix, 517 p. p.
80. Randle V. Electron backscatter diffraction: Strategies for reliable data acquisition and processing. Materials Characterization 2009;60(9):913-922.
81. Bastos A, Zaefferer S, Raabe D, Schuh C. Characterization of the microstructure and texture of nanostructured electrodeposited NiCo using electron backscatter diffraction (EBSD). Acta Mater 2006;54(9):2451-2462.
82. Jeong DH, Gonzalez F, Palumbo G, Aust KT, Erb U. The effect of grain size on the wear properties of electrodeposited nanocrystalline nickel coatings. Scripta Mater 2001;44(3):493-499.
83. Bicelli LP, Bozzini B, Mele C, D'Urzo L. A review of nanostructural aspects of metal electrodeposition. Inter J Electrochem Sci 2008;3(4):356-408.
84. Zhang Z, Zhou F, Lavernia EJ. On the analysis of grain size in bulk nanocrystalline materials via X-ray diffraction. Metall Mater Trans a-Physical Metallurgy and Materials Science 2003;34A(6):1349-1355.
85. Tomov I, Banova R, Surnev S. X-Ray-Diffraction Method for Determination of Texture Evolution in Layers. Textures and Microstructures 1992;19(4):189-196.
86. Zhao T, Zagidulin D, Szymanski G, Lipkowski J. Application of atomic force microscopy and scaling analysis of images to predict the effect of current density, temperature and leveling agent on the morphology of electrolytically produced copper. Electrochim Acta 2006;51(11):2255-2260.
87. Grujicic D, Pesic B. Electrochemical and AFM study of nickel nucleation mechanisms on vitreous carbon from ammonium sulfate solutions. Electrochim Acta 2006;51(13):2678-2690.
88. Matsushima H, Nohira T, Mogi I, Ito Y. Effects of magnetic fields on iron electrodeposition. Surface & Coatings Technology 2004;179(2-3):245-251.
89. Azizi A, Sahari A, Felloussia ML, Schmerber G, Meny C, Dinia A. Growth and properties of electrodeposited cobalt films on Pt/Si(100) surface. Appl Surf Sci 2004;228(1-4):320-325.
90. Lee I, Chan KY, Phillips DL. Growth of electrodeposited platinum nanocrystals studied by atomic force microscopy. Appl Surf Sci 1998;136(4):321-330.
91. Grujicic D, Pesic B. Iron nucleation mechanisms on vitreous carbon during electrodeposition from sulfate and chloride solutions. Electrochim Acta 2005;50(22):4405-4418.
92. Harty SF, Mcgeough JA, Tulloch RM. A Review of the Electroforming of Iron and Iron-Nickel Alloy. Surf Tech 1981;12(1):39-55.
93. Nakamura K, Umetani M, Hayashi T. Electrodeposition of Iron-Rich Ni-Fe Alloys from Sulfate and Chloride Baths. Surf Tech 1985;25(2):111-119.
94. Gehrmann B, Hattendorf H, KolbTelieps A, Kramer W, Mottgen W. Corrosion behaviour of softmagnetic iron nickel alloys. Materials and Corrosion-Werkstoffe Und Korrosion 1997;48(8):535-541.

95. Li HQ, Ebrahimi F. Synthesis and characterization of electrodeposited nanocrystalline nickel-iron alloys. Mater Sci Eng a-Structural Materials Properties Microstructure and Processing 2003;347(1-2):93-101.
96. Rhen FMF, Hinds G, O'Reilly C, Coey JMD. Electrodeposited FePt films. Ieee Trans Magnet 2003;39(5):2699-2701.
97. Kim SH, Sohn HJ, Joo YC, Kim YW, Yim TH, Lee HY, Kang T. Effect of saccharin addition on the microstructure of electrodeposited Fe-36 wt.% Ni alloy. Surf Coat Tech 2005;199(1):43-48.
98. Yoo BY, Hernandez SC, Park DY, Myung NV. Electrodeposition of FeCoNi thin films for magnetic-MEMS devices. Electrochim Acta 2006;51(28):6346-6352.
99. Yang ZN, Zhang Z, Zhang JQ. Electrodeposition of decorative and protective Zn-Fe coating onto low-carbon steel substrate. Surf Coat Tech 2006;200(16-17):4810-4815.
100. Hassani S, Raeissi K, Golozar MA. Effects of saccharin on the electrodeposition of Ni-Co nanocrystalline coatings. J Appl Electrochem 2008;38(5):689-694.
101. Ricq L, Lallemand F, Gigandet MP, Pagetti J. Influence of sodium saccharin on the electrodeposition and characterization of CoFe magnetic film. Surf Coat Tech 2001;138(2-3):278-283.
102. Zarpellon J, Jurca HF, Klein JJ, Schreiner WH, Mattoso N, Mosca DH. Electrodeposition of Fe thin films on Si(111) surfaces in the presence of sodium saccharin. Electrochim Acta 2007;53(4):2002-2008.
103. Mohanty US, Tripathy BC, Das SC, Singh P, Misra VN. Effect of sodium lauryl sulphate (SLS) on nickel electrowinning from acidic sulphate solutions. Hydrometallurgy 2009;100(1-2):60-64.
104. Diaz SL, Calderon JA, Barcia OE, Mattos OR. Electrodeposition of iron in sulphate solutions. Electrochim Acta 2008;53(25):7426-7435.
105. Gow KV, Iyer SP, Wu HH, Castelliz KM, Hutton GJ. Microstructure, Internal-Stress and Mechanical-Properties of Electrodeposited Iron Foils. Surf Tech 1979;8(4):333-346.
106. Yoshimura S, Yoshihara S, Shirakashi T, Sato E. Preferred Orientation and Morphology of Electrodeposited Iron from Iron(Ii) Chloride Solution. Electrochim Acta 1994;39(4):589-595.
107. Lai SHF, Mcgeough JA, Lau P. Electroforming of Iron Foil. J Mech Work Tech 1978;1(3):231-243.
108. Yuan B, Haarberg GM. Electrodeposition of Iron in Aqueous Alkaline Solution: An Alternative to Carbothermic Reduction. ECS Transactions 2009;16(36):31-37.
109. Myung NV, Park DY, Urgiles DE, George T. Electroformed iron and FeCo alloy. Electrochim Acta 2004;49(25):4397-4404.
110. Crichton I, McGeough J, Thomson J. Effects of Cathode-Mandrel Surface Irregularities on the Mechanical Properties and Structure of Electroformed Iron Foil. J Mech Eng Sci 1980;22(2):49–53.
111. Gomes A, da Silva Pereira M, Mendonca M, Costa F. Effect of the substrate on the electrodeposition of iron sulphides. Solid State Sci 2002;4(8):1083-1088.
112. ASTM B832 - 93. Standard Guide for Electroforming with Nickel and Copper, ASTM International, West Conshohocken, PA, 2008, DOI: 10.1520/B0832-93R08 , www.astm.org, Accessed on October 2010.

113. Merchant HD, Liu WC, Giannuzzi LA, Morris JG. Grain structure of thin electrodeposited and rolled copper foils. Mater Character 2004;53(5):335-360.
114. Jartych E, Zurawicz JK, Maczka E, Borc J. Preparation of thin iron films by electrodeposition and characterization of their local magnetic properties. Mater Chem Phys 2001;72(3):356-359.
115. Bugayev K. Iron and steel production. New York: Books for Business; 2001, 252 pp.
116. ASTM D1976 - 02. Standard Test Method for Elements in Water by Inductively-Coupled Argon Plasma Atomic Emission Spectroscopy, ASTM International, West Conshohocken, PA, 2006, DOI: 10.1520/D1976-02 , www.astm.org, Accessed on October 2010.
117. ASTM E1019-03. Standard Test Methods for Determination of Carbon, Sulfur, Nitrogen, and Oxygen in Steel and in Iron, Nickel, and Cobalt Alloys, ASTM International, West Conshohocken, PA, 2006, DOI: 10.1520/E1019-03, www.astm.org, Accessed on October 2010.
118. ASTM E8M-04. Standard test methods for tension testing of metallic materials, ASTM International, West Conshohocken, PA, 2006, DOI: 10.1520/E0008_E0008M-04 , www.astm.org, Accessed on October 2010.
119. Morozov GI, Morozov VI. Hardenability of electrolytic deposits of iron during burnishing. Met Sci Heat Treat 1974;16(10):888-890.
120. Smialowski M. Hydrogen in steel : effect of hydrogen on iron and steel during production fabrication and use. New York: Pergamon Press; 1962.
121. Jartych E, Jalochowski M, Budzynski M. Influence of the electrodeposition parameters on surface morphology and local magnetic properties of thin iron layers. Appl Surf Sci 2002;193(1-4):210-216.
122. Choi J, Kang S, Lee D. Relationship between deposition and recrystallization textures of copper and chromium electrodeposits. J Mater Sci 2000;35(16):4055-4066.
123. Kim I, Lee SG. Initial and recrystallization texture of nickel electrodeposits. Textures and Microstructures 2000;34:159-169.
124. Ebrahimi F, Zhai Q, Kong D. Deformation and fracture of electrodeposited copper. Scripta Mater 1998;39(3):315-321.
125. Dazhin VG, Kurdyumov VA, Kon'kov YD. Recrystallization of electrolytic iron. Met Sci Heat Treat 1970;12(1):81-82.
126. Shadrow VG, Tochitskii TA, Boltushkin AV. On the Influence of Twinning Processes on Columnar Crystallite Growth in Electrodeposited Films. Crystal Res Tech 1993;28(2):157-161.
127. Krause A, Uhlemann M, Gebert A, Schultz L. A study of nucleation, growth, texture and phase formation of electrodeposited cobalt layers and the influence of magnetic fields. Thin Solid Films 2006;515(4):1694-1700.
128. Reddy AKN, Wilman H. Electron-diffraction evidence of an outward growth tendency in electrolytic crystal growth. Acta Crystallograph 1963;16(8):844-845.
129. Hill MA, Bingert JF, Lillard RS. The relationship between crystallographic orientation and the passivity and breakdown of beryllium. Available from: http://public.lanl.gov/MCEL/PDF-Publications/Be-OIM.pdf, Accessed on October 2010.

130. Butany J, Carmichael K, Leong S, Collins M. Coronary artery stents: identification and evaluation. J Clinical Pathol 2005;58(8):795.
131. Ashby DT, Dangas G, Mehran R, Leon MB. Coronary artery stenting. Catheter Cardiovasc Interv 2002;56(1):83-102.
132. Waksman R. Update on bioabsorbable stents: from bench to clinical. J Interv Cardiol 2006;19(5):414-21.
133. Hänzi A, Gunde P, Schinhammer M, Uggowitzer P. On the biodegradation performance of an Mg-Y-RE alloy with various surface conditions in simulated body fluid. Acta Biomater 2009;5(1):162-171.
134. Moravej M, Prima F, Fiset M, Mantovani D. Electroformed iron as new biomaterial for degradable stents: Development process and structure-properties relationship. Acta Biomater 2010;6(5):1726-1735.
135. ASTM G31 - 72. Standard Practice for Laboratory Immersion Corrosion Testing of Metals, ASTM International, West Conshohocken, PA, 2004, DOI: 10.1520/G0031-72R04 , www.astm.org, Accessed on October 2010.
136. Mueller PP, May T, Perz A, Hauser H, Peuster M. Control of smooth muscle cell proliferation by ferrous iron. Biomaterials 2006;27(10):2193-2200.
137. Loos A, Rohde R, Haveich A, Barlach S. In vitro and in vivo biocompatibility testing of absorbable metal stents. Macromolecular Symposia 2007;253:103-108.
138. Seiler HG, Sigel H, Sigel A. Handbook on toxicity of inorganic compounds. New York: Dekker; 1988. xxiv, 1069 pp.
139. Zhu SF, Huang N, Xu L, Zhang Y, Liu HQ, Sun H, Leng YX. Biocompatibility of pure iron: In vitro assessment of degradation kinetics and cytotoxicity on endothelial cells. Mater Sci Eng C-Biomimetic and Supramolecular Systems 2009;29(5):1589-1592.
140. Kiyama M, Takada T. Iron Compounds Formed by Aerial Oxidation of Ferrous Salt Solutions. Bull Chem Soc Japan 1972;45(6):1923-1924.
141. Olowe AA, Rezel D, Genin JMR. Mechanism of Formation of Magnetite from Ferrous Hydroxide in Aqueous Corrosion Processes. Hyperfine Interactions 1989;46(1-4):429-436.
142. Stohs SJ, Bagchi D. Oxidative Mechanisms in the Toxicity of Metal-Ions. Free Radic Biol Med 1995;18(2):321-336.
143. Ngamwongsatit P, Banada PP, Panbangred W, Bhunia AK. WST-1-based cell cytotoxicity assay as a substitute for MTT-based assay for rapid detection of toxigenic Bacillus species using CHO cell line. J Microbiol Methods 2008;73(3):211-215.
144. Moravej M, Purnama A, Fiset M, Couet J, Mantovani D. Electroformed pure iron as a new biomaterial for degradable stents: In vitro degradation and preliminary cell viability studies. Acta Biomater 2010;6(5):1843-1851.
145. Ramanauskas R, Quintana P, Maldonado L, Pomes R, PechCanul MA. Corrosion resistance and microstructure of electrodeposited Zn and Zn alloy coatings. Surf Coat Tech 1997;92(1-2):16-21.
146. Schreiber A, Schultze JW, Lohrengel MM, Karman F, Kalman E. Grain dependent electrochemical investigations on pure iron in acetate buffer pH 6.0. Electrochim Acta 2006;51(13):2625-2630.

147. Asgari H, Toroghinejad MR, Golozar MA. On texture, corrosion resistance and morphology of hot-dip galvanized zinc coatings. Appl Surf Sci 2007;253(16):6769-6777.
148. Meyer-Kobbe C, Hinrichs B. Why the annealing of 316LVM-Stents is so important, http://www.meko.de/downloads/316LVM.pdf, Accessed on October 2010.
149. Ebrahimi F, Ahmed Z. The effect of current density on properties of electrodeposited nanocrystalline nickel. J Appl Electrochem 2003;33(8):733-739.
150. Li D, Szpunar J. Textural evolution in electrodeposits under the influence of adsorbed foreign species: Part I Textural evolution in iron electrodeposits affected by hydrogen co-deposition. J Mater Sci 1997;32(20):5513-5523.
151. Wang Y, Peng R, Almer J, Odén M, Liu Y, Deng J, He C, Chen L, Li Q, Zuo L. Grain-to-grain stress interactions in an electrodeposited iron coating. Adv Mater 2005;17(10):1221-1226.
152. Hutchinson WB. Recrystallisation textures in iron resulting from nucleation at grain boundaries. Acta Metall. 1989;37(4):1047-1056.
153. Hansen K, Pantleon K. Microstructure stability of silver electrodeposits at room temperature. Scripta mater 2008;58(2):96-98.
154. Qi B, Kim D, Williamson D, Trefny J. Effects of Postdeposition Heat Treatment on Morphology and Microstructure of CdTe Grown by Electrodeposition. J Electrochem Soc 1996;143:517.
155. Enriquez J, Mathew X. The effect of annealing on the structure of CdTe films electro-deposited on metallic substrates. J Crystal Growth 2003;259(3):215-222.
156. Enriquez J, Mathew X. Anneal induced recrystallization of CdTe films electrodeposited on stainless steel foil: The effect of CdCl 2. Journal of Materials Science: Materials in Electronics 2005;16(9):617-621.
157. Schreiber A, Rosenkranz C, Lohrengel M. Grain-dependent anodic dissolution of iron. Electrochim Acta 2007;52(27):7738-7745.
158. Drovosekov A, Ivanov M, Lubnin E. Deposition of Iron by the Method of Chemical–Catalytic Reduction Using Sodium Hypophosphite. Protection of metals 2004;40(1):89-91.
159. Stöver M, Renke-Gluszko M, Schratzenstaller T, Will J, Klink N, Behnisch B, Kastrati A, Wessely R, Hausleiter J, Schömig A. Microstructuring of stainless steel implants by electrochemical etching. J Mater Sci 2006;41(17):5569-5575.
160. Zhao H, Humbeeck J, Sohier J, Scheerder I. Electrochemical polishing of 316L stainless steel slotted tube coronary stents. J Mater Sci: Mater Med 2002;13(10):911-916.